Redox and mixed valence in some solid state systems

Thesis

The Open University

REDOX AND MIXED VALENCE IN SOME SOLID STATE SYSTEMS.

By

Karl R Whittle MSc BSc

Submitted as requirement for the degree of PhD in Chemistry.

AUTHORS NUMBER : M7190919
DATE OF SUBMISSION: 29 JUNE 1998
DATE OF AWARD: 4 DECEMBER 1998

Department of Chemistry

June 1998

Declaration.

The work reported in this thesis was carried out solely by me in the Department of Chemistry, The Open University, except where indicated otherwise. No part of this work has been submitted for the award of a degree at any other institution.

Karl Whittle

Acknowledgements

Professor F.J.Berry at The Open University, for his kind help and supervision throughout this research.

Dr D.Johnson at The Open University, for the help and assistance he gave during the work on the silver amalgamation process.

Dr J.F.Marco, and Dr R.Gancedo for allowing me to collect the low temperature Mössbauer spectra in their laboratory at the CSIC in Madrid, Spain.

Dr C.B.Ponton, and I.Maclaren for their assistance given in the synthesis of hexaferrites at the Interdisciplinary Research Centre in Materials for High Performance Applications at The University of Birmingham.

Dr A.J.Williams for the collection of magnetic susceptibility data , at the Department of Metallurgy and Materials at The University of Birmingham and assistance in the subsequent analysis.

The technical staff at the Department of Chemistry at The Open University, for their help during this work.

The Engineering and Physical Sciences Research Council (EPSRC) for providing a studentship.

Abstract

The silver amalgamation process whereby silver sulphide ore is converted to silver metal using copper chlorides and mercury proceeds through a redox process. The process involves the transformation of Ag_2S to AgCl with a corresponding reduction of copper from Cu^{2+} to Cu^{+} and subsequent oxidation of Cu^{+} to Cu^{2+} by atmospheric oxygen. The AgCl is then reduced to Ag by mercury to form an amalgam. It has been found that the process proceeds similarly when iron replaces copper and involves a reduction of Fe^{3+} to Fe^{2+}.

The doping of $SrFe_{12}O_{19}$ by europium and lanthanum to form compounds of the type $Sr_{1-x}M_xFe_{12}O_{19}$ (M=Eu,La) has been achieved by three different methods, the calcination of oxides at 1250°C, calcination of a gel at 925°C, and hydrothermal processing of metal nitrates at 220°C. X-ray powder diffraction (XRD) indicates the formation of similar materials by each method. X-ray absorption fine structure (XAFS) has shown that the La^{3+} ions substitute for Sr^{2+} ions. The particle sizes of the

$Sr_{1-x}M_xFe_{12}O_{19}$ phase have been found by Scherrer analysis of the X-ray powder diffraction data to increase with the temperature involved in the synthesis method. The results show that the materials formed by the calcination of oxides have a size ~800 nm, while those made by hydrothermal processing are ~ 300 nm.

^{57}Fe Mössbauer spectra collected at various temperatures have shown that the dopant has negligible effect on the magnetic properties of the system. The results show a gradual coalescence of hyperfine fields as the temperature is decreased from 298K to 25K. Magnetic susceptibility measurements have shown that Eu- and La-doped $SrFe_{12}O_{19}$ prepared by the co-precipitation of a gel has a greater magnetic coercivity than those prepared by other methods.

TABLE OF CONTENTS.

TABLE OF FIGURES.

CHAPTER 1 - INTRODUCTION.

1.1 Aims.

The work reported in this thesis is concerned with an investigation of mixed valence phases formed in:

(i) The silver amalgamation process.

(ii) The doping of strontium hexaferrite.

1.2 The Silver Amalgamation Process.

1.2.1 Introduction.

The social and economic influence of the amalgamation process for the extraction of silver was very great [1]. In particular, in Europe during the 16th century, the coincidence of unprecedented inflation with the arrival of the extracted silver, provoked those with time to think into formulating the first monetary theories of economics [2]. Writers as eminent as David Hume [3] and John Maynard Keynes [4] have also argued that the influx of bullion from the amalgamation process encouraged the rise of capitalism in early modern Europe. Finally, there is universal agreement among economic historians that the subsequent flow of silver bullion from Europe to the Orient acted as a motor for world trade, and shaped world trading patterns during the 17th and 18th centuries [5].

In spite of its historical importance, there has never been complete agreement about the chemistry of the amalgamation process, and no studies of it have been made for many years. This chapter describes previous investigations of that chemistry. It begins with the ores from which the silver was extracted.

1.2.2 The silver ore.

The major deposits of silver in South America were found in the Zacetacas region of Mexico and at Potosi in modern day Bolivia, shown in Figure 1-1.

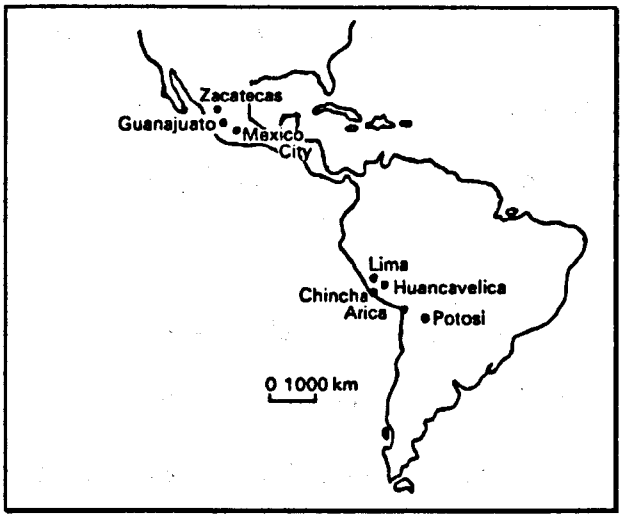

Figure 1-1 Map showing the regions of importance in the silver amalgamation process.[1]

The ore was generally found as a mixture of sulphides that underwent aerial oxidation by aerated water near the surface[6]. Silver would then be deposited as native Ag or in the presence of chloride as cerargyrite (AgCl). However the silver could be transferred downwards as aqueous silver ions or as complexes such as $[AgCl_2]^-$. But below the water table, there is a reduced sulphide zone where the descending silver is precipitated as sulphide minerals such as acanthite or argentite, both forms of Ag_2S[7]. This process is known as supergene enrichment. The overall result of such a process was a deposit containing two major regions, those above and below the water table. Above the water table, there was a rich oxidised zone where the silver was found as either native Ag or AgCl; below the table, in the reducing zone, the silver occurred as sulphides such as Ag_2S. An example of such a deposit was the famous Cerro Rico at Potosi where the oxidised zone was some 200m in depth.

1.2.3 Original Extraction.

During the early years of the Spanish occupation of South and Central America, the silver was obtained by direct smelting of the ore. This method was especially suitable when the ores were rich and came from the oxidised zone. However, with time, the quality of the ore decreased to a point where smelting became much less effective, and some new technique was required. Such a technique was the silver amalgamation process.

Although the Romans knew of the ability of mercury to dissolve silver and gold, it was not applied to the extraction of silver from its ores. Most historians date its first application to the extraction of silver in South America to the mid-1550s, and give the credit to Bartholomeo de Medina [8], a merchant from Seville. Rickard, however, disputes de Medina's priority[9].

The extraction process would follow 8 stages: [6,8,10]

(i) The silver ore was ground in a grinding mill called an *'arrastra'* (shown in Figure 1-2), which was powered by mules or horses.

(ii) The silver ore, once ground, was then converted into a mud by addition of water, and piled up into heaps of about 1500 kg of ore on a stone floor called a *'patio'*.

(iii) Salt was added and well trodden in for a day by horses, mules or native labour to ensure complete mixing.

(iv) On the second day *'magistral'* was added. This was weathered copper pyrites which contains copper(II) sulphate. Again, the addition was followed by thorough mixing.

(v) Finally mercury was added and the mixture trodden daily until amalgamation was complete. The process could take up to three months to complete.

(vi) After amalgamation was judged to be complete, fresh mercury was added to make the amalgam more mobile. The mass of material was then washed with running water, usually a stream, to remove the lighter non-amalgamated solids. After washing the heavy amalgam phase would remain.

(vii) The remaining amalgam was transferred to sacks and squeezed to remove any excess liquid mercury. This excess was collected for reuse.

(viii) The solid amalgam was then heated under iron bells. The mercury was thereby removed by distillation and again collected for reuse. The silver that was left behind could be melted and cast into ingots of about 98% purity.

A contemporary plate showing the Potosi mine where the above processes were undertaken is shown in Figure 1-3.

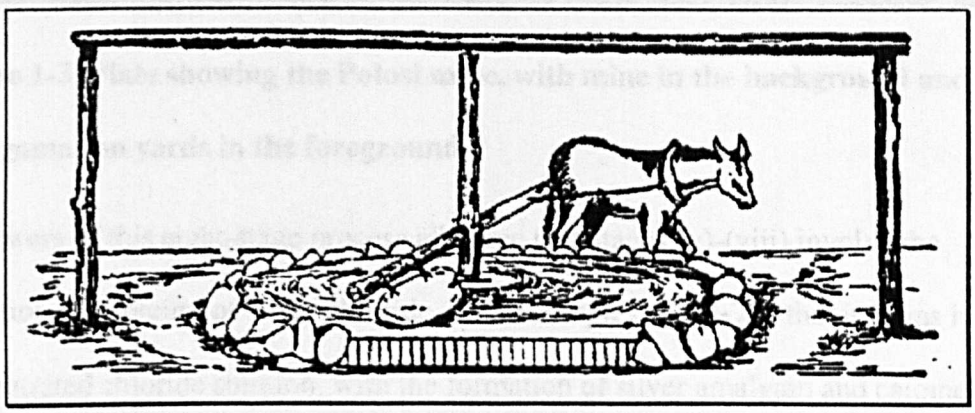

Figure 1-2 Detail of an arrastra , the stones forming the front have been removed to show the rock pavement.

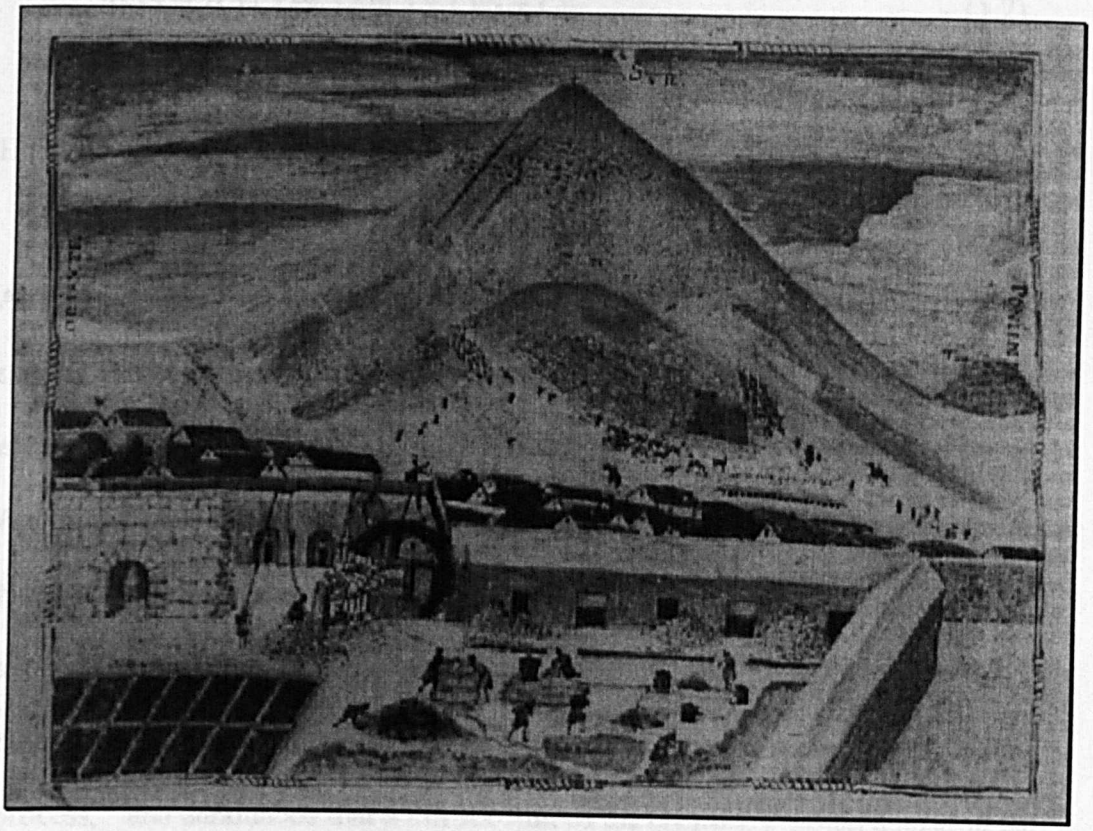

Figure 1-3 Plate showing the Potosi mine, with mine in the background and the amalgamation yards in the foreground.[1]

Reviewers of this eight-stage process all agree that stages (v)-(viii) involve the reduction by mercury of silver chloride, or the complex $AgCl_2^-{}_{(aq)}$ that it forms in concentrated chloride solution, with the formation of silver amalgam and calomel, Hg_2Cl_2. There is, however, disagreement about the chemical reactions in which the silver ore is converted into the chloride species in stages (ii)-(iv). Bakewell[6,8] quotes Bargallo[11] as his authority, and claims that the principal reaction is as follows:

$$Ag_2S + CuCl_2 \rightarrow 2AgCl + CuS \qquad (1.1)$$

This involves a simple transfer of counter ions. However, the existence of CuS as a terminal product seems unlikely as it is oxidised in moist air[12].

Another reviewer, Rickard[9], provides three possible reactions of which the one outlined above by Bargallo[11] is considered. The other two are:

$$Ag_2S + 2CuCl \rightarrow 2AgCl + CuS + Cu \quad (1.2)$$

$$Ag_2S + 2CuCl \rightarrow 2AgCl + Cu_2S \quad (1.3)$$

Habashi[13] proposed the following:

$$2Cu^{2+} + Ag_2S \rightarrow 2Cu^{+} + 2Ag^{+} + S \quad (1.4)$$

As equations (1.1)-(1.4) show, reviewers tend to write reactions without proper specification of physical, or even chemical, states. For example, in Habashi's equation (1.4), it is not clear what species are supposed to contain the ions Cu^{+} and Ag^{+}. The aqueous ions, or the insoluble chlorides CuCl and AgCl, could be meant. None of these reviewers considered the work of Percy which is important because it takes the role of atmospheric oxygen into account. In part 1 of his work on the metallurgy of silver and gold, Percy devoted much space to the amalgamation process,[10] and announced that a full account of the chemistry would appear in part 2 of the work[14]. Part 2 was never published, but the likely shape of his explanation is fairly clear from the study that he made of the reaction of copper salts with Ag_2S in chloride solution[15]. The initial reaction that he proposed is:

$$Ag_2S + 2CuCl_2 \rightarrow 2AgCl + 2CuCl + S \quad (1.5)$$

This resembles Habashi's reaction (1.4)[13]. However, Percy[10] then proposed a second reaction in which atmospheric oxygen is involved and the copper monochloride is oxidised to an insoluble basic chloride of copper (II). The result is an overall reaction of the type:

$$6Ag_2S + 3O_2 + 6H_2O + 8CuCl_2 \rightarrow 12AgCl + 6S + 2\{CuCl_2.3Cu(OH)_2\} \quad (1.6)$$

There may be further oxidation of the sulphur to thiosulphate or sulphate.

As can be seen above there has been no agreement in the reaction schemes that have been put forward. Moreover, none of the reviewers has made any attempt to connect their proposals with recent advances in hydrometallurgy. In particular, the oxidative

chloride leaching of sulphide ores of metals such as copper, nickel, lead and zinc has recently become an active field of research and development[16,17].

1.3 Strontium Hexaferrite.

1.3.1 Crystallographic Structure.

Strontium hexaferrite, $SrFe_{12}O_{19}$, is isomorphous with magnetoplumbite of composition $PbFe_{12}O_{19}$. The $SrFe_{12}O_{19}$ unit cell is hexagonal, with a=b=5.883Å and c=23.038Å. The space group for the magnetoplumbite structure is P63/mmc, No 194, Z=2. The α,β angles are 90° and γ=120°. The structure [18]consists of the following:

(i) A twelve oxygen co-ordinated Sr^{2+} ion, six O^{2-} in the plane with 3 above and 3 below, forming a polyhedron of 14 sides.

(ii) 3 Fe-O octahedra , known as the 12k, $4f_1$, $4f_2$ sites, following the nomenclature used in the International Tables of X-Ray Crystallography. The symbols denote a set of crystallographic operations with the number indicating the number of sites per unit cell.

(iii) A single Fe-O tetrahedron, 2a using the nomenclature outlined above.

(iv) A trigonal bipyramidal Fe-O polyhedron at 298K, known as 2b throughout this discussion.

(v) Five crystallographically independent oxygen sites forming a framework around the Sr and Fe ions.

The crystal structure is shown in Figure 1-4.

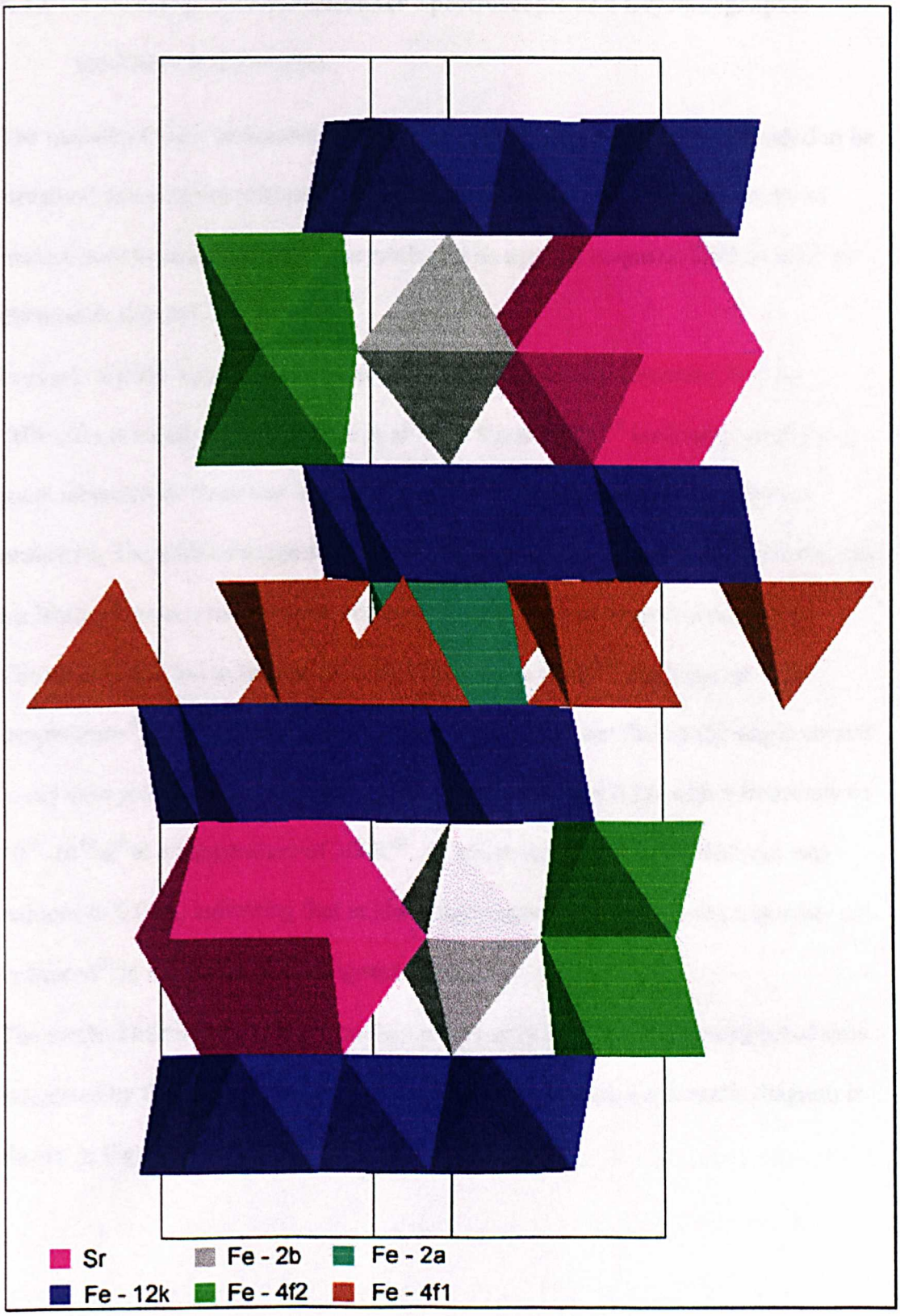

Figure 1-4 Diagram showing the $SrFe_{12}O_{19}$ crystal structure[18].

1.3.2 Low Temperature Mössbauer Spectroscopic and Crystallographic studies of Hexaferrites.

The majority of low temperature Mössbauer spectroscopic studies have tended to be structural and concern primarily the dynamics of the 2b Fe site. The majority of studies have tended to use single crystals and an applied magnetic field in order to distinguish this site.

In single crystal X-ray studies of the magnetoplumbite type structure, which $SrFe_{12}O_{19}$ is based upon, Obradors et al[18] and Kimura et al[19] both suggested that at room temperature there was a possibility that the 2b site was not trigonally co-ordinated. The authors suggested that the Fe may be thought to be located at this site oscillating between two adjacent tetrahedrally Fe-O co-ordinated crystal sites.

The observation led to further work by Fontcuberta et al[20,21] studying the low temperature ^{57}Fe Mössbauer spectra of $SrFe_{12}O_{19}$. They confirmed the single crystal X-ray data postulated and that the oscillation distance was 0.2Å with a frequency of 10^{11}-10^{12} s^{-1} at a temperature of 300K[20]. At lower temperatures the distance was reduced to 0.06Å, indicating that at low temperature this site becomes trigonally co-ordinated[21] in the centre of the trigonal bipyramid.

The method of movement between the two adjacent tetrahedrally co-ordinated sites suggested by the authors was an ion-tunnelling mechanism, a schematic diagram is shown in Figure 1-5.

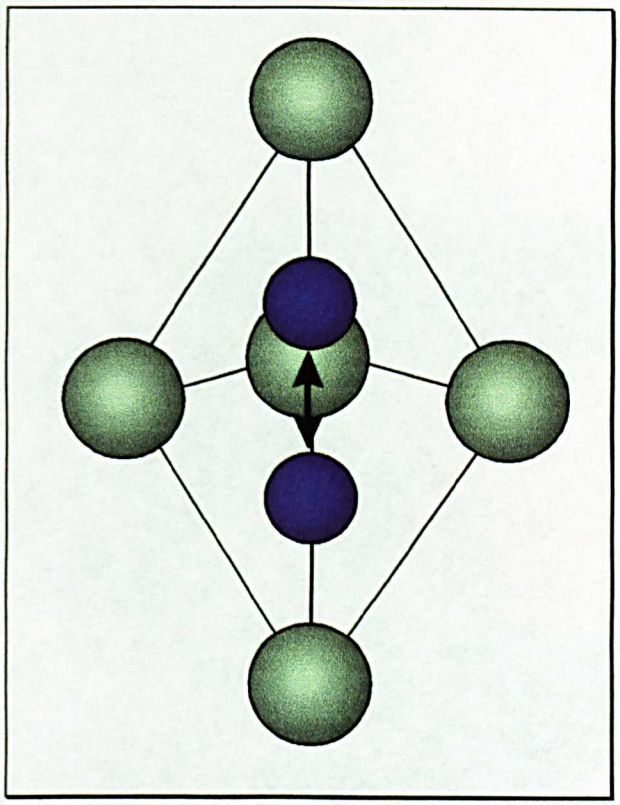

Figure 1-5 Schematic representation of oscillation between two Fe tetrahedral sites.

1.3.3 Magnetic structure.

In the magnetoplumbite structure the direction of magnetic alignment has been reported by van Diepen [22] as being along the c-axis. The resultant magnetic moment is the sum of the 2a, 2b, and 12k Fe ions being aligned parallel to the direction of magnetism. This sum is reduced by the anti-parallel behaviour of the $4f_1$ and $4f_2$ sites. With the magnetic moment of Fe^{3+} being $5\mu_\beta$, using the convention that the magnetic moment of a single unpaired electron is equal to $1\mu_\beta$, the overall result of this alignment is a theoretical value[22] of $20\mu_\beta$ per molecule for the saturation magnetisation at 0K. The magnetic structure is shown in Figure 1-6.

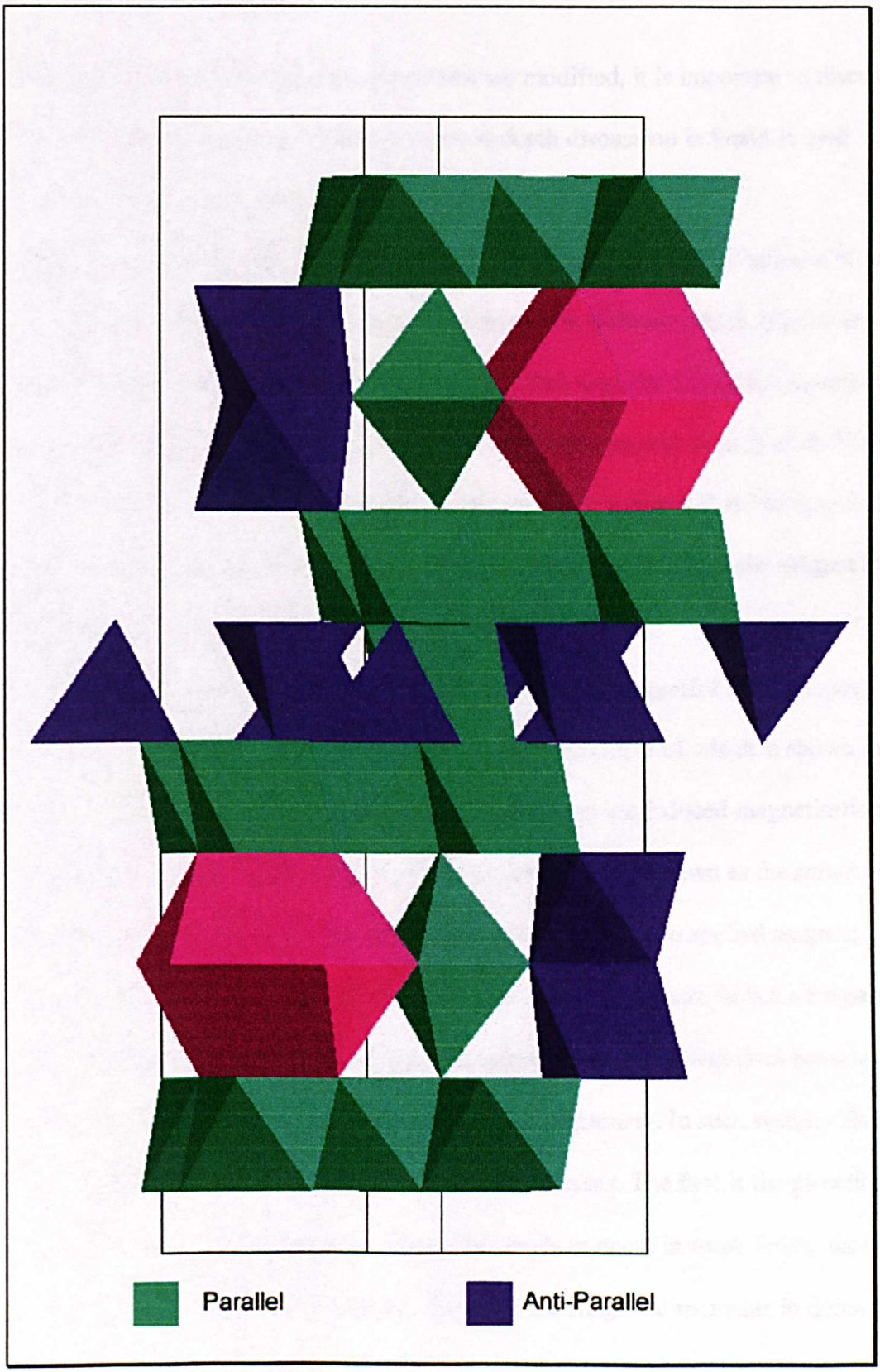

Figure 1-6 Magnetic Structure of $SrFe_{12}O_{19}$[22].

1.3.4 Magnetic Properties.

Before discussion of how magnetic properties are modified, it is important to discuss how magnetic properties are defined, a more in-depth discussion is found in well known textbooks such as Kittel[23].

In magnetic solids there are regions where the direction of magnetic alignment is one way whereas in other regions the magnetic alignment is different. Such regions are known as magnetic domains. Within each domain the magnetic alignment is parallel, but the arrangement of magnetic domains is random with respect to each other. If the arrangement of these domains results in a small magnetic moment then the magnet is known as a *hard* magnet. If there is no overall magnetic moment then the magnet is known as a *soft* magnet.

When a magnetic system is placed in a magnetic field, its magnetisation increases. This is conventionally known as a hysteresis loop, an example of which is shown in Figure 1-10. If the magnetic system is paramagnetic then the induced magnetisation increases with applied magnetic field, until it reaches a limit, known as the *saturation magnetisation*. After this point has been reached, any increase in applied magnetic field does not increase the induced magnetic field. However, if a solid has a magnetic moment with no applied field, i.e. it is a hard magnet, then this effect does not occur, as the individual moments already have a degree of alignment. In such systems there are two mechanisms by which the magnetisation increases. The first is the growth of magnetic domains at the expense of others, this tends to occur in weak fields, shown in Figure 1-7. In strong fields however rotation of the magnetic moments in domains occurs, this is shown in Figure 1-8.

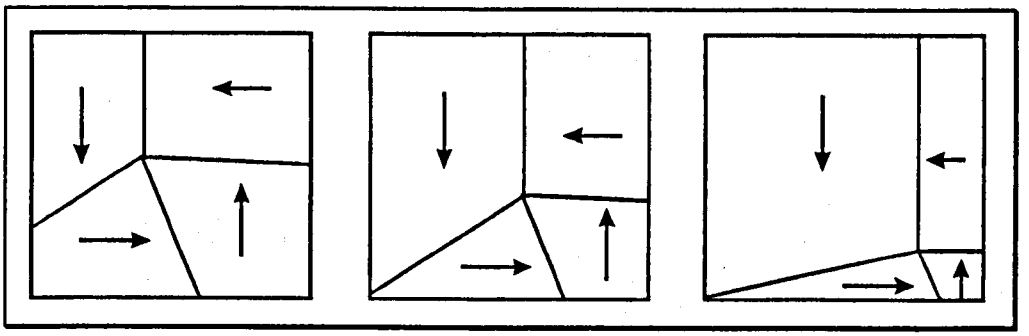

Figure 1-7 Diagram showing growth of magnetic domains at expense of others.

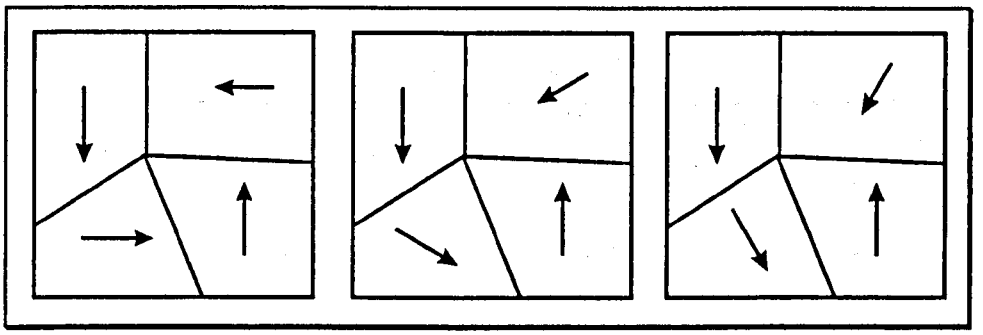

Figure 1-8 Diagram showing rotation of magnetic domains.

The mechanism of alignment is not fully understood but it involves the *walls* of these domains, which have a finite thickness, known as Bloch Walls[23]. Across a wall the magnetic spins rotate into alignment with the spins in the next domain. The growth of domains is thought to occur by a helical twisting of the moment, such an effect is shown in Figure 1-9.

Domain size is determined by two competing mechanisms. Interelectronic repulsion or exchange mechanisms which favour parallel alignment are short range effects and decrease rapidly with increasing distance. A competing force is the magnetic dipolar effect which favours antiparallel alignment, this force is 1000 times weaker than the interelectronic repulsion, but the force decreases as $1/r^3$ where r is the distance from the atom in question. As the distance from an atom is increased the more favourable alignment is antiparallel.

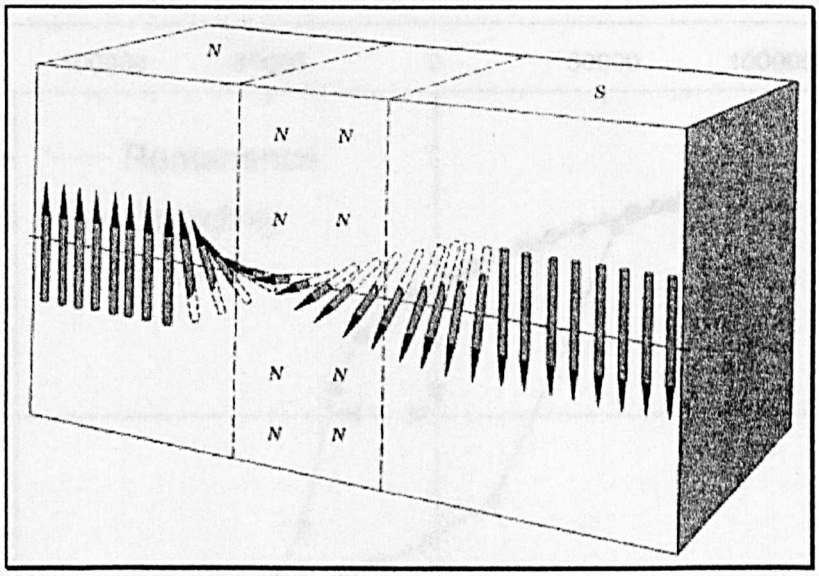

Figure 1-9 Diagram showing rotation of magnetic fields at Bloch Walls[23].

As particle size increases there comes a point whereby the interelectronic repulsion loses out to the magnetic dipolar effect, at this point the particle becomes multidomain and once this occurs, various magnetic properties change. The size at which a particle changes from being single to multidomain in $SrFe_{12}O_{19}$ is ~600nm. If a hard magnetic solid, such as $SrFe_{12}O_{12}$, has no applied magnetic field, but there is a measurable magnetic field, then such a magnetic field is known as the *remanant magnetisation* or *remanence*. If the same magnetic solid is influenced by a magnetic field to such an extent that the induced magnetic field in the solid is zero, then this magnetic field is known as the *coercive force* or *coercivity,* both of the above forces are shown in Figure 1-10, in a hysteresis loop. The magnetic force required to demagnetise the solid, i.e. reduce the magnetic field to zero, is directly proportional to the volume of magnetic solid being demagnetised. In *hard* magnetic materials both the remanence and coercivity values are high, whereas in *soft* magnetic materials both of these values are low.

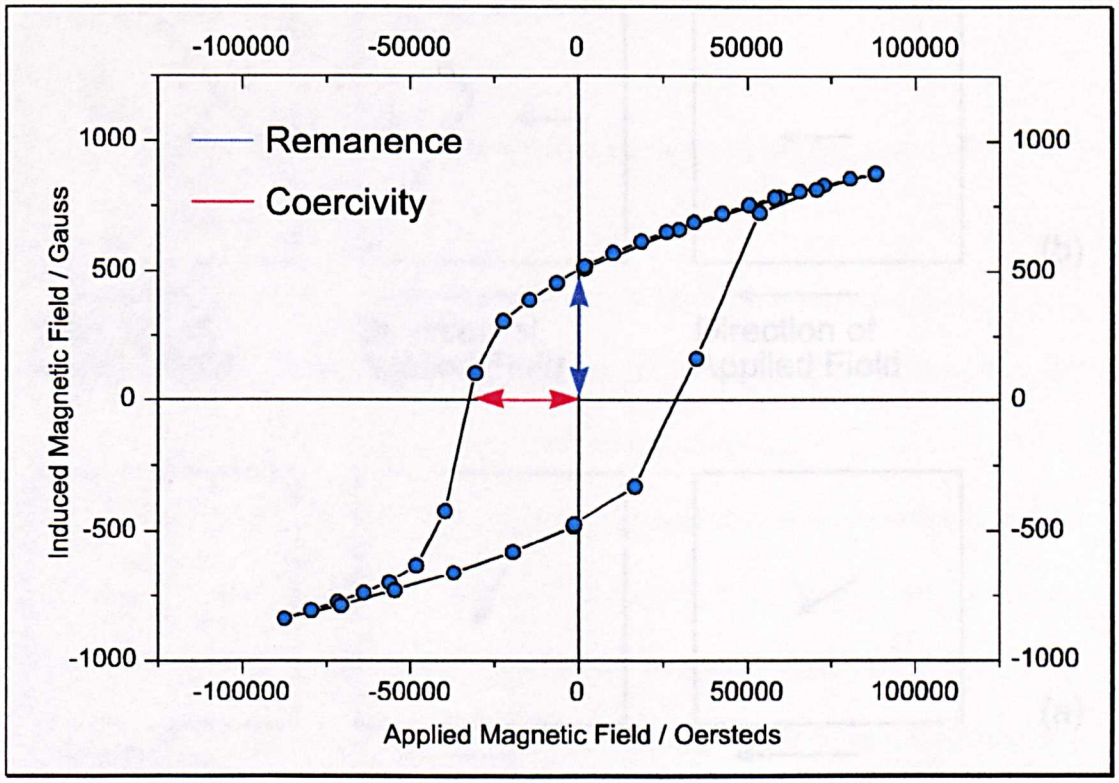

Figure 1-10 Hysteresis loop showing Remanence and Coercivity.

If the solid being demagnetised is single domain then the whole domain needs to be rotated, shown in Figure 1-11(a). In a multidomain solid there may be some domains in which the field does not need to be rotated, shown in Figure 1-11(b), in these particles the energy will be lower than those of single domain particles. Such a reduction is observed by a reduction in coercive force, therefore in hard magnetic materials it is important to reduce the number of multidomain particles to a minimum.

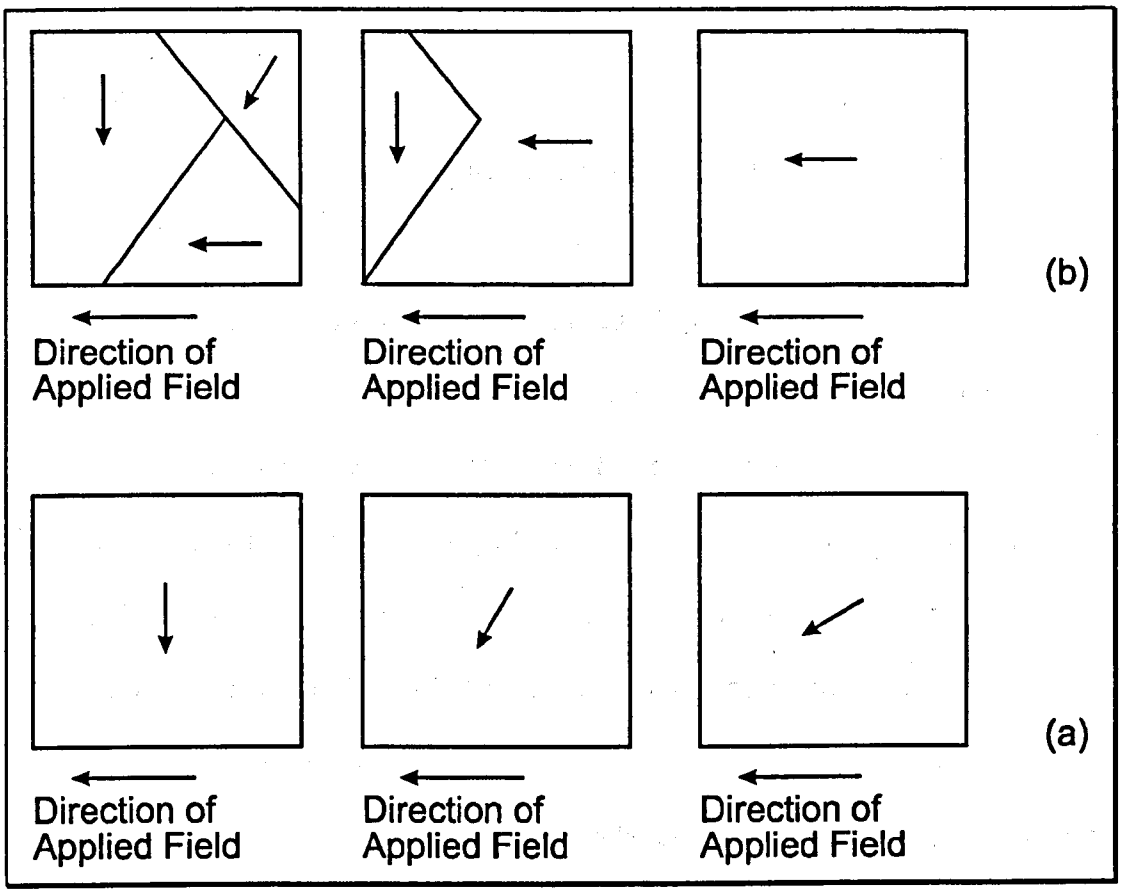

Figure 1-11 Diagram showing magnetic direction in (a) single and (b) multidomain particles being rotated by an applied magnetic field of equal intensity.

1.3.5 Modification of Magnetic Properties.

There are two methods of modifying the physical properties of magnetoplumbites:

(i) Dopant addition - the exchange of one or more elements for another.

(ii) Modification of synthetic procedure.

1.3.6 Dopant Modification.

Previous literature reports[24,25] on the doping of magnetoplumbites doped with a rare-earth metal have concentrated on the doping of magnetoplumbites other than $SrFe_{12}O_{19}$ such as $BaFe_{12}O_{19}$[24], $PbFe_{12}O_{19}$[25], and $CaFe_{12}O_{19}$[26]. There have been three

main types of doping reported for the doping of hexaferrites with rare-earth elements:

(i) $M_{1-x}Ln_xFe_{12}O_{19}$ - where the alkaline earth metal has been partially replaced.

(ii) $MFe_{12-x}Ln_xO_{19}$ - where the trivalent Fe has been replaced.

(iii) $(Ln_2O_3)_x[MO.6(Fe_2O_3)]_{100-x}$, where MO is the alkaline-earth oxide - this is where the system as a whole has had an addition.

The majority of papers on the doping of magnetoplumbites by rare-earth elements have tended to use lanthanum as the dopant. However, it has been shown that $LaFe_{12}O_{19}$ exists and is only stable over a narrow temperature range[22].

When La is used to dope[22] using method (i) above, the saturation magnetisation is reduced from $20\mu_\beta$ to $19\mu_\beta$. This reduction can be explained in the following manner: La^{3+} when doped for Sr^{2+} creates a charge imbalance, in order to compensate for this, a Fe^{3+} ion undergoes reduction to Fe^{2+}. It has been suggested that one of the trivalent Fe ions on the 2a site undergo reduction to the bivalent state[27]. This original hypothesis has since been confirmed by other workers[22]. Since the reduced Fe^{2+} has a lower magnetic moment $4\mu_\beta$, as opposed to that of Fe^{3+} $5\mu_\beta$, and since this site is aligned parallel to the direction of magnetisation, a reduction in μ is predicted and observed. It has been reported by Higuchi et al [28] that when $BaFe_{12}O_{19}$ was doped with La, using method (i) an increase in coercive force was noticed, with a maximum value being reached at $Ba_{0.85}La_{0.15}Fe_{12}O_{19}$.

Method (ii) for the doping of magnetoplumbites has tended to be concerned with the addition of highly ferromagnetic rare-earth elements such as Sm, Dy, Gd and Ho. Higuchi et al [28]reported that $Ba_{0.85}Gd_{0.15}Fe_{12}O_{19}$ showed a high coercive force > 6100 Oersteds (Oe) after heat treatment.

Doping using method (iii) has been primarily used to dope with La_2O_3. Yamamoto et al [29] reported that this method of doping stabilises the formation of the magnetoplumbite structure. This method of doping has been shown to be effective for the four main magnetoplumbites, Pb, Ca, Ba, and Sr.

Although there has been little published work on rare-earth doped hexaferrites there has been a wide range of work published on hexaferrites doped with other elements. There are many different combinations of elements which can be used[30]. If Fe^{3+} in the system is replaced with other trivalent elements then the elements Al, Cr, In, Ga, and As are examples of the dopants. If Fe^{3+} in the system is doped then provided the trivalent positive charge is matched, it can be built up of various combinations such as the following general types M(II)/M(IV), M(II)/M(V), and M(II)/M(VI) of which Ti/Co, Sn/Co, Nb/Zn, and Ti/Zn/Mn are examples.

If the bivalent alkaline-earth is partially substituted then common elements used are Ba,Sr,Ca, and La. Since La is trivalent, a Fe^{3+} is reduced to Fe^{2+} to conserve charge but this also causes a reduction in the magnetic moment. If La is doped along with Na in equal amounts then charge balance is conserved over the whole system, thus avoiding any reduction processes.

It has been reported in the literature[30] that if the barium hexaferrite system is doped with a M(II)/M(IV) combination in exchange for Fe, then a reduction in various magnetic properties is observed. The coercivity, remanence and saturation magnetisation are all reduced as the amount of dopant is increased. An example of these effects is shown in Figure 1-12, which shows the change in coercivity for various dopants at various levels.

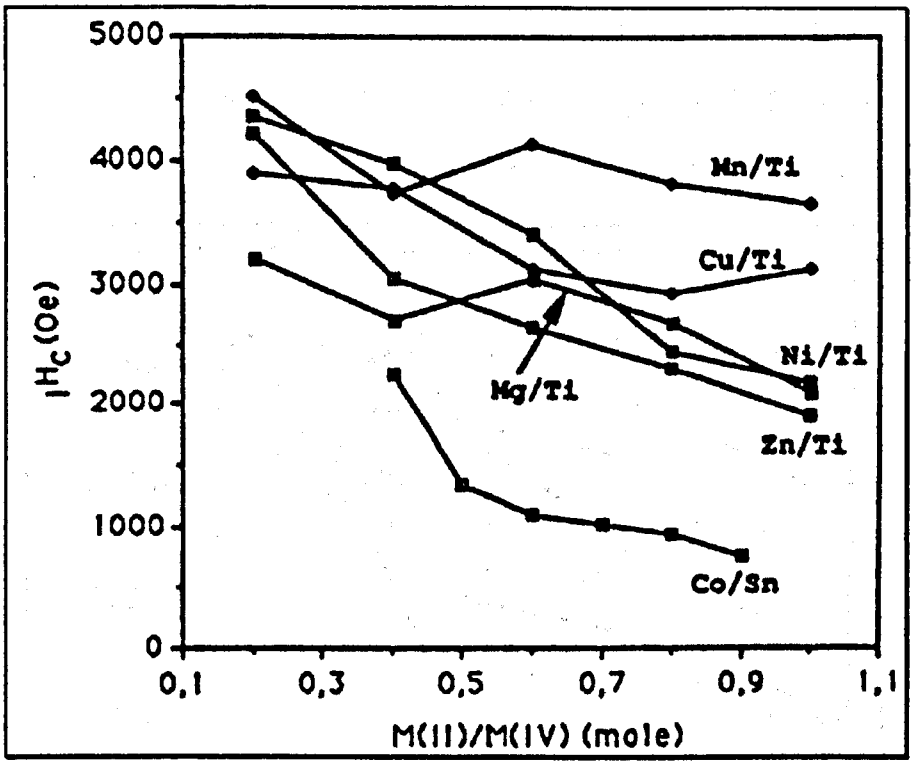

Figure 1-12 A graph showing variation in coercivity against dopant concentration for various M(II)/M(IV) systems.[30]

As can be seen from the above figure the decrease in coercivity shows an overall decrease for the Ni/Ti, Zn/Ti, and Co/Sn combinations. It is also found that a similar dependence is found for the saturation magnetisation.

Another feature of doping with this combination of elements is observed in the Mössbauer spectra recorded from the Mn/Ti and Mg/Ti doped systems[30]. It has been found that the site occupation of the dopants can be identified and that the Mn or Mg atoms occupy the $4f_1$ site whereas the Ti atoms dope randomly onto the 4f and 12k sites. This effect of doping has the effect of reducing the unit cell magnetic moment in the unit cells which have the dopant.

Data concerning the doping of M(II)/M(V) or M(II)/(MVI) for trivalent Fe have been reported[30]. A similar effect to the method of doping discussed above was found i.e. a reduction in coercivity, remanence, and saturation magnetisation. The reduction in

coercivity is relatively slow for doping levels less than 1.0/0.5 (M(II)/M(V)). The same behaviour is observed for the saturation magnetisation. A graph showing the effects of dopant on the coercivity of the system is shown in Figure 1-13.

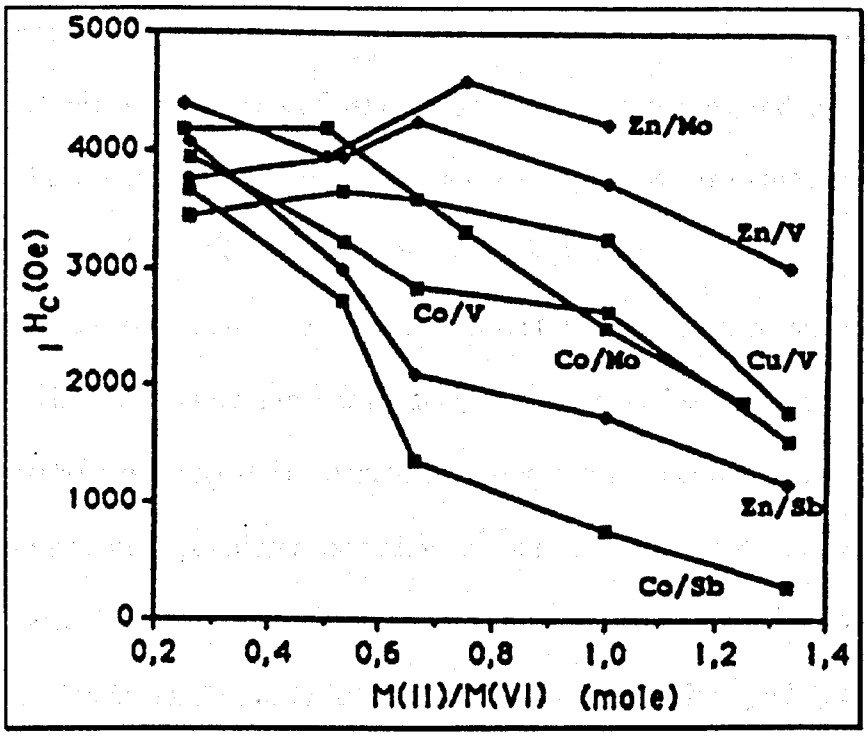

Figure 1-13 Graph showing variation in coercivity against dopant concentrations for various M(II)/M(VI) systems.[30]

The majority of reports on the effect of doping on the magnetic properties has tended to use dopants of the first type discussed here, i.e. M(II)/(MIV), and this work has led to a number of patents being granted on systems found to have magnetic properties desirable for industrial applications. The majority of such patents has tended to be granted to systems which use Ti as a dopant.

1.3.7 Synthetic route modification.

The second method of modifying the magnetic properties of $SrFe_{12}O_{19}$ is through the modification of the synthetic route.

Other than the standard calcination of metal oxides, other techniques have been used, examples are salt co-precipitation [31,32], organometallic hydrolysis [28,33], glass crystallisation[34] and hydrothermal processing[35,36]. There are many drawbacks and advantages for each method used, the main advantage in the calcination of metal oxides is the relative cheapness of the reactants. However, the major drawback of this method is the formation of multidomain particles, this is due to the high temperatures (1200-1300°C) which accelerate grain growth.

Saha et al[37] have reported the effect of calcination temperature on the magnetic properties. The authors found that as the temperature of calcination was increased the magnetic properties changed. If the material was synthesised at temperatures below 1000°C an incomplete reaction occurred, with poor magnetic properties and impurity phases present. The authors found that as the temperature is increased above 1000°C grain growth increases. Above 1250°C large crystals begin to form, while at temperatures above 1300°C grain growth being rapid with each particle essentially becoming a single crystal. The effect of increasing formation temperature on the magnetic properties is shown in Figure 1-14.

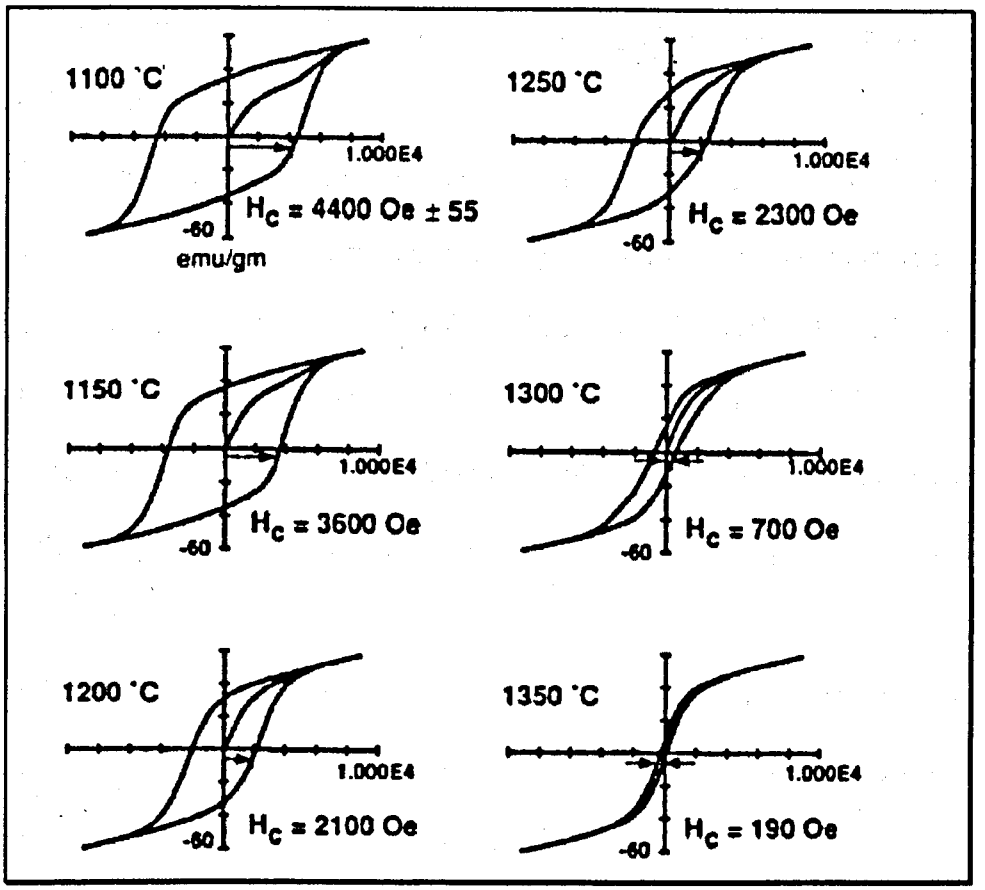

Figure 1-14 Diagram showing effect of heat treatment on coercivity.[37]

It can be seen that while the saturation magnetic moment remains constant, coercivity decreases with increasing temperature. This observation was explained in terms of the formation of multidomain particles. As the temperature, and thus crystallite size increased, the number of multidomain particles increased thus reducing the coercivity. As a result the final product had to be milled to reduce the particle size to that approaching single domain ~600 nm. The above advantages and disadvantages contrast with the chemical co-precipitation route. This route uses the relatively cheap chloride or nitrate salts of the element, which are converted to a gel using NaOH , filtered and then calcined. Due to the intimate mixing of the gel , a lower calcination temperature is used, 925°C, this reduces the grain growth and as a

result increases the number of particles which are single domain, thus no further milling is required.

One technique which has recently been used to synthesise $SrFe_{12}O_{19}$ with small particle size has been hydrothermal processing[35,38]. This involves the precipitation of a gel using NaOH from the nitrates. This gel based solution is then heated in an autoclave at 220°C for 2hrs under autogenous pressure, ~ 25 bar, and the mixture filtered after cooling. After filtration hexagonal platelike particles are formed which are small enough to require no further milling or heat treatment prior to production of the finished magnet.

The main advantage of the hydrothermal route is the ease of synthesis, approximately 4 hours, allowing for the heating and cooling of the mixture. This contrasts with the calcination of the metal oxides, which require heat treatments at 1200-1300°C for many days to achieve phase purity. The co-precipitation route requires heating at 925°C for 2 hours to achieve phase purity, but the formation and filtration of the gel can take up to 24 hours.

The other two methods, organometallic hydrolysis and glass crystallisation, produce magnets which have good magnetic and physical properties. However, both methods use exotic salts of the metals which are expensive and sometimes difficult to purchase.

Since there has not been a direct comparison of the effect of synthetic procedure on the magnetic properties, one aim of this work has been to compare materials formed from different synthetic routes with different dopants.

1.4 References.

1. J Houseman and D.A Johnson, *Interdisciplinary Science Reviews*, 1991, **16**, 245.
2. H Hegeland, *The Quantity Theory of Money*, Kelley, New York, 1969, p. Chapter 2.
3. D Hume, *Essays, Moral, Political and Literary*, Liberty Classics, Indianapolis, 1985, pp. 281-326.
4. J.M Keynes, *A Treatise on Money*, Macmillan, London, 1930, pp. 152-163.
5. C.M Cipolla, *Before the Industrial Revolution*, Methuen, London, 2nd edn., 1981, pp. 230-233.
6. P.J Bakewell, *The Cambridge History of Latin America*, Cambridge University Press, Cambridge , 1984, pp. 105-151.
7. C.F Park and R.A Mcdiarmid, *Ore Deposits*, Freeman, San Francisco, 2nd edn., 1970, pp. 478-488.
8. P.J Bakewell, *Silver Mining and Society in Colonial Mexico; Zacatecas 1546-1700*, Cambridge University Press, Cambridge, 1971, p. Chapter 6.
9. T.A Rickard, *The Canadian Institute Of Mining and Metallurgy*, 1936, 23.
10. J Percy, *Metallurgy; Silver and Gold Part 1*, John Murray, London, 1880, pp. 576-608.
11. M Bargallo, *La Mineria y La Metalurgica En La America Espanola Durante La Epoca Colonial*, Mexico, 1955, p. 194.
12. J.R.Partington, *General and Inorganic Chemistry*, Macmillan, London, 4th edn., 1966, p. 334.

13. F Habashi, *CIM Bulletin*, 1982, **75**, 133.

14. J Percy, *Metallurgy; Silver and Gold Part 1*, John Murray, London, 1880, p. 656.

15. J Percy, *Metallurgy; Silver and Gold Part 1*, John Murray, London, 1880, pp. 73-84.

16. J.A Grieg, G.A.Davies, *Separation Processes in Hydrometallurgy*, Ellis Horwood, Chichester, 1987, pp. 35-48.

17. J.E Dutrizac, *Hydrometallurgy*, 1992, **29**, 1.

18. X Obradors, X Solans, A Collomb, D Samaras, J Rodriguez, M Pernet and M Font-Altaba, *J. Solid State Chem.*, 1988, **72**, 218.

19. K Kimura, M Ohgaki, K Tanaka, H Morikawa and F Marumo, *J. Solid State Chem.*, 1990, **87**, 186.

20. J Fontcuberta and X Obradors, *J. Phys. C: Solid State Phys*, 1988, **21**, 2335.

21. J Fontcuberta, W Reiff and X Obradors, *J. Phys. C: Condensed Matter*, 1991, **3**, 2131.

22. A.M. van Diepen and F.K.Lotgering, *J. Phys. Chem. Solids*, 1974, **35**, 1641.

23. C Kittel, *Introduction to Solid State Physics*, John Wiley & Sons, New York, 7th Edn 1996.

24. V Vasiljev, L Tulchinsky and G Yaglo, *Mater. Sci. Forum*, 1990, **62-64**, 527.

25. H Yamamoto and M Nagakura, *IEEE Trans. Magn.*, 1987, **MAG-23**, 294.

26. Ming-Pan Hung and Mao-Tsong Wu, *Proc.Natl.Sci.Counc.ROC(A)*, 1983, **7**, 52.

27. Ch Sauer, U Kobler, W Zinn and H Stablein, *J. Phys. Chem. Solids*, 1978, **39**, 1197.

28. Kazuo Higuchi, Shiegeharu Naka and Shin-Ich Hirano, *Advanced Ceramic Materials*, 1986, **1**, 104.

29. H Yamamoto, M Nagakura and H Terada, *IEEE Trans. Magn.*, 1990, **26**, 1144.

30. U Meisen and A Eiling, *IEEE Trans. Magn.*, 1990, **26**, 21.

31. C.W.Chang, M.S.Tzeng and S.J.Wang, *J. Mater. Sci. Lett.*, 1990, **9**, 832.

32. S Kulkarni, J Shrotri, C.E Deshpande and S.K. Date, *J. Mater. Sci.*, 1989, **24**, 3739.

33. K Haneda, C Miyakawa and K Goto, *IEEE Trans. Magn.*, 1987, **MAG-23**, 3134.

34. K Oda, T Yoshio, K O-Oka and F Kanamaru, *J. Mater. Sci. Lett.*, 1984, **3**, 1007.

35. A Ataie, I.R Harris and C.B Ponton, British Ceramic Proceedings, W.E Lee and A Bell, University of Leeds, 20 December, 1993-22 December, 1993, Institute of Materials, London, 1994, pp. 273-281.

36. C.H. Lin, Z.W Shih, T.S. Chin, M.L Wang and Y.C Yu, *IEEE Trans. Magn.*, 1990, **26**, 15.

37. B Saha and W Yetter, *J. Appl. Phys.*, 1993, **73**, 6260.

38. A Ataie, I.R.Harris and C.B.Ponton, *J. Mater. Sci.*, 1995, **30**, 1429.

CHAPTER 2 - EXPERIMENTAL TECHNIQUES.

2.1 XRD - X-Ray Diffraction.

The basic theory of X-ray diffraction has been understood since the early part of this century, and is now used for structural characterisation. X-ray diffraction as a structural technique is explained in well known chemical and physical textbooks[1-3], and is only briefly described here. In order to understand X-ray diffraction, it is best to start with a basic model i.e. a one-dimensional grating.

2.1.1 The Diffraction of Light by an Optical Grating.

If light is passed through a grating, glass with slits, two main processes can occur.

(i) transmittance - the light passes through unchanged.

(ii) diffraction - this occurs when slit spacing is only slightly larger than the wavelength of the light.

In a glass where the second process occurs, each slit acts as a point source for a wave shown in Figure 2-1.

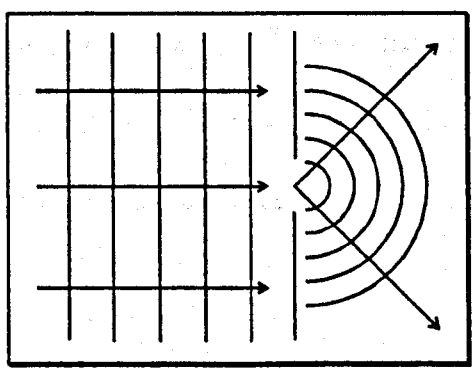

Figure 2-1 The effect of a slit acting as a point source on a parallel wave.

When these waves interact there will be regions of constructive and destructive interference, shown in Figure 2-2.

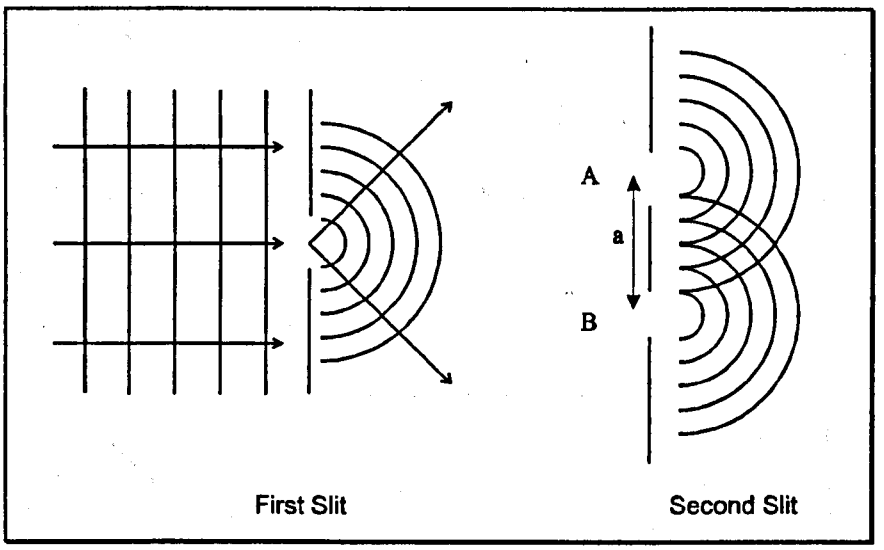

Figure 2-2 The effect of two slits on a parallel wave, showing the interference which occurs.

In a light source, containing more than a few beams, the interference results in regions of strong intensity, and regions of little or no intensity. The directions where interference occurs are governed by the wavelength of the light, λ, and separation of the slits.

If two beams constructively interfere with each other, then they must be in phase with each other, i.e. a multiple of a full wavelength, $n\lambda$. However, since both beams will be moving out at an angle from the source, θ, the following relationship will be valid

$$AB = n\lambda \qquad (2.1)$$

But, $$AB = a \sin\theta \qquad (2.2)$$

$\therefore$ $$a \sin\theta = n\lambda \qquad (2.3)$$

The above equation defines where constructive interference will occur.

Since solids are 3-dimensional, in order to achieve the same effect, X-rays are used as their wavelength is approximately the same as the "slits" used in the model put forward above.

2.1.2 The Bragg Equation[4].

Bragg's approach was to consider the crystals as being built in layers, or planes, such that each acts as a semi-transparent mirror. The planes allow some of the X-ray beams to be reflected at the same angle as the angle of incidence.

The derivation can be shown pictorially:

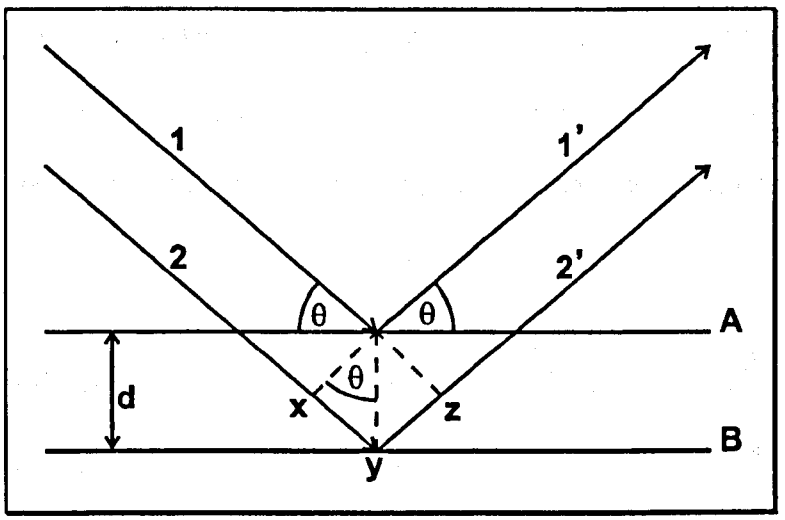

Figure 2-3 Diagram used for the derivation of Bragg's law.

The incident beams 1 & 2 are reflected by A & B to form beams 1' and 2', the condition under which these beams are in phase with each other is approached as follows.

Beam 22', shown in Figure 2-3, has to travel a further distance, xyz, than beam 11'. For 1'and 2' to be in phase with each other, xyz must equal n, i.e. a whole number of wavelengths. The perpendicular spacing, d, and angle of incidence, θ, Bragg angle, are both related to xy by :

$$xy = yz = d \sin\theta \qquad (2.4)$$

$$\Rightarrow \quad xyz = 2\,d \sin\theta \qquad (2.5)$$

$$\text{Since} \quad xyz = n\lambda \qquad (2.6)$$

$$\Rightarrow \quad n\lambda = 2\,d \sin\theta \qquad (2.7)$$

When the above equation, (2.7), Bragg's Law, is satisfied the reflected beams are in phase and thus constructively interfere. If the angle is not correct then usually interference of a destructive nature will occur. It can be seen that many solutions are possible i.e. n= 1,2,3 however, it is usual to put n=1 and work from there.

2.1.3 d-spacings and their use.

It is possible to work back from d-spacings to find where the planes that diffract the X-rays intersect the unit cell, and from here work out a general structure.

Working with orthogonal unit cells and simplifying the procedure the equation is:

$$\frac{1}{d^2} = \frac{h^2}{a^2} + \frac{k^2}{b^2} + \frac{l^2}{c^2} \qquad (2.8)$$

where h,k,l are the Miller Indices , a,b,c are the unit cell parameters. The Miller Indices are the reciprocal of the lattice intercepts as shown in Figure 2-4.

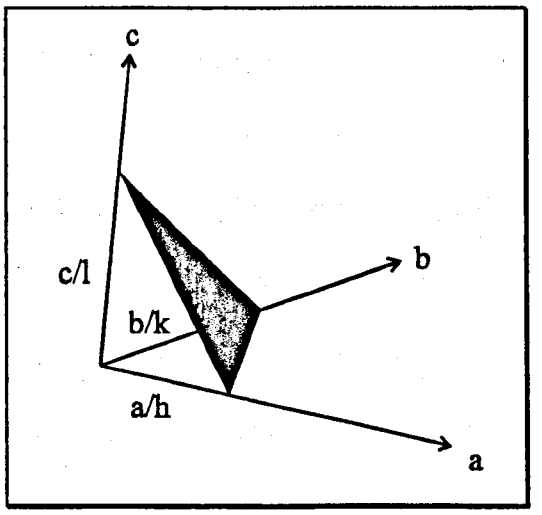

Figure 2-4 Diagram showing a plane intersecting the axes, and the Miller indices.

2.1.4 The Powder Method.

The basic principle of the powder method is shown in Figure 2-5. A monochromatic beam of X-rays strike the powdered sample arranged randomly such that every orientation is possible. As a result, for every diffraction plane there are some crystals correctly oriented at the Bragg angle and hence some diffraction occurs.

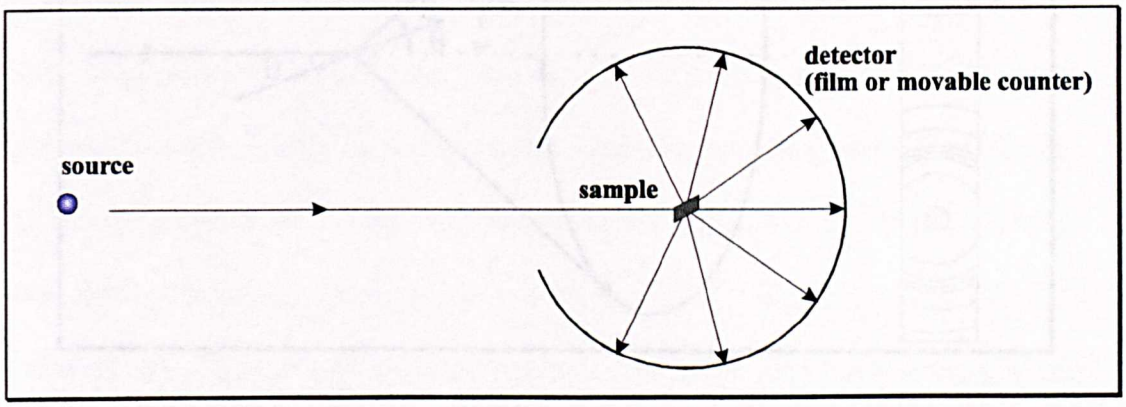

Figure 2-5 A schematic representation of the powder method.

The diffracted beam can be detected by one of two means, a photographic plate surrounding the sample, or a movable detector, such as a Geiger-Müller tube connected to a computer. The original photographic method, called the Debye-Scherrer method, is little used in modern X-ray diffraction practices but provides an explanation from which other methods have developed. For any set of lattice planes the diffracted radiation forms a cone. The only requirement for diffraction to occur is that the plane be at the angle θ, see Figure 2-6. In a randomly oriented sample crystals are present at every angle and therefore the diffracted beams appear to be diffracted from the sample in a cone. If the Bragg angle is θ then the angle between the diffracted and undiffracted beam is 2θ and the angle of the cone 4θ. Each set of planes gives its own cone of radiation. The cones are detected using a cylindrical photographic film surrounding the sample, each one intersects the film as two short

arcs symmetrical around the two holes, where the incident and undiffracted X-rays pass.

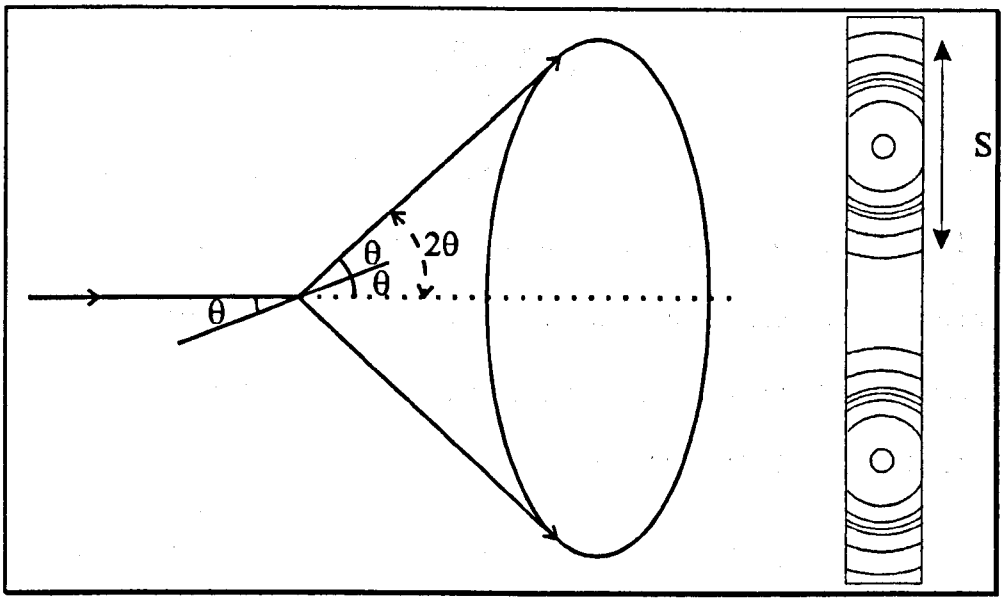

Figure 2-6 Formation of a cone of diffracted radiation, with a schematic of the pattern obtained by this method..

The d-spacing can be obtained from the film using equation 2.9:

$$\frac{S}{2\pi R} = \frac{4\theta}{360} \qquad (2.9)$$

where S is the separation between pairs of corresponding arcs , and R is the film radius from the sample. When R is known it is relatively easy to determine 2θ and subsequently d.

A modern diffractometer works in a similar way. The major difference being that rather then use a photographic plate surrounding the sample, a movable detector rotates around the sample. The detector can collect accurate positional and intensity data, both quickly and easily. This enables the phase composition to be determined in less than an hour, with the recorded pattern being matched against standard patterns.

2.1.5 d-spacing and unit cell sizes.

In an orthogonal system the d-spacing for any set of planes is given by :

$$\frac{1}{d^2} = \frac{h^2}{a^2} + \frac{k^2}{b^2} + \frac{l^2}{c^2} \qquad (2.10)$$

where d is the d-spacing , h, k, l are the Miller indices, and a, b, c are the unit cell dimensions. There are equivalent equations for the five other crystal systems. It is possible to calculate unit cell sizes from accurate diffraction data. Calculation of unit cell parameters is usually carried out using computer modelling techniques using a variety of programs, an example of such a program is DICVOL91[5] which has been used in this work.

Since the calculation of unit cell parameters is dependent upon the d-spacing, highly accurate data is required. As a result, X-ray powder diffraction patterns for determining unit cell size parameters are measured over a long period of time (ca. 18hr) with fine step sizes. A pattern for determining phases in a solid mixture usually has a resolution of 0.02°, whereas a pattern for determining unit cell parameters has a resolution of 0.01°. Coupled to the higher resolution is an increased counting time to increase signal to noise ratio.

Although the collected data may be excellent even if the sample or instrument are incorrectly aligned, the data will be inaccurate. To combat this, an internal standard giving peaks of known position and intensity is used, in this work Si. Once the data has been collected the peaks assigned to Si are compared with the standard positions. The overall result is highly accurate data which can give reliable unit cell parameters.

2.1.6 Peak Intensities

There are many factors which affect peak intensity, of which a few are described below.

i) Structure Factor.

This accounts for the intensity of the peak resulting from the position of the atom in the unit cell and the atom type. If an atom has a high atomic number then it will scatter X-rays better than an element with a low atomic number, e.g. Cs scatters better than Li.

ii) Multiplicity Factor.

For a cubic system, lattice planes (013), (031), (103), (130), etc. all have the same d-spacing as can be shown using Equation (2.8), where a=b=c. In a powder XRD pattern the variable co-ordinate is d-spacing, therefore reflections which give rise to the same d-spacing will be superimposed. As a result a more intense peak will be observed.

iii) Preferred orientation.

This occurs if the powder is poorly ground or if the powder is not completely oriented randomly. This effect can cause some intensities to be increased while others are decreased.

iv) Temperature factor.

Thermal vibrations of atoms cause a decrease in the observed peak intensity with an increase in background scatter. This effect is usually only important for experiments performed at high temperature.

2.1.7 Particle size measurement.

From X-ray powder diffraction data it is possible to measure the crystallite size from the effect of line broadening on the diffraction pattern. The relationship between the mean dimension of the crystallites in a powder, D, and the pure X-ray diffraction broadening, β, was first determined by Scherrer[6], and is discussed in detail by Klug and Alexander[7].

Scherrer related the mean dimension, D, to the pure diffraction broadening, β, by the equation;

$$D = \frac{K\lambda}{\beta \cos\theta} \qquad (2.11)$$

where K is a constant approximately equal to unity, θ is the diffraction angle and λ is the wavelength used in the diffraction. The Scherrer equation allows relative crystallite sizes to be calculated, such as in a series of related compounds, but should not be used for absolute measurements.

2.1.8 Experimental Procedures.

The collection of X-ray powder diffraction data is routinely carried out on a diffractometer, such an instrument is shown in Figure 2-7:

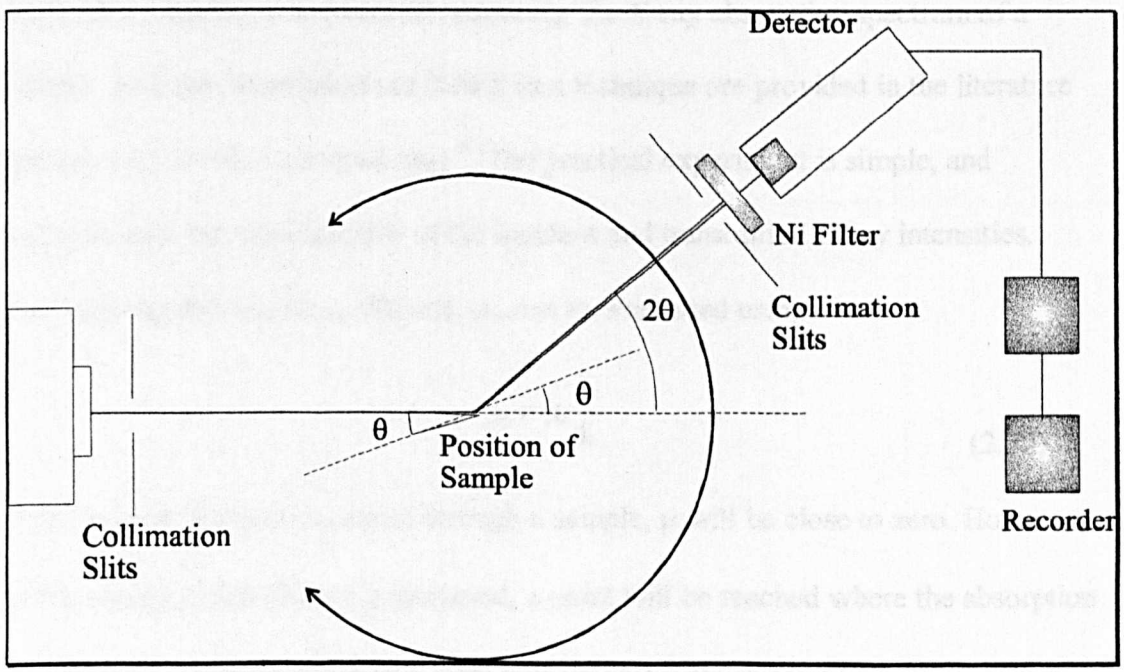

Figure 2-7 Schematic representation of a standard X-ray diffractometer.

The X-rays are generated in an X-ray tube, where electrons are bombarded against a metal target, usually copper. This bombardment results in the evolution of X-rays, the X-rays are then collimated into a pencil like beam. The beam then passes through

the sample, which is rotating around a central axis, as the beam passes through the sample it is diffracted. This diffracted beam is then passed through a further set of collimation slits, to remove X-ray scattering, prior to passing through a filter, in this case Ni. The filter is used to remove any radiation which is not used for the collection of data, in this example Cu-K_β. The X-rays are then counted in a Geiger-Müller tube moving around the central axis, at an angle of rotation twice that of the sample. A more in-depth review of this type of X-ray design can be found in the literature[1].

2.2 XAFS - X-ray Absorption Fine Structure.

2.2.1 XAFS - General Theory

An XAFS experiment consists of measuring the X-ray absorption spectrum of a sample. In-depth descriptions of XAFS as a technique are provided in the literature and are only briefly described here [8]. The practical experiment is simple, and involves only the measurement of the incident and transmitted X-ray intensities. From this an absorption coefficient, μ, can be evaluated using -

$$\mu = \ln \frac{I_o}{I_t} \qquad (2.12)$$

If low energy X-rays are passed through a sample, μ will be close to zero. However, as the energy of the X-rays is increased, a point will be reached where the absorption coefficient, μ, increases sharply. This point is called the "absorption edge", where the X-rays are of sufficient energy to "eject" a photoelectron from the sample, shown in Figure 2-8.

The electron ejected will be from the K or L sub shells and the energies of the X-rays will usually be between 1-40keV, any further increase in X-ray energy is translated

into kinetic energy of the ejected photoelectron. At the absorption edge the energy of the X-ray , hμ, will be the same as the binding energy of the ejected E_b. The situation is described pictorially is Figure 2-9.

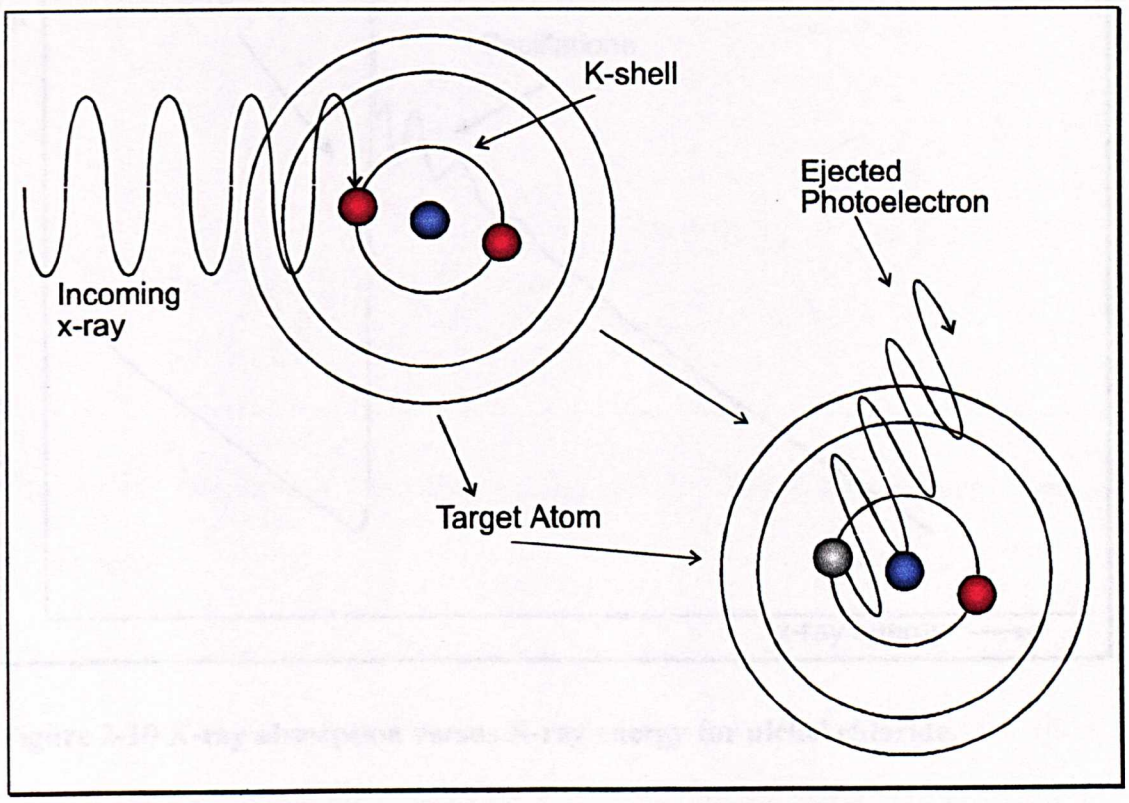

Figure 2-8 Diagram showing ejection of core electron by X-ray

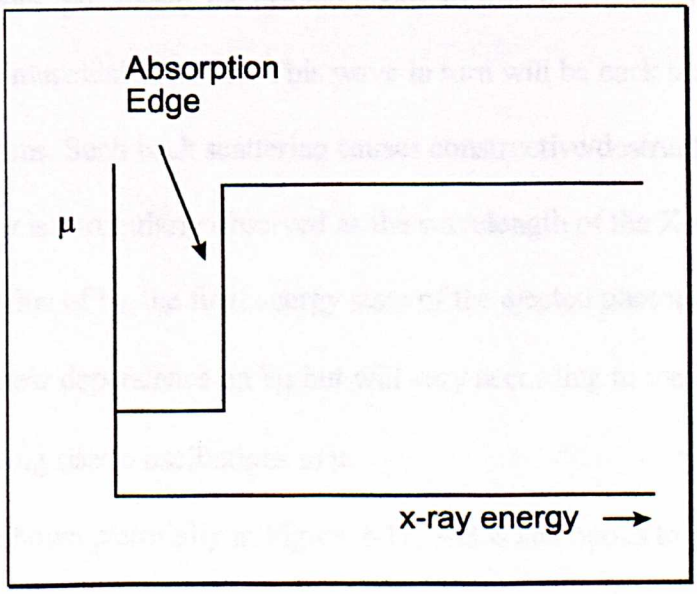

Figure 2-9 Diagram showing the expected X-ray absorption versus X-ray energy.

However the simple step is not observed, the observed result is shown in Figure 2-10.

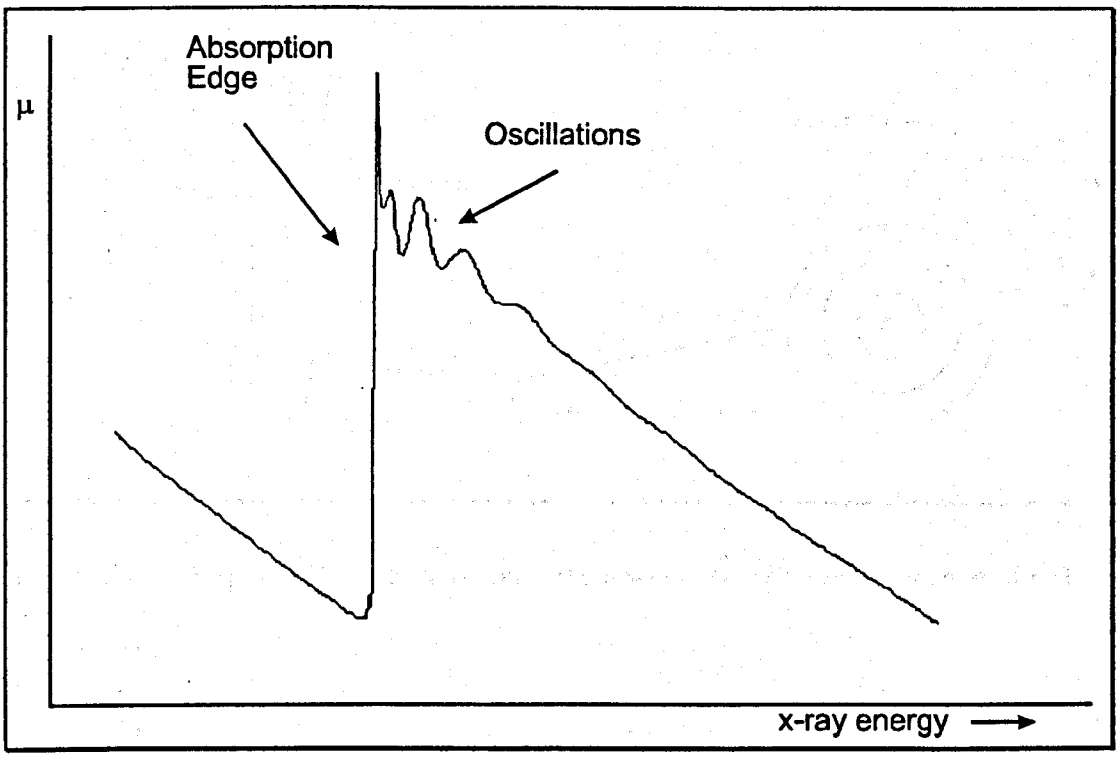

Figure 2-10 X-ray absorption versus X-ray energy for nickel chloride.

The explanation for the observation of an oscillatory type function is that the electron has wave properties, put simply the ejected photoelectron moves out of the atom as a spherical wave, sinusoidal in nature. This wave in turn will be back scattered by neighbouring atoms. Such back scattering causes constructive/destructive interference. This is particularly observed as the wavelength of the X-ray changes. As a result the value of E_f, the final energy state of the ejected photoelectron, will not simply have a linear dependence on $h\mu$ but will vary according to the inference patterns, this giving rise to oscillations in μ.

The situation is shown pictorially in Figure 2-11, and is analogous to a ripple tank experiment, the difference being that XAFS occurs on the atomic scale.

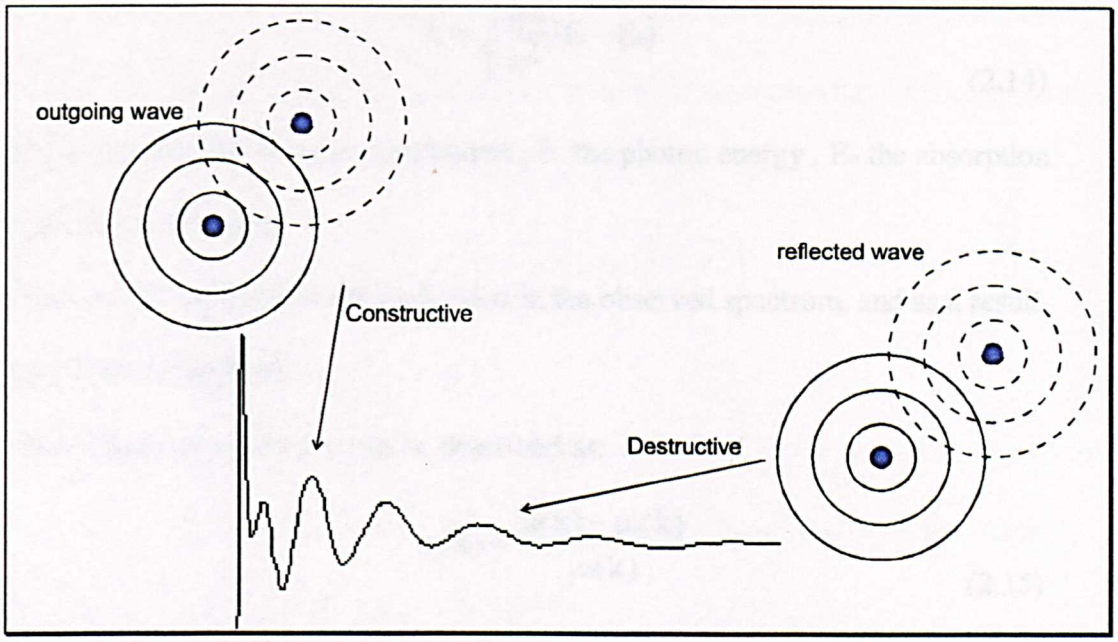

Figure 2-11 Diagram showing constructive and destructive interference of out going wave.

It is possible to derive information, such as bond length and co-ordination numbers, from the oscillations. The explanation for this is due to the sine wave observed, this wave being dependent upon the back scattered wave, with a periodicity dependent on the distance from the source (central) atom. Since the atoms do not move from their sites by a large degree, it is possible to deduce a structure from the sinusoidal wave formed.

2.2.2 XAFS - Mathematical Treatment

Following on from a simplified introduction to the basic theory of XAFS a mathematical treatment can now be approached.

When the photoelectron has been ejected, its wavelength will be determined by:

$$\lambda = \frac{2\pi}{k} \tag{2.13}$$

where k , the photoelectron wave-vector, is determined by:

$$k = \sqrt{\frac{2m}{\hbar^2}(E - E_o)} \tag{2.14}$$

where m is the rest mass of the electron , E the photon energy , E_o the absorption edge threshold energy.

These XAFS oscillations are embedded in the observed spectrum, and as a result have to be normalised.

The normalisation process can be described as:

$$\chi(k) = \frac{\mu(k) - \mu_o(k)}{\mu_o(k)} \tag{2.15}$$

where μ_o is the structureless absorption edge.

A simple picture of XAFS is based on the single scattering of an ejected photoelectron by the atoms in a co-ordination shell surrounding the core-atom. This model gives an expression for $\chi(k)$:

$$\chi(k) = \sum_j A_j(k) \sin[2kr_j + \phi_j(k)] \tag{2.16}$$

where r_j is the radial distance away from the central atom to the atom in the j_{th} co-ordination sphere. Φ_j is the total phase shift due to the interaction of the photoelectron with the central atom, and scattering from atoms in the j_{th} shell.

The summation extends over j co-ordination shells and k is the photoelectron wave vector.

The amplitude function A, which represents the total scattering of the j_{th} shell, is given by:

$$A_j(k) = \left(\frac{N_j}{kr_j^2}\right) F_j(k) \exp\left(-2\sigma_j^2 k^2\right) \tag{2.17}$$

where N_j is the number of atoms, and σ is the root mean square deviation of the interatomic distance about r_j i.e. the Debye-Waller factor. The value of σ has two

components σ_{stat} and σ_{vib} which describe the static disorder and thermal vibrations. The amplitude $F_j(k)$, which accounts for elastic electron back-scattering amplitude $f(\pi,k)$ and inelastic effects, is given by

$$F_j(k) = f(\pi,k)\exp\left(\frac{-2r_j}{\lambda}\right) \qquad (2.18)$$

where λ is the inelastic mean-free path.

It should be noted that $f(\pi,k)$ is the XAFS back-scattering factor, which is a function based upon the scattering atoms. The quantities of this factor and $\phi(k)$, the phase shift, have been calculated by Teo and Lee[9].

If $\chi(k)$ is Fourier transformed i.e.

$$f_n(r) = \left(\frac{1}{2}\pi\right)^{1/2} \int_{k_{min}}^{k_{max}} k^n \chi(k)\exp(2ikr)\,dk \qquad (2.19)$$

the result is a function which exhibits a series of peaks at $r=r_j-a_j$, where a_j, a correction to the calculated distances, arises as $\phi(k)$ is not included in the transform, k^n is used to weight the data, where certain regions are emphasised.

Since the transformation is over a finite region, ripples are introduced from the termination points. The ripples can be minimised using mathematical functions.

It is usual to computer fit the data against a theoretical model, this theoretical model usually being formed from standard parameters. The model is then adjusted until the experimental data matches the model data i.e. the two sets of curves match. In general the parameters which are modified are N, r, and σ i.e. co-ordination number, bond length and Debye-Waller factors.

2.2.3 XAFS - The Normalisation Process.

Before any analysis of the data can occur, the raw data must first be normalised, such that the XAFS oscillations can be observed. The process usually proceeds in the following manner.

(i) The raw data, i.e. counts from the scintillation counters, are usually calibrated. This process usually involves a few stages but, nevertheless, is important as any error here will cause problems later on. The program used to carry out this process is EXCALIB, on the Daresbury computer network.

(ii) The background spectra are then subtracted, leaving the XAFS oscillations, this process usually follows five stages:

(a) The E_o, the absorption energy, is found and then used as a standard against which the observed oscillations can be considered. The E_o can be changed from the absolute value as this makes the following stages easier to process, and is fundamental to the penultimate stage.

(b) The pre-edge absorption is then subtracted, since this absorption is approximately linear, the process simply involves extending the absorption through the XAFS region, shown in Figure 2-12.

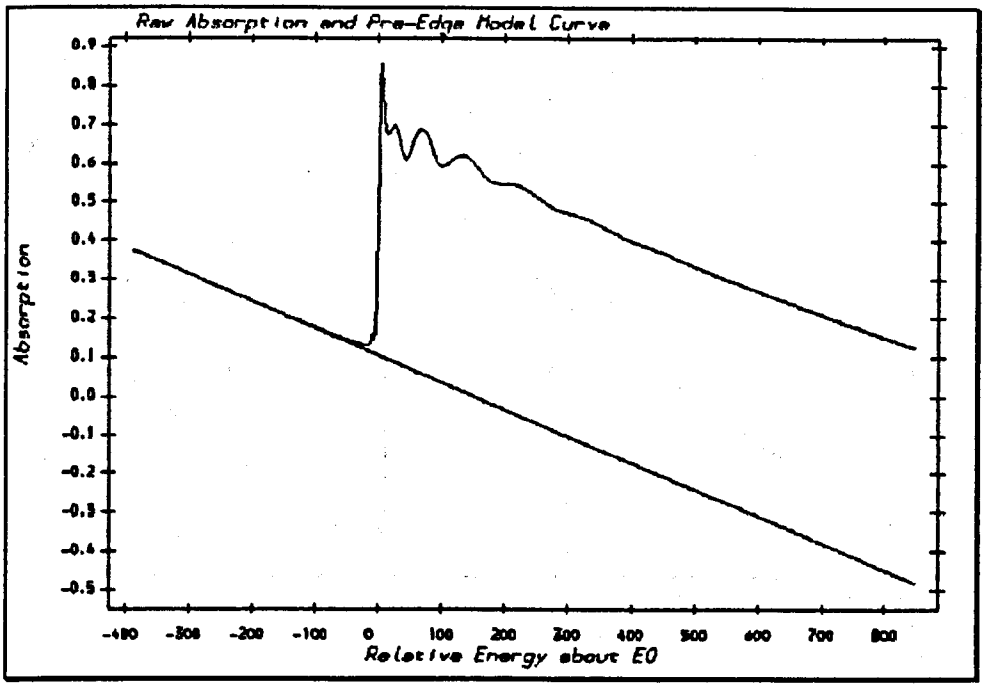

Figure 2-12 Diagram showing the pre-edge subtraction curve.

(c) The next stage of the process is to remove the smoothed atomic absorption factor μ_0. This process involves the fitting of a polynomial such that it goes through the centre of the oscillations. Usually the polynomial will be placed such that it goes through the centre of the XAFS oscillations i.e. 30-50 KeV above the edge jump, shown in Figure 2-13.

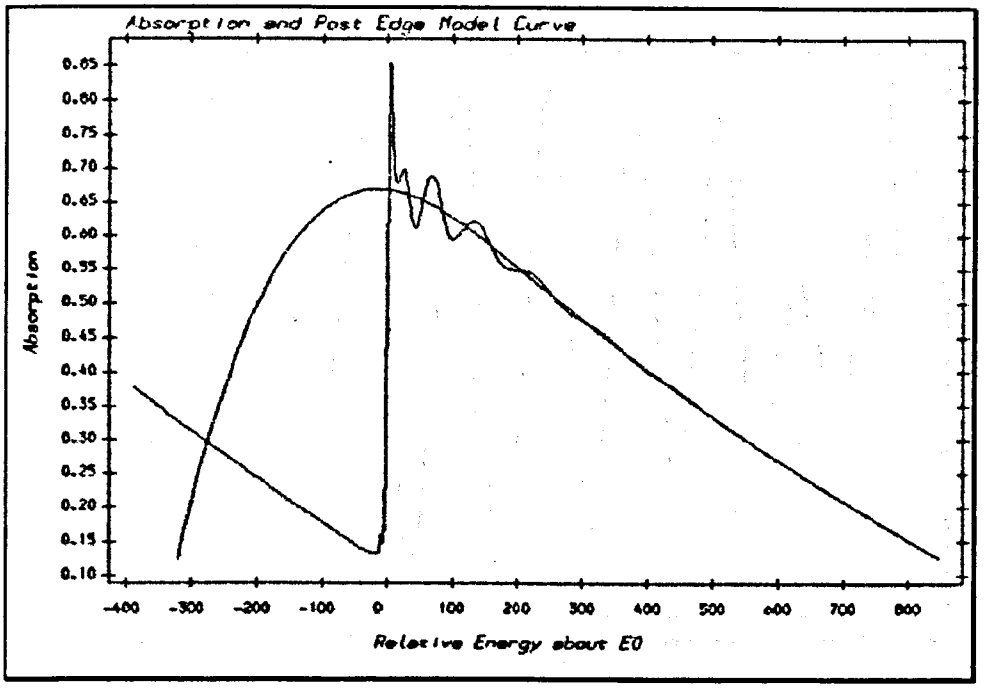

Figure 2-13 Diagram showing post-edge subtraction curve.

(d) The fourth stage is to extract the XAFS oscillations, by subtracting the pre- and post-edge polynomials, and converting the x-axis from energy to $k=(2\pi/\lambda)$ where λ is the electron wavelength above the edge jump E_o. The XAFS oscillations are then multiplied by k^3, which increases the amplitude of oscillations at large k, shown in Figure 2-14.

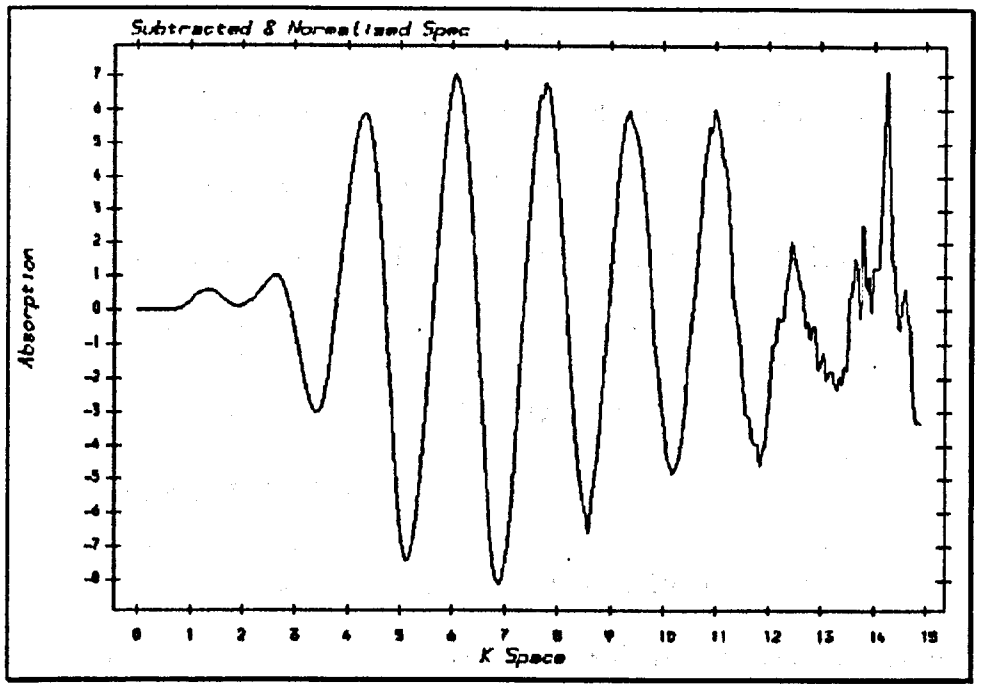

Figure 2-14 Diagram showing XAFS oscillations after subtraction of pre- and post- edge curves.

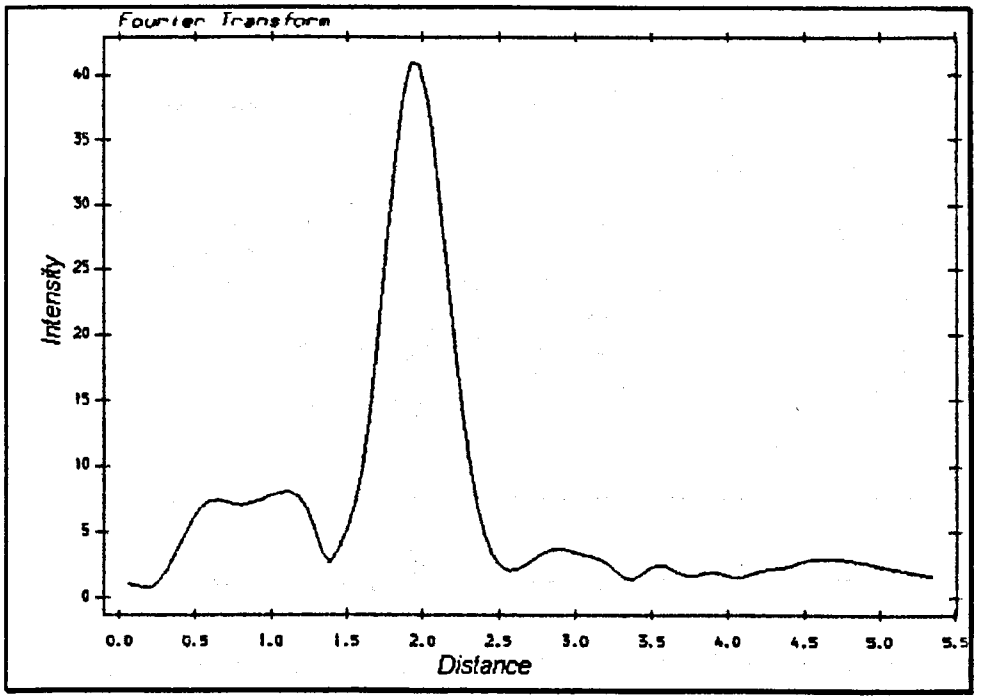

Figure 2-15 Fourier transformation of XAFS oscillations.

(e) The final stage is to Fourier transform the XAFS data, to obtain a radial distribution function. This will result in a plot showing peaks at certain radii away from the core atom, shown in Figure 2-15.

The normalisation process is carried out using the program EXBACK on the Daresbury network. After normalisation the next stage is to fit the data using the EXCURV92[10] program, again on the Daresbury network.

2.2.4 Synchrotron Radiation.

Synchrotrons are particle accelerators, first used in the 1940's to study the structure of matter. In essence a synchrotron is a facility in which charged particles, usually electrons but positrons can be used, are accelerated to relativistic velocities ~99.995% of the speed of light, these particles are then stored in a storage ring, where they are subsequently used.

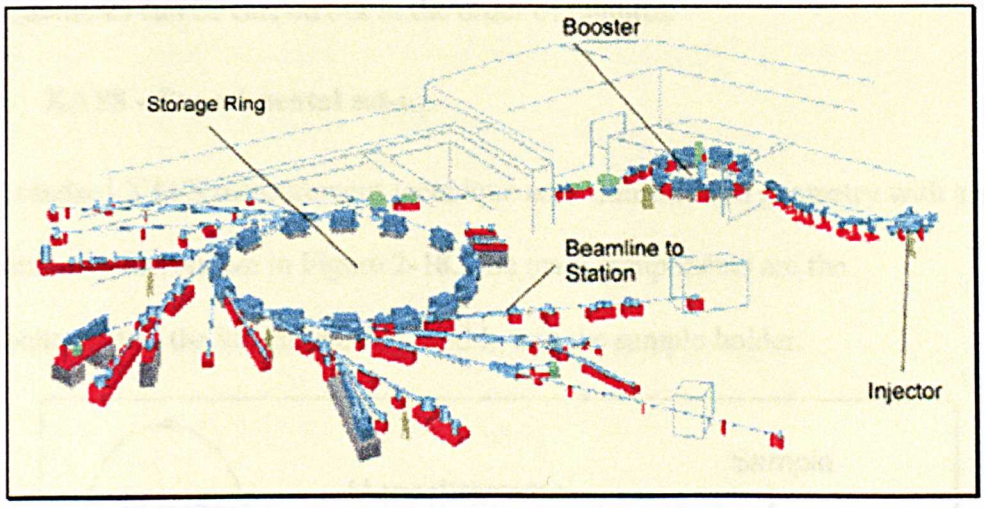

Figure 2-16 Illustration of the synchroton facility at Daresbury laboratory.

In the storage ring the particles are constantly being affected by a magnetic field, such that the particles circulate in a circular orbit. A property of a particle travelling in such a manner is the emission of electromagnetic radiation. The radiation, emitted

along a tangent, is "white" and covers all frequencies, dependent on the particle's energy.

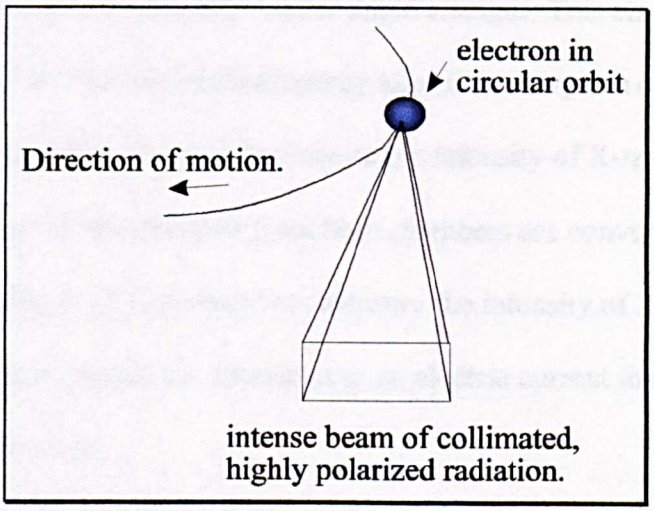

Figure 2-17 Illustrating emission of X-rays from the synchrotron.

One of the favourable properties of a synchrotron is that the radiation is emitted in a pencil like, highly collimated beam. The X-rays produced are so intense that XAFS measurements can be carried out in the order of minutes.

2.2.5 XAFS - Experimental set-up.

The standard XAFS measurement technique uses transmission geometry with a set-up similar to that shown in Figure 2-18. The main components are the monochromator, the ion chambers I_o and I_t, and the sample holder.

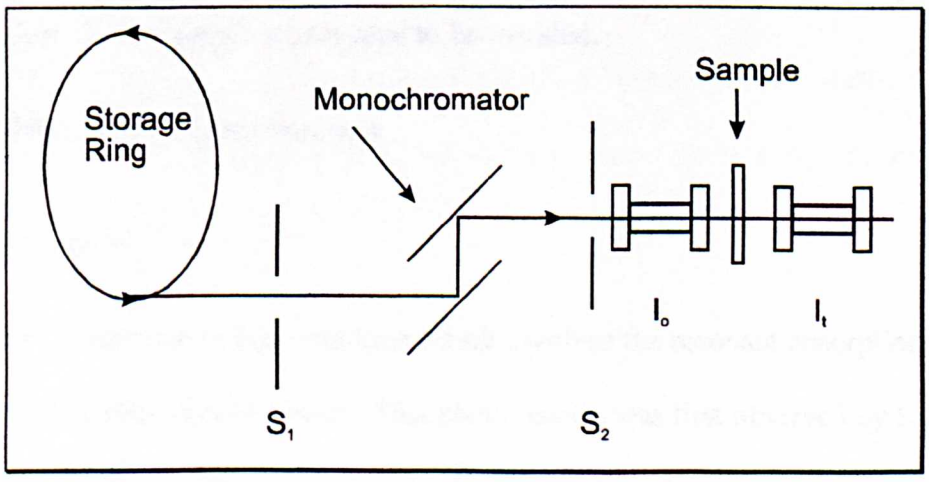

Figure 2-18 Experimental set-up for transmission XAFS experiments.

The monochromator is used to convert the white radiation produced by the synchrotron into radiation of a fixed wavelength. During the experiment the wavelength changes, as the monochromator angle changes. This change is then used to measure the oscillations in absorbed energy after the absorption edge.

The ion chambers I_o and I_t are used to measure the intensity of X-rays before and after the sample, the values obtained from both chambers are converted to absorption values using equation 2-12. Ion chambers measure the intensity of X-rays through the ionisation of gases, which are measured as an electric current that flows across two highly charged plates.

The sample is placed in the sample holder. There are many ways of placing the sample in the beam, the most common is to make a pellet of the sample and place this on the sample holder. The main advantage of using this technique is the lack of pinholes in the sample. If, however, the amount of sample required precludes the formation of a pellet then the sample can be diluted using BN, or another light compound such as powdered polyethylene.

S_1 and S_2 in Figure 2-18 refer to mechanical slits on the beam line. These slits are used to change the beam characteristics, such as width, they are useful in situations where the sample area is smaller than the standard profile of the beam, or when there are pin holes in the sample which need to be avoided.

2.3 Mössbauer Spectroscopy

2.3.1 Theory

Mössbauer spectroscopy is a technique which involves the resonant absorption and emission of gamma rays by nuclei. This phenomenon was first observed by Rudolf Mössbauer in ^{158}Ir in 1958, and led to the development of the technique which now

bears his name. Many detailed accounts of the theory and instrumentation of Mössbauer spectroscopy can be found in the literature [11-13].

In Mössbauer spectroscopy the γ-ray source consists of a solid matrix in which a radioactive isotope is embedded which then decays into the Mössbauer isotope in an excited state which subsequently relaxes with the emission of a γ-ray. For resonant absorption the energy of the γ-ray must not be influenced by nuclear recoil, to achieve this the Mössbauer nuclei are held in a rigid crystal lattice. If the energy of the nuclear recoil associated with the absorption and emission of γ-rays is small in comparison to the lowest quantised lattice vibration, recoil free transitions suitable for a Mössbauer experiment can occur. In the case of ^{57}Fe the γ-ray energy is small (14.4keV), and thus recoil effects are small.

The energy of the transition between the excited and ground state of the Mössbauer nucleus is usually different in the source and absorber. Therefore, rarely does the energy of the incident γ-ray correspond to the energy transition of the absorber Mössbauer atom. The γ-ray energy is subsequently modified by the Doppler effect, achieved by vibration of the source at a velocity of millimetres per second. Thus, a Mössbauer spectrum consists of a plot of γ-ray counts against γ-ray energy, Figure 2-19. The γ-ray energy is presented in terms of the velocity of the source. A typical Mössbauer spectrum obtained from a sample in which the Mössbauer atoms are in the same cubic environment in both source and absorber is presented in Figure 2-19.

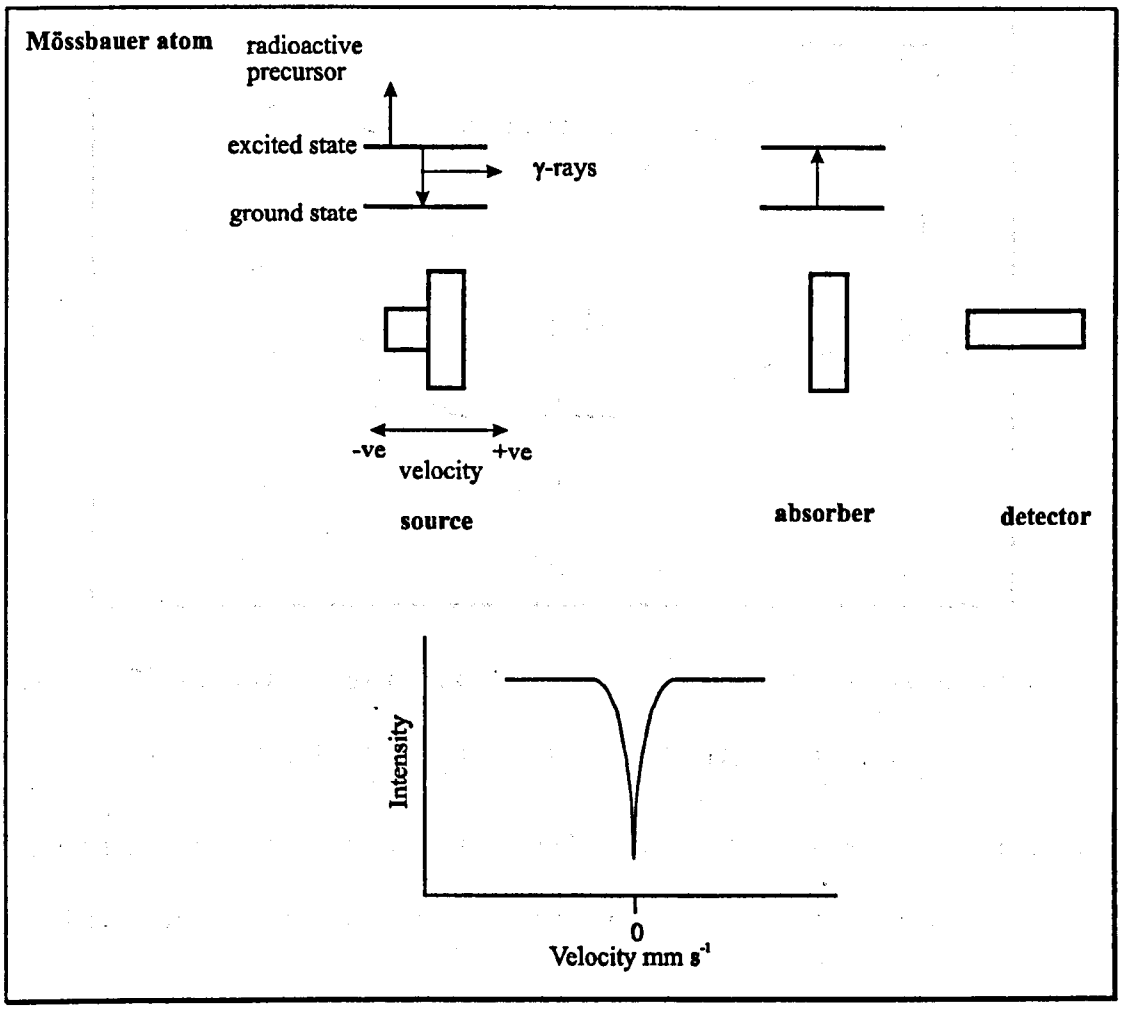

Figure 2-19 Schematic representation of a Mössbauer spectroscopic experiment.

Differing environments about the nucleus in the absorber atom give rise to hyperfine interactions which are described as the Mössbauer parameters known as isomer shift, quadrupole splitting and magnetic hyperfine splitting. These arise because of the electric monopole interaction, electric quadrupole interaction and magnetic monopole interaction respectively.

2.3.2 Isomer Shift

To understand the origin of the isomer shift it is useful to consider a nucleus stripped of its electrons. In such a nucleus the energy of the transition between ground and excited states may be represented as E, in the Figure 2-20(a).

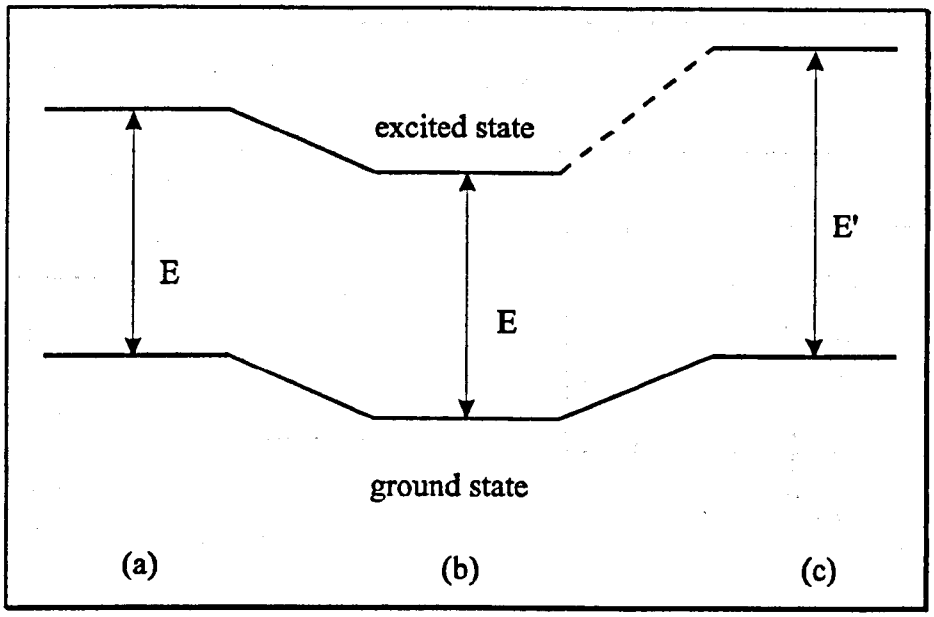

Figure 2-20 Nuclear energy level of (a) bare nucleus, and a nucleus where the excited and ground states are (b) the same size and (c) differing sizes.

If the nucleus is surrounded by electrons a Coulombic attraction between the nuclear and the electronic charges occurs which modifies the nuclear energy levels. If in both the excited and ground states the size of the nucleus is the same, then the interaction of these states with the electrons will be the same. Hence the energy levels will be changed by the same amount, as will the energy of the transition E, in Figure 2-20(b). If, alternately, the size of the nucleus of the two states are different, as usually arises, the energies of the ground and excited states will be modified to a different extent, consequently the energy of the transition will be modified to a new value E', Figure 2-20(c).

The nuclear energy levels depend upon the electronic environment. Therefore if the source and absorber nuclei are in different electronic environments then the nuclear energy levels will be modified to differing degrees, Figure 2-21(a). So the energy of the emitted γ-ray is modified by the Doppler effect and the Mössbauer spectrum will

exhibit a resonant absorption shifted from zero velocity, Figure 2-21(b). This is known as the isomer or chemical isomer shift, δ.

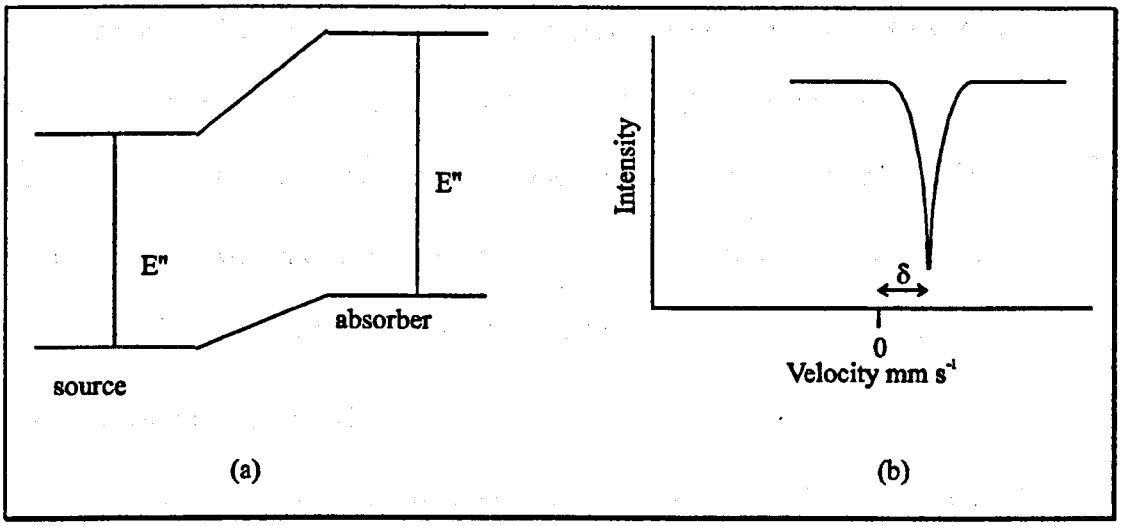

Figure 2-21 (a) Nuclear energy levels of source and absorber atoms in different electronic environments, (b) the resultant spectrum.

The isomer shift can be related to the electronic properties by the equation

$$\delta = \text{constant}\frac{\Delta R}{R}(\Psi_o^2(o)_A - \Psi_s^2(s)_S) \qquad (2.20)$$

where $\Delta R/R$ is $(R_e - R_g)/R_g$ and R_e and R_g are the radii of the excited and ground state nuclei respectively. $\Psi_s^2(o)_A$ and $\Psi_s^2(o)_S$ are the s-electron densities at the absorber and source respectively. $\Psi_s^2(o)$ is dependent primarily on the population of the s-orbitals, but will also be influenced by the occupation of other types of orbitals. This is due to the outer electrons shielding the interaction of the s-electrons from the nucleus. For any particular source the value of $\Psi_s^2(o)_S$ will be constant, and therefore any change in the isomer shift will reflect changes in $\Psi_s^2(o)_A$. Hence information about the electronic environment of the absorber is obtained, which can then be used as a probe of oxidation state.

For ^{57}Fe Mössbauer spectroscopy the value of $\Delta R/R$ is negative. Hence higher s-electron densities at iron nuclei are reflected by a decrease in isomer shift. Another influence on the isomer shift in iron compounds is the effect of shielding. As d electron removal effectively increases the s-electron density at the iron nuclei, iron(II) species with a d^6 configuration have a more positive isomer shift than iron(III) species with a d^5 configuration. In ^{57}Fe nuclei the magnitude of $\Delta R/R$ is sufficiently large for a range of isomer shifts to exist.

2.3.3 Quadrupole Splitting

If a nucleus has a spin I greater than 1/2 then it will have an asymmetric charge distribution, which gives rise to a nuclear quadrupole moment. It is then possible for the nuclear quadrupole moment to interact with an asymmetric electric field represented by an electric field gradient. This results in the partial or complete splitting of the nuclear energy levels. As more than one nuclear transition may occur, a multi-line Mössbauer spectrum results. For nuclear transitions the selection rule is $\Delta m = 0, \pm 1$. ^{57}Fe has excited and ground state spins of 3/2 and 1/2 respectively, which for this isotope means that the presence of an electric field gradient gives rise to a two line spectrum, shown in Figure 2-22. The distance between the peaks is the quadrupole splitting, Δ.

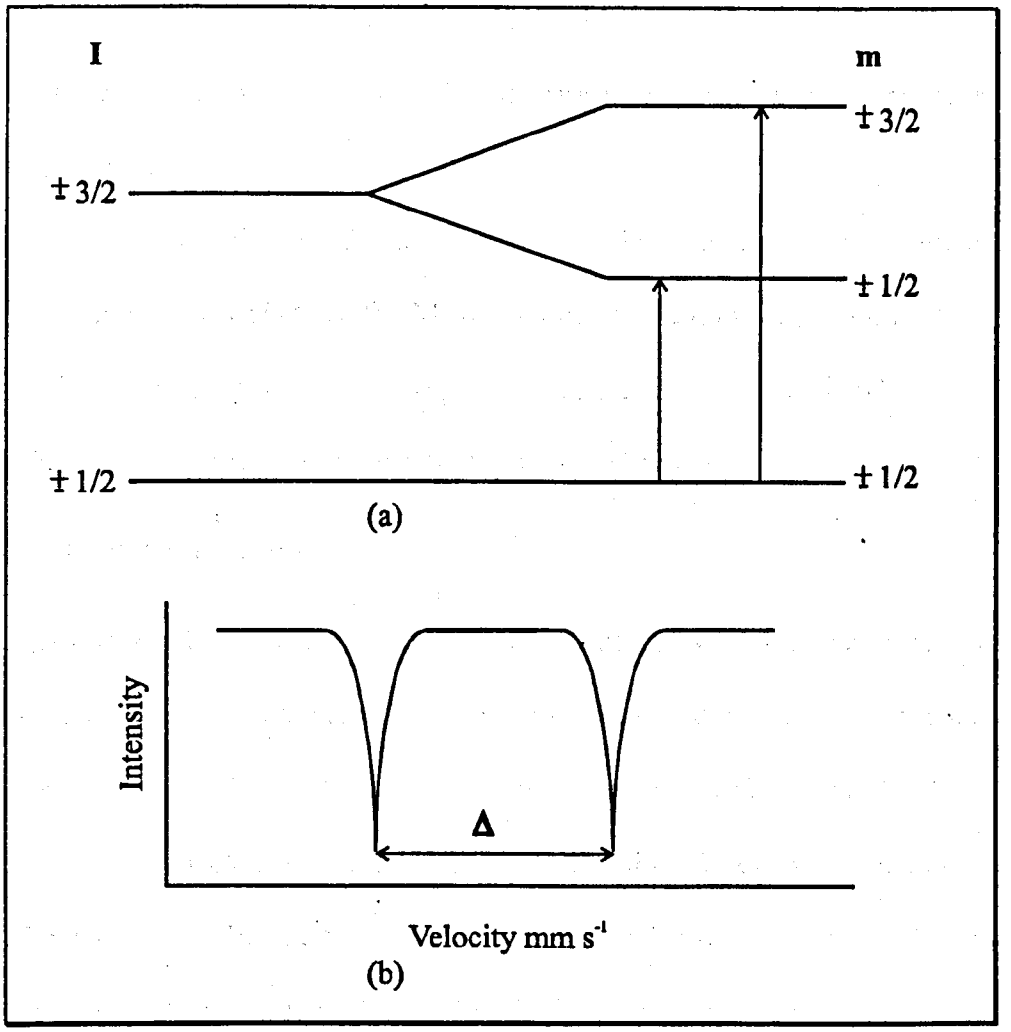

Figure 2-22 (a) Splitting of nuclear energy levels for ^{57}Fe nuclei in the presence of an electric field gradient and (b) resultant spectrum.

Several different components contribute to the electric field gradient. One is from the electronic environment about the nucleus, called the valence term. The valence term can be envisaged as arising from the valence electrons of the Mössbauer atom and originates from asymmetry in the electronic structure which derives from the unfilled or partially filled electron shells occupied by the valence electrons. The main contribution to the valence term is the asymmetric p- and d- electron populations, as the s-electron density is principally symmetric about the nuclear volume. A lattice contribution, arising from surrounding charged entities, also contributes to the electric field gradient. This arises from asymmetry in the arrangement of atoms

around the Mössbauer nuclei. Further contributions to the electric field gradient include the effects of molecular orbitals and any polarisation of the core electrons of the Mössbauer atom.

Hence, quadrupole splitting reflects the symmetry of the bonding environment and local structure in the vicinity of the Mössbauer atom. Used in conjunction with chemical isomer shift data, the quadrupole splitting can be used to elucidate the oxidation states, electronic configurations and ligand arrays.

2.3.4 Magnetic Splitting

A nucleus of spin $I > 0$ has a magnetic moment which may interact with a magnetic field via a magnetic dipole interaction. Such a magnetic interaction induces splitting of the nuclear energy levels. Degeneracy of the nuclear states is removed by interaction of the nucleus with the magnetic field, and the levels subsequently split into $2I + 1$ substates. In ^{57}Fe the ground state with $I = 1/2$ splits into two substates, and the excited state with $I = 3/2$ splits into four substates. For these spin states the selection rules $\Delta m = 0, \pm 1$, give rise to a symmetric six line Mössbauer spectrum. In such a spectrum the isomer shift is given as the centre of gravity of the six peaks. The magnetic splitting of the ground and excited states for ^{57}Fe and resultant spectrum is illustrated in Figure 2-23.

The total magnetic field experienced by the nucleus is a vector sum of the magnetic hyperfine field and any external applied field. The magnetic hyperfine field arises from the spin of any unpaired electrons and is dependent upon oxidation and spin state of that atom. Hence, interpretation of the magnetically split Mössbauer spectrum can give information about electronic structure and magnetic properties in a system. It is also possible to modify the hyperfine field by application of an external factor, which distinguishes the hyperfine field from the other Mössbauer hyperfine

interactions. Altering the applied field can change the appearance of the spectrum and aid interpretation. The occurrence of magnetically split ^{57}Fe Mössbauer spectra is common among ferro- and antiferro- magnetic materials. Paramagnetic materials cooled to below their Curie temperatures also exhibit a magnetically split Mössbauer spectrum.

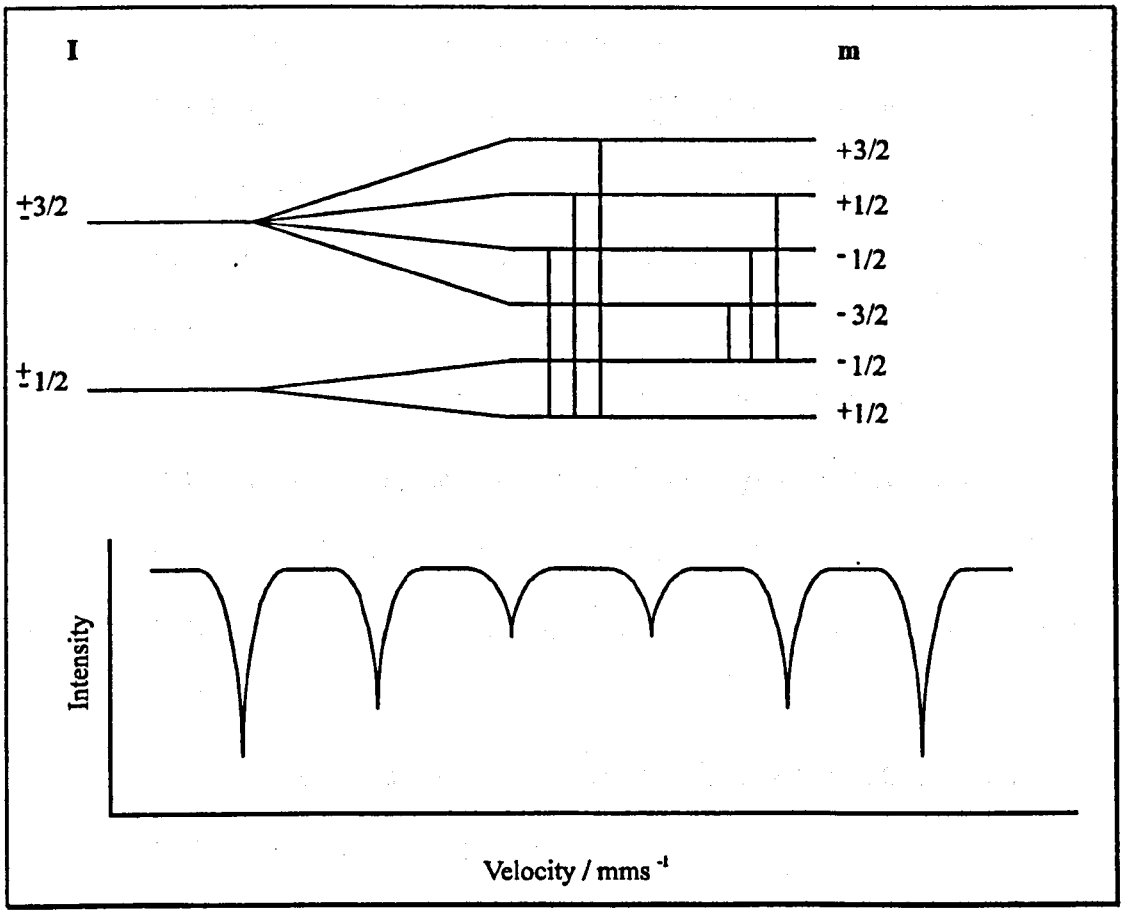

Figure 2-23 - (a) Splitting of nuclear energy levels by a magnetic field (b) and resultant spectrum.

2.4 References.

1. A.R West, *Solid Chemistry and Its Applications*, John Wiley & Sons, Chichester, 1992.

2. C Kittel, *Introduction to Solid State Physics*, John Wiley & Sons, New York, 7th Ed 1996.

3. M.J Buerger, *X-ray Crystallography*, John Wiley & Sons, New York, 1942.

4. W.L Bragg, *Proc. Cambridge Phil Soc*, 1913, **17**, 43.

5. A Boultif and D Louer, *J. Appl. Crystallogr.*, 1991, **24**, 987.

6. P Scherrer, *Göttinger Nachtricthen*, 1918, **2**, 98.

7. H.P Klug and L.E Alexander, *X-ray Diffraction Procedures for Polycrystalline and Amorphous Materials*, Wiley, 1974.

8. B.K Teo, *EXAFS: Basic Principles & Data Analysis*, Springer-Verlag, Berlin, 1986.

9. B.K Teo and P.A Lee, *J. Am. Chem. Soc.*, 1979, **101**, 2815.

10. "CCLRC Daresbury Laboratory EXCURV92 program" N Binsted, J.W Campbell, S.J Gurman, and P.C Stephenson 1991

11. N.N Greenwood and T.C Gibb, *Mössbauer Spectroscopy*, Chapman and Hall, London, 1971.

12. D.P.E Dickson and F.J Berry, *Mössbauer Spectroscopy*, Cambridge University Press, Great Britain, 1986.

13. R.V Parish, *NMR, NQR, EPR and Mössbauer Spectroscopy*, Ellis Horwood, London, 1990.

CHAPTER 3 - EXPERIMENTAL

3.1 The Silver Amalgamation Process.

The general synthesis procedure was as follows:

Ground powders of Ag_2S (Alfa, 99.5%), $CuCl_2.2H_2O$ (Aldrich, 99%), NaCl (Aldrich, 99%) were added to 35 ml of H_2O and stirred. Where Hg (Aldrich 99.9%) was added the addition was after 24 hours. After 96 hours the mixture was filtered and both phases were evaporated to dryness. Experimental amounts are given in Table 4.1 and conditions under which experiments were performed are described in Chapter 4.

3.2 Rare Earth doped Strontium Hexaferrite.

3.2.1 Calcination of oxides.

Mixtures of $SrCO_3$ (Alfa, 99.99%), Fe_2O_3 (99.5%, Alfa), Eu_2O_3 (99.99%, Aldrich), La_2O_3 (99.95%, Aldrich), mass amounts shown in Table 3.1, enough to make 0.05M of product, were ground and calcined at 1250°C, at a heating rate of 5K min^{-1}, until the mixture was phase pure as determined by X-ray powder diffraction.

System	$SrCO_3$ (g)	Fe_2O_3 (g)	Eu_2O_3 (g)	La_2O_3 (g)
$SrFe_{12}O_{19}$	0.74	4.79		
$Sr_{0.95}Eu_{0.05}Fe_{12}O_{19}$	0.70	4.79	0.04	
$Sr_{0.90}Eu_{0.10}Fe_{12}O_{19}$	0.66	4.79	0.09	
$Sr_{0.95}La_{0.05}Fe_{12}O_{19}$	0.70	4.79		0.04
$Sr_{0.90}La_{0.10}Fe_{12}O_{19}$	0.66	4.79		0.08

Table 3 -1- Masses used in the calcination synthesis of doped $SrFe_{12}O_{19}$.

3.2.2 Co-precipitation of Gels.

Mixtures of $SrCl_2.6H_2O$ (Aldrich , 99.5%), $FeCl_3.6H_2O$ (Aldrich , 99%), $EuCl_3.6H_2O$ (Aldrich, 99.99%), $LaCl_3.7H_2O$ (Aldrich , 99%), were dissolved in 50 ml of H_2O ,amounts outlined in Table 3.2, and added to a 50ml aqueous solution of 25g NaOH (BDH, 99%), and 6.25g Na_2CO_3 (Aldrich , 99%). After formation of the gel , the mixture was stirred for 30 min, and the mixture allowed to stand for 30 minutes prior to filtration. Washing of the residue was carried out to remove Cl^- ions which impede the formation of the product. The absence of Cl^- ions in the residue was determined by addition of the washings to a solution of $AgNO_3$. When no AgCl was precipitated the residue was free of chloride ion contamination. The solid was then dried and calcined at 925°C, at a heating rate of 5K min^{-1}, for 2 hours.

System	$SrCl_2.6H_2O$ (g)	$FeCl_3.6H_2O$ (g)	$EuCl_3.6H_2O$ (g)	$LaCl_3.7H_2O$ (g)
$SrFe_{12}O_{19}$	1.87	20.28		
$Sr_{0.95}Eu_{0.05}Fe_{12}O_{19}$	1.77	20.28	0.13	
$Sr_{0.90}Eu_{0.10}Fe_{12}O_{19}$	1.68	20.28	0.26	
$Sr_{0.95}La_{0.05}Fe_{12}O_{19}$	1.77	20.28		0.13
$Sr_{0.90}La_{0.10}Fe_{12}O_{19}$	1.68	20.28		0.26

Table 3 -2- Masses used in the co-precipitation synthesis of doped $SrFe_{12}O_{19}$.

3.2.3 Hydrothermal Synthesis.

Mixtures of $Sr(NO_3)_2$ (Aldrich, 98%), $Fe(NO_3)_3.9H_2O$ (Aldrich , 99.5%), $Eu(NO_3).5H_2O$ (Aldrich , 99.9%), $La(NO_3)_3.6H_2O$ (Aldrich , 99.5%) were added to NaOH , such that the ratio of NO_3^- : OH^- was 1:2, mass amounts are given in Table 3.3. The ratio of Sr (Eu/La): Fe was 1:8, as previously discussed in the literature [1]. The mixture was then stirred for 30 minutes, and placed in a Teflon lined autoclave. The sample was heated under autogenous pressure, a pressure of 25bar, at 220°C for 2 hours. After cooling the mixture was washed with water and dried.

System	$Sr(NO_3)_2$ (g)	$Fe(NO_3)_3.9H_2O$ (g)	$Eu(NO_3).5H_2O$ (g)	$La(NO_3)_3.H_2O$ (g)	NaOH (g)
$SrFe_{12}O_{19}$	1.59	24.24			15.6
$Sr_{0.95}Eu_{0.05}Fe_{12}O_{19}$	1.51	24.24	0.16		15.63
$Sr_{0.90}Eu_{0.10}Fe_{12}O_{19}$	1.43	24.24	0.32		15.66
$Sr_{0.95}La_{0.05}Fe_{12}O_{19}$	1.51	24.24		0.16	15.63
$Sr_{0.90}La_{0.10}Fe_{12}O_{19}$	1.43	24.24		0.32	15.66

Table 3 -3- Masses used in the hydrothermal synthesis of doped $SrFe_{12}O_{19}$.

Due to the low level of dopant used it proved impossible to get accurate levels of dopant in the formed product.

3.3 X-Ray Powder Diffraction.

X-ray diffraction patterns were recorded using a Siemens Kristalloflex D5000 using Cu K_α (1.5406Å) radiation, with a Ni filter. Two types of scan were recorded, a short 1 hour scan for phase identification, and a longer 14 hour scan for unit cell parameter determination.

Unit cell parameter determination was carried out using in-situ Si corrected X-ray powder diffraction patterns. The fitting of the sample was performed using DICVOL91[2] and a standard least squares routine supplied by Siemens.

3.4 X-Ray Absorption Fine Structure.

XAFS measurements were performed on the Fe K-edge, and the La L_{III}-edge in transmission geometry using Station 7.1 at the SRS at the Daresbury Laboratory with the storage beam in multibunch mode. XAFS measurements were carried out on the Sr K-edge on station 9.2, using fluorescence geometry, again at the SRS with the storage beam in multibunch mode.

Analysis of the data was performed using the Daresbury suite of software i.e. EXCALIB, EXBACK[3] and EXCURV92[4].

3.5 Mössbauer Spectroscopy.

Mössbauer spectra were recorded at various temperatures using a constant acceleration spectrometer with a ^{57}Co(Rh) source and a He-closed cycle cryogenerator[5]. The powdered sample was sandwiched between two aluminium foils to ensure good thermal conductivity between the sample and sample holder.

Temperature control was achieved within ±1.5K. The spectra were fitted to Lorentzian lines using the MFIT computer program.

3.6 X-Ray Photoelectron Spectroscopy

Powdered samples were mounted on double-sided adhesive carbon tape. XPS data were recorded using a CLAM-2 analyser under an operating vacuum of 10^{-8} Torr using Al Kα radiation (300W), with an analyser transmission energy of 100eV for the wide scan spectra and 20eV for the narrow scan spectra. All the spectra were recorded at take-off angles of 90°. All binding energy values were charge corrected to the C1s signal set at 284.6 eV. The accuracy of determination of the binding energies is 0.2eV.

3.7 Electron Microscopy

The TEM analysis was performed using a Phillips CM20 electron microscope operating at an accelerating voltage of 200kV. Images were formed under bright field imaging conditions and selected area diffraction patterns were also recorded. These measurements were carried out at the IRC in Materials for High Performance Applications at The University of Birmingham.

3.8 Magnetic Susceptibility Measurements.

A vibrating sample magnetometer was used to analyse powder samples. Powder samples were placed in a sample holder and then bonded using an adhesive wax to prevent movement of the material upon the application of a magnetic field. The system used a modified loudspeaker to vibrate the sample. The amplitude of this voltage is directly proportional to the magnetisation of the sample. The arrangement

of sample and coils was held in the pole gap of an electromagnet, driven by a high current power supply. The system was interfaced to a computer.

The powder was aligned in a field of ~2T and field cooled. The sample was measured and the data recorded. The samples were then rotated through 90° and measured again. This allowed the comparison of the induced magnetic field in the two directions. Calibration was achieved with a nickel standard.

3.9 References.

1. A Ataie, I.R Harris and C.B Ponton, British Ceramic Proceedings, W.E Lee and A Bell, University of Leeds, 20 December, 1993-22 December, 1993, Institute of Materials, London, 1994, pp. 273-281.

2. A Boultif and D Louer, *J. Appl. Crystallogr.*, 1991, **24**, 987.

3. "CCLRC Daresbury Laboratory EXCALIB and EXBACK programs"

4. "CCLRC Daresbury Laboratory EXCURV92 program" N Binsted, J.W Campbell, S.J Gurman, and P.C Stephenson 1991

5. J.R Gancedo, M Gracia and J.F Marco, *Hyperfine Interact.*, 1994, **83**, 71.

CHAPTER 4 - RESULTS AND DISCUSSION

SILVER AMALGAMATION PROCESS.

4.1 Introduction.

An in-depth introduction to this work is given in Chapter 1.

4.2 A chemical model of the extraction process.

The pure substances used in a laboratory do not reproduce the indeterminate mixtures of minerals obtained in mining and used on the patio. In this respect, the laboratory studies described here, like all previous ones, are only a chemical model of the historical operation. In place of the original ore, Ag_2S (Alfa, 99%) is used; this assumes that the bulk of the ore was found as sulphides. This is basically true, because the amalgamation process became necessary when the reduced sulphide zone was reached after the more productive ores containing native silver and silver chloride had become depleted.

The active ingredient in *'magistral'* is soluble copper(II) sulphate, and indeed, Percy reports that in some 19th century versions of the process, pure $CuSO_4.5H_2O$ was used[1]. This is effective because it forms Cu^{2+} in aqueous solution. To avoid adding a further chemical species, sulphate, to the reaction mixture, in the model process used here *magistral* is replaced by copper(II) chloride in the form of $CuCl_2.2H_2O$ (Aldrich, 99%).

Liquid mercury (Aldrich), NaCl (Aldrich, 99%), and a standard amount of distilled water (35 cm^3) were also used.

The reaction mixtures were stirred with a magnetic stirrer for 96 hours at room temperature, and the products were then analysed. Contemporary accounts are naturally weak on quantitative detail, but the descriptions given by Percy[1] suggest that the chemical elements in the initial reaction mixture were present in the approximate molar ratio Ag : Cu : Hg : Cl of 2 : 3 : 6 : 120. An extra 30% of mercury

was then added during the final stages. It follows that accurate modelling of the process requires an aqueous medium containing high concentrations of chloride ions, and most of the procedures to be described were carried out under such conditions.

4.3 Validation of Model.

The first step in the investigation was to check that the model system could achieve the degree of silver extraction that was reached in the historical amalgamation process. A complete extraction procedure was therefore undertaken, along with an analysis of the final amalgam. The relative amounts of reactant are shown in Table 4.1 (Experiment 1); the initial 70% of the mercury was added after 24 hours.

After 96 hours the final 30% of mercury was added and gently agitated in the insoluble material to draw in and consolidate as much of the amalgam phase as possible. The light non-amalgam material was then removed by decantation with flowing water. The amalgam phase that was obtained in this way was both duller and less mobile than mercury; indeed, it was almost plastic. It was dissolved in concentrated HNO_3. This converts the silver to $Ag^{+}_{(aq)}$, and the mercury to $Hg^{2+}_{(aq)}$. After the formation of NO_2 had ceased, a further addition of acid was carried out and the mixture stirred for a further 24 hours to ensure complete reaction. The silver was precipitated with dilute hydrochloric acid, and then filtered, dried and weighed as silver chloride. Figure 4-1 shows the X-ray powder diffraction pattern of the precipitate, and confirms that it is indeed AgCl. The weight of the precipitate showed that about 90% of the silver in the initial mass of silver sulphide had been extracted as amalgam. This figure is close to that claimed in contemporary historical accounts of the extraction process.[1]

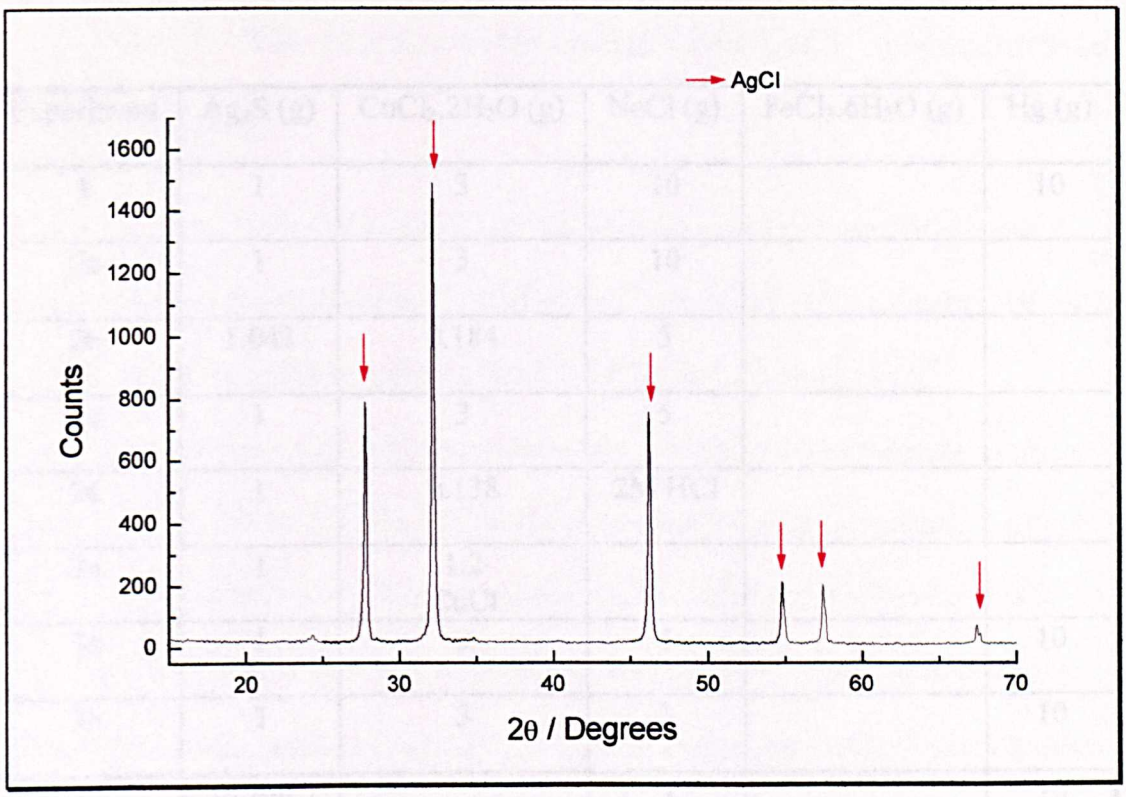

Figure 4-1 X-ray powder diffraction pattern recorded from preciptated product from validation procedure.

The above procedure confirms that the model used in these experiments is indeed valid and can be used to isolate the various stages in the formation of AgCl.

Experiment	Ag_2S (g)	$CuCl_2.2H_2O$ (g)	NaCl (g)	$FeCl_3.6H_2O$ (g)	Hg (g)
1	1	3	10		10
2a	1	3	10		
2b	1.042	0.184	5		
2c	1	3	5		
2d	1	0.138	2M HCl		
2e	1	1.2 CuCl			
3a	1	3	5		10
3b	1	3	3		10
3c	1g AgCl		5		10
4a	2		5	2.2	
4b	2		5	2.2	10
5	1	0.70			

Table 4-1 Table showing masses of reagents used in this study.

The investigation to be described separates the overall process into two main stages. The first is the reaction of Ag_2S with copper (II) chloride in concentrated sodium chloride solutions. The second stage is the reaction between the products of this first stage and mercury. This differentiation has been carried out for two reasons. Firstly, it mimics the actual extraction process in that the first addition of mercury was carried out after some time, usually a day, and sometimes more. Secondly, the reviewers and workers cited in Section 1.2.3 have also broken down the overall process in this way, so the same policy allows a direct comparison with their work and conclusions.

4.4 Stage 1 – The reaction between Ag_2S and $CuCl_2$ in concentrated Cl^- solution.

The amounts of Ag_2S, $CuCl_2.2H_2O$ and NaCl whose masses are shown in Table 4.1 (experiment 2a) were stirred in 35 ml of water for 96 hours. After filtration, the solid residue was dried under an infrared lamp. After drying, it looked black.

The filtrate containing the soluble products was a bright green transparent solution. On addition of further H_2O the solution became cloudy and slowly turned to a light blue. The formation of the cloudy precipitate is consistent with the presence of silver chloride. The chloride dissolves significantly in concentrated chloride solutions by forming complexes such as $[AgCl_3]^{2-}_{(aq)}$. Thus stability constant data[2] and solubility studies[3] suggest that the solubility of silver chloride at chloride concentrations of 4 mol litre^{-1} is between 10^{-2} and 10^{-3} mol litre^{-1}. Dilution of the chloride solution then precipitates it. This silver chloride was removed by filtration, and the filtrate evaporated to dryness under an infrared lamp. The residue was pale brown in colour, but on standing for a few hours, it became bright green. This observed change in colour is characteristic of $CuCl_2.2H_2O$, whose colour when anhydrous is brown, but which becomes bright green when the water of crystallisation is reabsorbed from the atmosphere.

4.4.1 Products containing copper.

The X-ray powder diffraction patterns for both phases, insoluble phase (a), soluble phase (b), shown in Figure 4-2, reveals the existence of the following compounds:

Insoluble Phase - AgCl[4], and atacamite, $Cu_2(OH)_3Cl$ [5]

Soluble Phase - NaCl[6], and $CuCl_2.2H_2O$ [7]

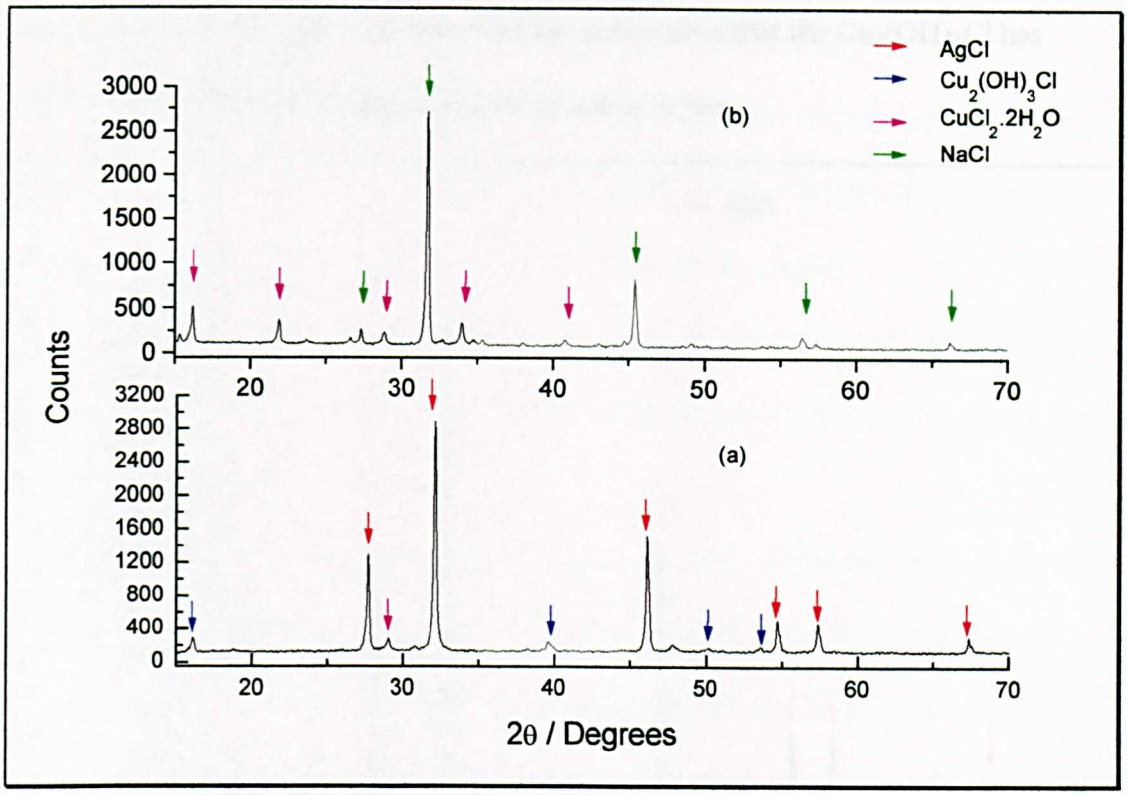

Figure 4-2 X-ray powder diffraction patterns recorded from reaction between Ag_2S and $CuCl_2$ in concentrated Cl^- solution: (a) insoluble phase, (b) soluble phase.

The soluble phase therefore contains just unused starting material, salt and AgCl dissolved as $AgCl_3^{2-}$. Previous reviews by Rickard[8] and Bakewell[9,10] have concluded that the reaction in the first stage concludes with the formation of copper sulphides. The observations above disagree with these reviews; they suggest that the major copper containing product is $Cu_2(OH)_3Cl$, and not CuS or Cu_2S. To confirm this observation the following analysis was carried out.

In dilute hydrochloric acid, both copper sulphides are insoluble,[3] but atacamite dissolves like a typical transition metal hydroxide. The filtrate was therefore washed with 2M HCl for 72 hours. After this time the material was filtered and the solid removed. After drying the solid X-ray powder diffraction pattern was recorded. The

result is shown in Figure 4-3. The recorded data shows that the $Cu_2(OH)_3Cl$ has indeed been removed, leaving AgCl as the sole product.

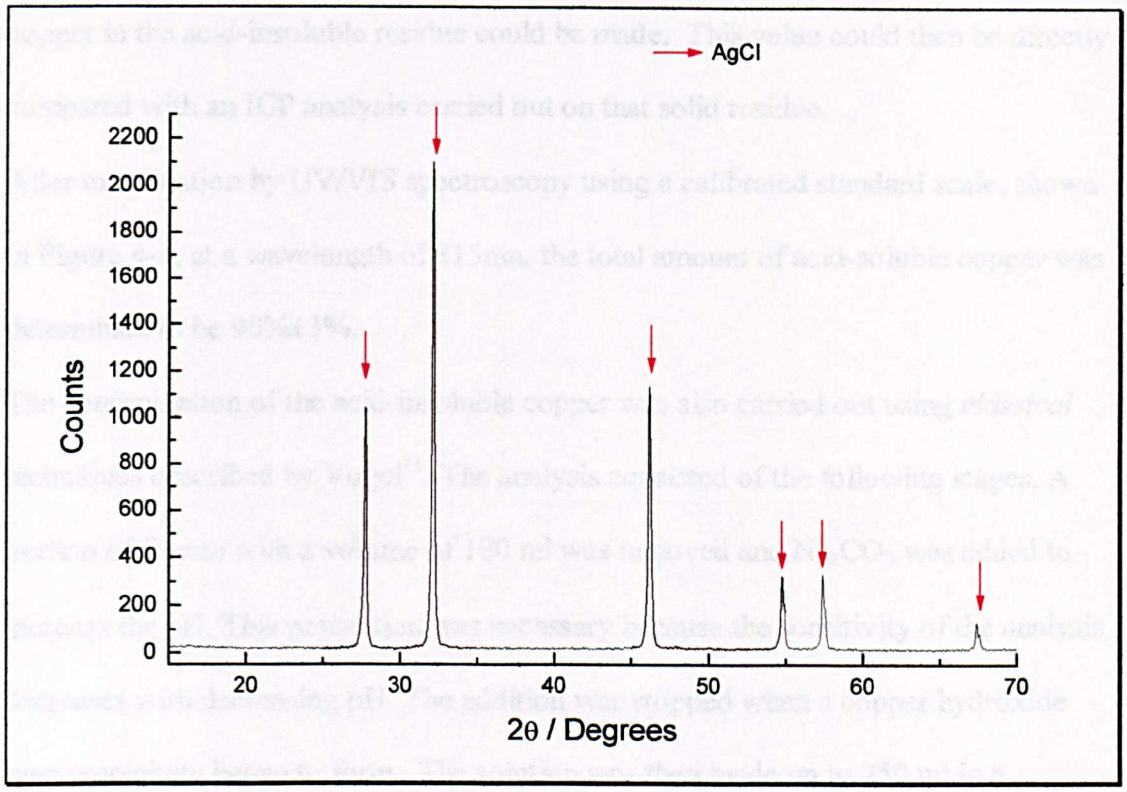

Figure 4-3 X-ray powder diffraction pattern recorded from solid product washed in HCl.

Part of the solid material was then added to NH_3 solution to determine if any copper remained in the product. On addition the solution slowly turned blue-violet in colour, indicative of the formation of tetrammine copper(II) complexes. However, as no copper compounds were detected by X-ray powder diffraction, the amount of copper still remaining in the solid was assumed to be low. To confirm this observation the following analyses were performed.

A new batch of material was prepared using identical conditions to the reaction carried out above. After filtration of the solid, the insoluble material was immediately washed with 2M HCl for 72 hours and filtered. Both sets of filtrate were then combined and analysed by both classical techniques and UV/VIS spectroscopy

to determine the amount of copper in the liquid phase. By subtracting this acid-soluble copper from the total copper in the starting material, an estimate of the copper in the acid-insoluble residue could be made. This value could then be directly compared with an ICP analysis carried out on that solid residue.

After examination by UV/VIS spectroscopy using a calibrated standard scale, shown in Figure 4-4, at a wavelength of 815nm, the total amount of acid-soluble copper was determined to be 90%±3%.

The determination of the acid-insoluble copper was also carried out using *classical* techniques described by Vogel[11]. The analysis consisted of the following stages. A portion of filtrate with a volume of 100 ml was removed and Na_2CO_3 was added to increase the pH. This precaution was necessary because the sensitivity of the analysis decreases with decreasing pH. The addition was stopped when a copper hydroxide type precipitate began to form. The solution was then made up to 250 ml in a volumetric flask. 50 ml portions of this solution were removed, and to each of these portions 3g of potassium iodate was added and well mixed. These portions , which contained liberated iodine, were then titrated against a standard solution of sodium thiosulphate. Using the amounts of titrated thiosulphate it is possible to deduce the amount of copper present in the original filtrate.

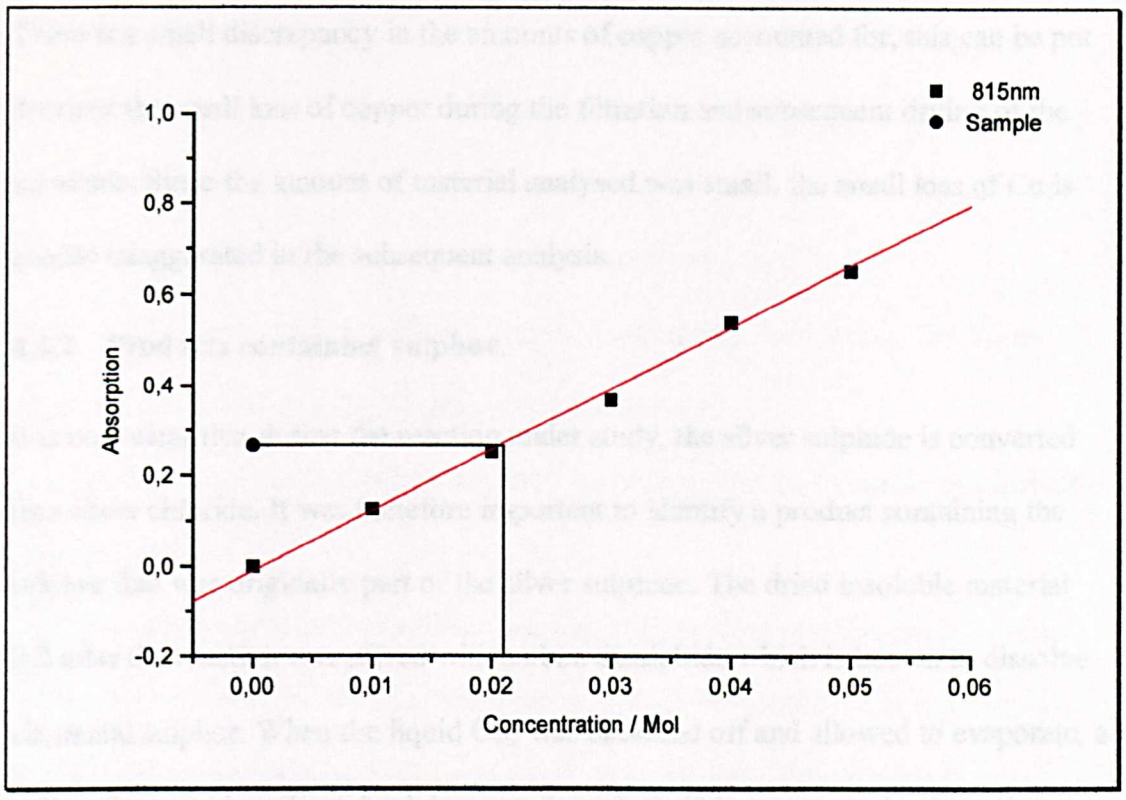

Figure 4-4 UV/VIS calibration scale and sample position.

From the above analysis a value of 87±3% of copper was present either as aqueous Cu^{2+} in the filtrate, or as insoluble $Cu_2(OH)_3Cl$ in the solid. This value agrees with that obtained by analysis of the filtrate by UV/VIS , and suggests that after the reaction, most of the copper is found as either $Cu^{2+}_{(aq)}$ or $Cu_2(OH)_3Cl_{(s)}$. Other copper species may be formed, notably in the acid-insoluble residue, but they are not major products, and under the conditions prevailing in Experiment 2a, are not detected in the X-ray powder diffraction patterns.

ICP analysis of the acid-insoluble residue, recovered from the above analytical solutions, showed that it contained ~ 3 ± 1% of the original total copper used in the experiment. Due to the lack of a reliable initial estimate of the composition, the subsequent results obtained have a larger than normal error margin. The results obtained from this method do however, agree well with the results obtained from the other methods used.

There is a small discrepancy in the amounts of copper accounted for, this can be put down to the small loss of copper during the filtration and subsequent drying of the materials. Since the amount of material analysed was small, the small loss of Cu is greatly exaggerated in the subsequent analysis.

4.4.2 Products containing sulphur.

It is now clear that during the reaction under study, the silver sulphide is converted into silver chloride. It was therefore important to identify a product containing the sulphur that was originally part of the silver sulphide. The dried insoluble material left after the reaction was stirred with carbon disulphide which is known to dissolve elemental sulphur. When the liquid CS_2 was decanted off and allowed to evaporate, a pale-yellow residue of solid sulphur was deposited. This appears to be the major sulphur product in the insoluble residue. No significant amounts of sulphur were detected in the filtrate. Thus when the filtrate from the reaction was tested with acidified barium chloride solution, only a very slight turbidity was observed, and no sulphur dioxide was smelt. This suggests that any oxidation to oxyanions of sulphur is very small. It appears, therefore, that the sulphide in Ag_2S has been mainly oxidised to the elemental state. The next step is the identification of the oxidising agent that does this.

4.4.3 The oxidising agent.

The obvious candidate for the oxidising role is copper(II). To confirm this hypothesis the following analysis was designed. A reaction was carried out with the masses shown in Table 4.1 (Experiment 2b) using degassed water as the solvent. The reaction was performed in a sealed flask under argon. This isolates the system from the atmosphere, and especially from atmospheric oxygen.

The reaction was allowed to proceed for 24 hours, after which the stirring was stopped and the mixture allowed to settle for 4 hours. The solution which had been blue-green at the start of the reaction was now colourless. The following chemical tests were then carried out on the colourless supernatant liquid.

A portion of the liquid was added to excess, aerated deionised water. The liquid became cloudy and deposited a pale-green precipitate.

A second portion of solution was added to bromine water; the bromine was instantly decolourized.

A third portion was added to a dilute solution of potassium permanganate in water. At the prevailing pH which is nearly neutral, the permanganate is not a strong enough oxidising agent to oxidise chloride[12]. Nevertheless, it was instantly decolourized.

Finally the remaining solution was left exposed to the atmosphere for 48 hours. After this time the solution had become cloudy with a pale-green precipitate.

These observations suggest that the solution formed during the reaction contains a reducing agent, and its colourless nature supports the presence of copper(I). This is consistent with the formation of a pale green precipitate on standing in air, or on addition of aerated water. The precipitate is the basic oxychloride of copper(II), atacamite, that is formed when neutral solutions of copper(I) undergo aerial oxidation in a chloride medium. Copper(I) chloride, CuCl, is very sparingly soluble in water, but it dissolves easily in strong solutions of chloride. For example, in 4M chloride solution, the solubility of CuCl is about 0.74 mol litre^{-1}, and the major species present is the trichlorocuprate(I) complex, $[CuCl_3]^{2-}_{(aq)}$, with significant but smaller amounts of $[CuCl_2]^-_{(aq)}$ [13,14]. The colourless reducing agent that is formed in the solution is therefore best written as $[CuCl_3]^{2-}_{(aq)}$.

4.4.4 The reactions of the first stage.

The above results allow a reaction scheme for stage 1 to be put forward.

(i) Copper (II) in the form of the aqueous ion, $Cu^{2+}_{(aq)}$, oxidises Ag_2S to elemental sulphur and form AgCl, while being reduced to copper(I):

$$2Cu^{2+}_{(aq)} + Ag_2S_{(s)} + 8Cl^-_{(aq)} \rightarrow 2AgCl_{(s)} + 2[CuCl_3]^{2-}_{(aq)} + S_{(s)} \qquad (4.1)$$

(ii) Atmospheric oxygen then oxidises copper (I) back to copper (II), and ultimately to the basic copper(II) chloride, atacamite, $Cu_2(OH)_3Cl$:

$$2CuCl_3^{2-}_{(aq)} + \tfrac{1}{2}O_{2(g)} + 2H_2O_{(l)} \rightarrow Cu_2(OH)_3Cl_{(s)} + 5Cl^-_{(aq)} + H^+_{(aq)} \qquad (4.2)$$

4.4.5 The pH of the solution.

In the preceding section, stress was laid upon the fact that atacamite is the ultimate copper product. The reason for this emphasis is that in the initial mixture of reactants, all the species needed to form atacamite ($Cu^{2+}_{(aq)}$, $Cl^-_{(aq)}$ and water) are present, but formation does not occur because the solution is too acid. Its pH is, in fact, about 3.5. Thus when the first traces of copper (I) are formed by the reaction between copper (II) and Ag_2S, and then oxidised back to copper (II) by atmospheric oxygen, the product is likely to be $Cu^{2+}_{(aq)}$, rather than atacamite.

When atmospheric oxygen performs a reaction of this kind, the effect is to raise the pH. Thus in acid solutions, the oxygen electrode is written:

$$O_{2(g)} + 4H^+_{(aq)} + 4e = 2H_2O_{(l)} \qquad E^\circ = 1.23\ V$$

This reveals the change in the pH as a decrease in the hydrogen ion concentration. What it suggests is that when the reaction between $Cu^{2+}_{(aq)}$ and Ag_2S begins in an oxygen atmosphere, there will be an initial increase in pH. This was therefore investigated.

The reaction was carried out in 50 ml of H_2O using the amounts of reagents shown in Table 4.1 (Experiment 2c). Oxygen gas was continuously bubbled through the

solution. This achieved thorough mixing, and allowed the pH study to be completed in hours rather than days.

During the reaction, a pH probe was immersed in the solution and the pH continuously monitored. The results are shown in Table 4.2. They reveal that the pH of the solution before the O_2 was bubbled through was 3.61. Initial contact with oxygen produced the expected increase, and the pH rose to a maximum of 3.94. However, it then dropped back to a value approaching that of the starting material. The results are plotted graphically in Figure 4-5.

The observations can be explained as follows. At the beginning of the reaction, the solution is too acid to allow precipitation of atacamite, so any $[CuCl_3]^{2-}_{(aq)}$ that is formed is oxidised back to $Cu^{2+}_{(aq)}$:

$$2[CuCl_3]^{2-}_{(aq)} + 1/2O_{2(g)} + 2H^{+}_{(aq)} \rightarrow 2Cu^{2+}_{(aq)} + H_2O + 6Cl^{-}_{(aq)} \qquad (4.3)$$

This explains the initial increase in pH. But it is known that in chloride solutions containing copper (II), atacamite begins to be precipitated at a pH of about 4 [15]. When the initial increase causes this to be reached, the formation of atacamite begins, and the reaction becomes that given in equation 4.2. This is marked by a *decrease* in pH.

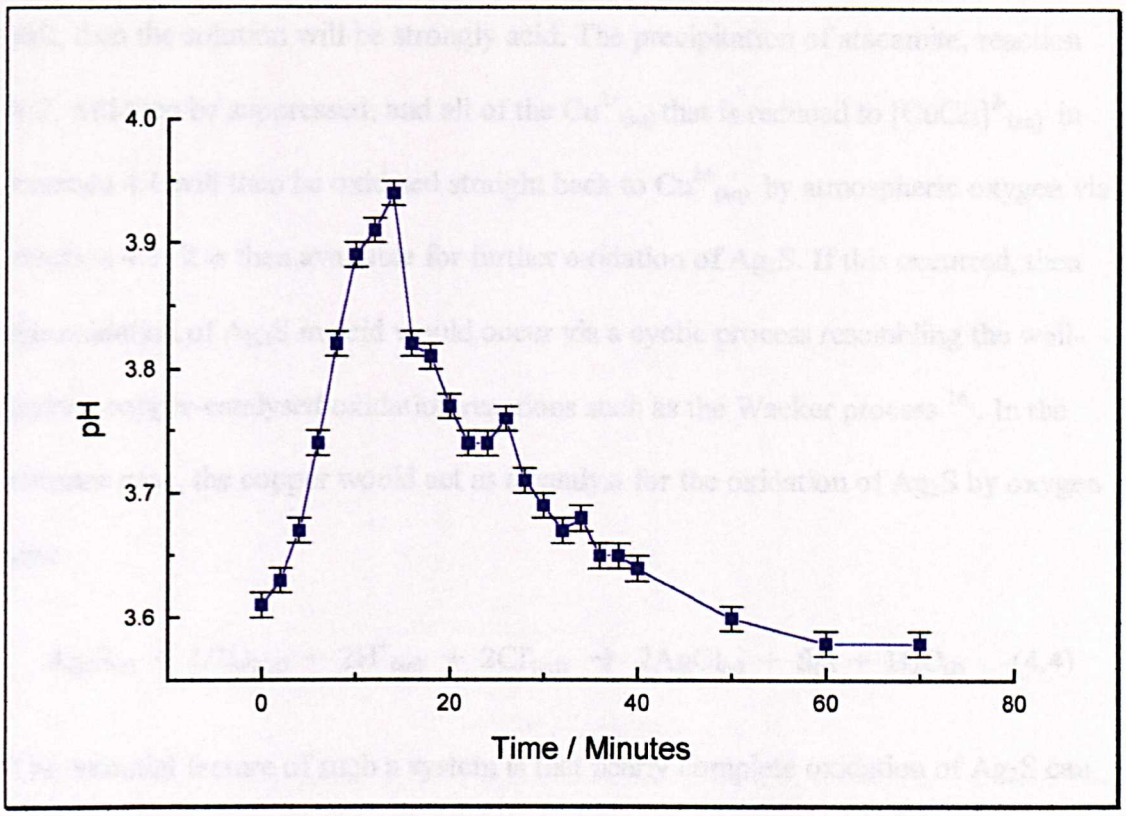

Figure 4-5 pH profile of reaction between Ag_2S and $CuCl_2.2H_2O$ in strong chloride solution.

Time (Min)	pH	Time (Min)	pH	Time (Min)	pH
0	3.61	16	3.82	32	3.67
2	3.63	18	3.81	34	3.68
4	3.67	20	3.77	36	3.65
6	3.74	22	3.74	38	3.65
8	3.82	24	3.74	40	3.64
10	3.89	26	3.76	50	3.60
12	3.91	28	3.71	60	3.58
14	3.94	30	3.69	70	3.58

Table 4-2 Table showing results from pH experiment.

4.4.6 Stage 1 under acid conditions.

The interpretation of the pH changes given in Section 4.4.5 raises an interesting possibility. If the concentrated chloride is provided by hydrochloric acid instead of

salt, then the solution will be strongly acid. The precipitation of atacamite, reaction 4.2, will then be suppressed, and all of the $Cu^{2+}_{(aq)}$ that is reduced to $[CuCl_3]^{2-}_{(aq)}$ in reaction 4.1 will then be oxidised straight back to $Cu^{2+}_{(aq)}$ by atmospheric oxygen via reaction 4.3. It is then available for further oxidation of Ag_2S. If this occurred, then the oxidation of Ag_2S in acid would occur via a cyclic process resembling the well-known copper-catalysed oxidation reactions such as the Wacker process [16]. In the extreme case, the copper would act as a catalyst for the oxidation of Ag_2S by oxygen gas:

$$Ag_2S_{(s)} + 1/2O_{2(g)} + 2H^+_{(aq)} + 2Cl^-_{(aq)} \rightarrow 2AgCl_{(s)} + S_{(s)} + H_2O_{(l)} \quad (4.4)$$

The essential feature of such a system is that nearly complete oxidation of Ag_2S can be achieved with an amount of copper well below that required by the Cu : Ag molar ratio of 1 : 1 in equation 4.1. To test this possibility, an experiment was designed in which the Cu : Ag ratio was 1 : 10. The masses are shown in Table 4-1 (experiment 2d). In this experiment the source of chloride used was 2M HCl solution, and the mixture was stirred for 96 hours. It was then filtered; the solid phase was black and the filtrate almost transparent. X-ray powder diffraction examination of the insoluble material revealed the presence of just AgCl as a major phase, shown in Figure 4-6.

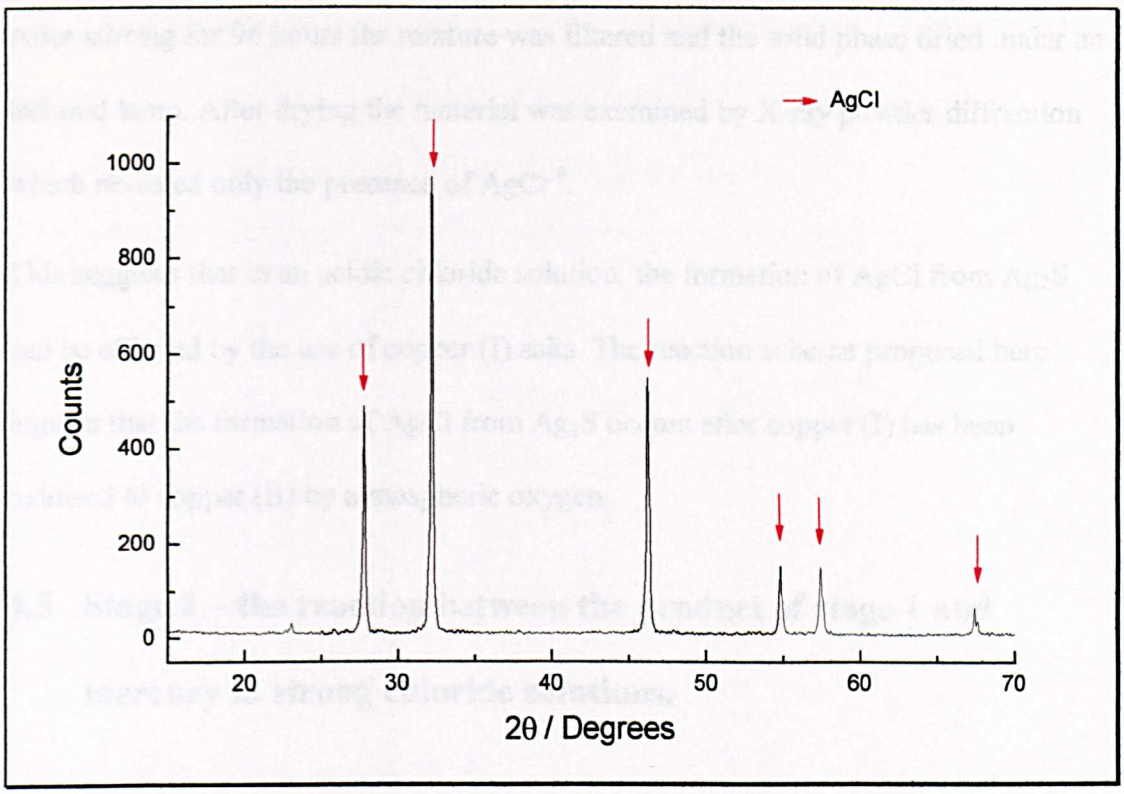

Figure 4-6 X-ray powder diffraction pattern recorded from a mixture containing Ag:Cu ratio of 5:1, Expt 2d.

X-ray powder diffraction patterns provided evidence for only a very small amount of unreacted Ag_2S, even though unreacted material was detected by this means in other experiments, and the starting material gives the expected powder pattern. The results therefore suggest that nearly complete oxidation of Ag_2S has occurred at copper levels well below that called for by equation 4.1, and that a cyclic process occurs.

Since the results outlined above suggest that copper (I) is formed and then oxidised back to $Cu^{2+}_{(aq)}$, it should be possible to use copper(I) as a starting material for the conversion of Ag_2S to AgCl. To study this, a reaction was carried out in which CuCl was used in place of $CuCl_2.2H_2O$ (Table 4.1, experiment 2e) and 2M HCl provided the strong chloride solution.

After stirring for 96 hours the mixture was filtered and the solid phase dried under an infrared lamp. After drying the material was examined by X-ray powder diffraction which revealed only the presence of AgCl [4].

This suggests that in an acidic chloride solution, the formation of AgCl from Ag_2S can be effected by the use of copper (I) salts. The reaction scheme proposed here implies that the formation of AgCl from Ag_2S occurs after copper (I) has been oxidised to copper (II) by atmospheric oxygen.

4.5 Stage 2 – the reaction between the product of stage 1 and mercury in strong chloride solutions.

To study this reaction, the amounts of reactants, shown in Table 4.1 experiment 3a, were mixed together and stirred for 24 hours. After 24 hours mercury was added, and the mixture stirred for a further 72 hours. Shortly after the addition of the mercury, the solution became dark brown in colour. Small samples of the supernatant liquid were found to decolourise potassium permanganate solution, indicating the presence of a reducing agent. The brown colour is probably caused by the formation of mixed valence complexes of copper (I) and copper (II). Mercury is known to reduce copper (II) chloride solutions, ultimately to copper(I), and these mixed valence complexes are presumably intermediates in that process. They are known to be brown in colour[17,18], and their reducing powers are a mark of the presence of copper (I).

After 72 hours the mixture was filtered and both phases dried under an infrared lamp. X-ray powder diffraction patterns, Figure 4-7, recorded from both phases showed the following constituents:

Insoluble Phase - $AgCl$[4], Ag_2Hg_3 crystalline amalgam [19], $Cu_2(OH)_3Cl$[5], and Hg_2Cl_2 calomel [20].

Soluble Phase - $CuCl_2.2H_2O$ [7], and NaCl [6]

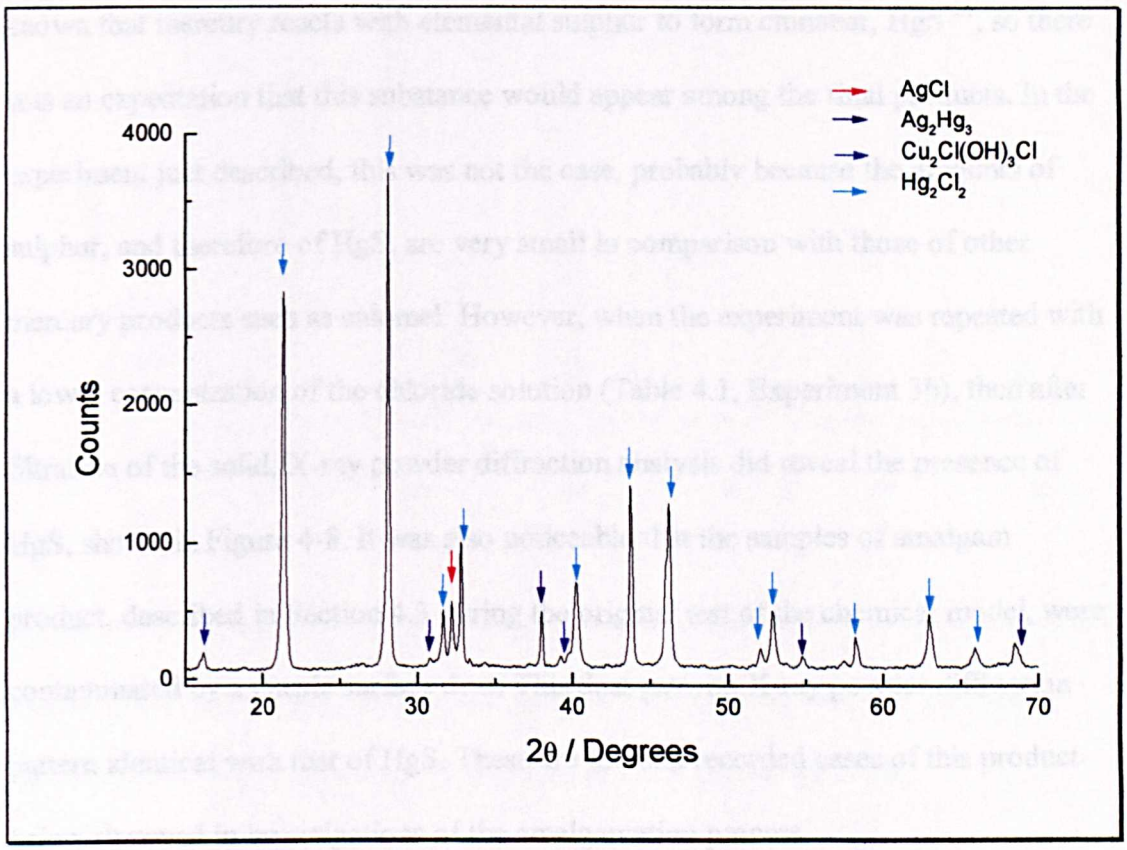

Figure 4-7 X-ray powder diffraction pattern recorded for the solid precipitate from the mixture $Ag_2S/CuCl_2/NaCl/Hg$, Expt3a

The detection of the crystalline amalgam was gratifying. It should be noted that although fresh mercury would normally be added during the final stages, no addition was made here because the amalgam would then be made liquid, and as such useless for X-ray powder diffraction.

The presence of atacamite in the product can be attributed to its formation during the generation of AgCl in stage 1, and a subsequent absence of any reaction with the mercury. The presence of calomel, Hg_2Cl_2, shows that substantial amounts of mercury are oxidised in the chloride solution. Since the X-ray diffraction

examination did not show the presence of AgCl it can be concluded that virtually all of the AgCl has been converted to amalgam.

In Section 4.4.2, elemental sulphur was detected as a product in stage 1. It is well known that mercury reacts with elemental sulphur to form cinnabar, HgS [21], so there was an expectation that this substance would appear among the final products. In the experiment just described, this was not the case, probably because the amounts of sulphur, and therefore of HgS, are very small in comparison with those of other mercury products such as calomel. However, when the experiment was repeated with a lower concentration of the chloride solution (Table 4.1, Experiment 3b), then after filtration of the solid, X-ray powder diffraction analysis did reveal the presence of HgS, shown in Figure 4-8. It was also noticeable that the samples of amalgam product, described in Section 4.3 during the original test of the chemical model, were contaminated by a purple surface dust. This dust gave an X-ray powder diffraction pattern identical with that of HgS. These are the first recorded cases of this product being observed in investigations of the amalgamation process.

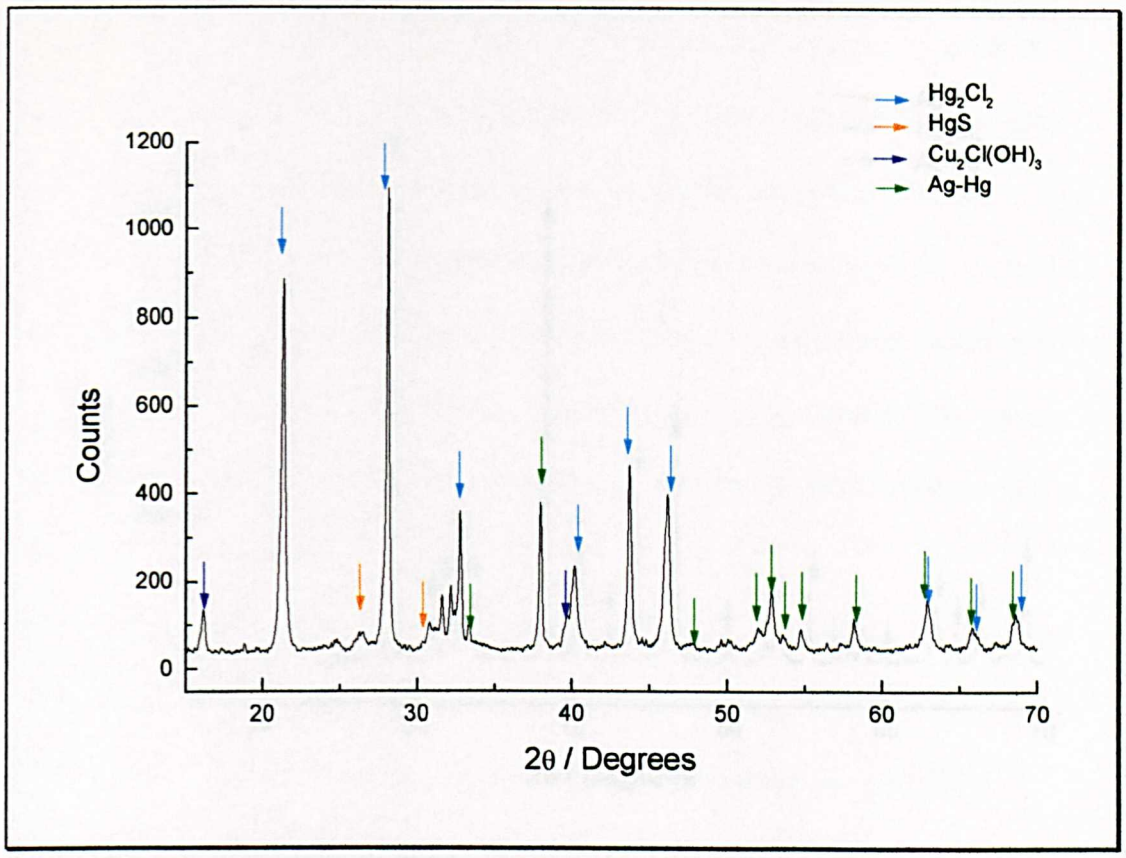

Figure 4-8 X-ray powder diffraction pattern recorded for the solid product obtained from reaction of $Ag_2S/CuCl_2/Hg$ in Cl^- solution, Expt 3b.

In order to confirm that Hg could reduce AgCl in strong chloride based solutions, a reaction was devised whereby only AgCl, Hg and NaCl were present (Table 4.1 experiment 3c). After the reaction had been allowed to proceed for 72 hours, the mixture was filtered and the solid materials examined by X-ray powder diffraction. The pattern recorded, shown in Figure 4-9, from the solid showed only the following peaks:

Insoluble Phase - Hg_2Cl_2 calomel [20], AgHg amalgam [22], and AgCl [4].

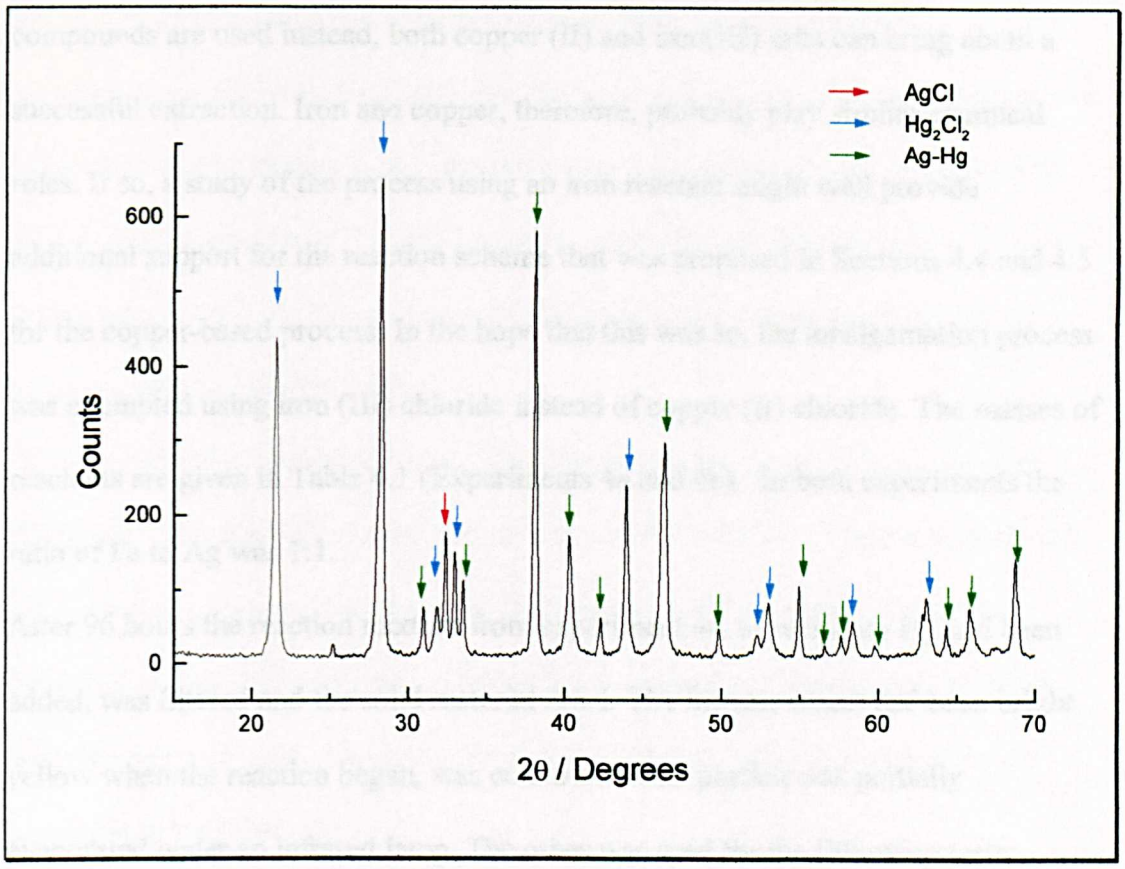

Figure 4-9 X-ray powder diffraction pattern recorded from solid product obtained from AgCl/Hg in strong Cl^- solution, Expt 3c.

The data obtained from this experiment confirms that mercury can reduce silver chloride to silver which reacts with excess mercury to form an amalgam. The mercury that acts as the reducing agent is oxidised to calomel, Hg_2Cl_2.

As can be seen in the above results, the second stage of the process is relatively straightforward: the direct reduction of the silver-containing products from stage 1 by mercury. If the amalgamated product is written Ag_2Hg_3, the reaction is:

$$5Hg_{(l)} + 2AgCl_{(s)} \rightarrow Ag_2Hg_{3(s)} + Hg_2Cl_{2(s)} \qquad (4.5)$$

4.6 The substitution of iron for copper.

It is well-known that the *magistral* ingredient employed in the amalgamation process often contained iron salts as well as those of copper, and that if pure chemical

compounds are used instead, both copper (II) and iron(III) salts can bring about a successful extraction. Iron and copper, therefore, probably play similar chemical roles. If so, a study of the process using an iron reactant might well provide additional support for the reaction scheme that was proposed in Sections 4.4 and 4.5 for the copper-based process. In the hope that this was so, the amalgamation process was attempted using iron (III) chloride instead of copper (II) chloride. The masses of reactants are given in Table 4.1 (Experiments 4a and 4b). In both experiments the ratio of Fe to Ag was 1:1.

After 96 hours the reaction mixture from experiment 4a, to which no Hg had been added, was filtered and the solid material dried. The filtrate, which had been bright yellow when the reaction began, was colourless. One portion was partially evaporated under an infrared lamp. The other was used for the following tests:

(i) A small portion of the solution was added to dilute $KMnO_4$ solution the purple solution became colourless, indicating that reduction had occurred.

(ii) A second portion was added to bromine water. The bromine was decolourized, again indicating that reduction had occurred.

(iii) A third portion was added to a solution of potassium ferricyanide: a dark blue solution formed, indicating the existence of $Fe^{2+}_{(aq)}$.

(iv) A final portion was added to ammonium thiocyanate to test for $Fe^{3+}_{(aq)}$. The test for this proved negative.

The above tests show that a reducing agent has been produced in the solution, and that this reducing agent is $Fe^{2+}_{(aq)}$. Test (iv) also shows that the reduction of $Fe^{3+}_{(aq)}$ by Ag_2S is virtually complete.

After 4 hours the solution which had been evaporating under an infrared lamp was examined using the same tests. During this lapse of time, the colour of the solution

had changed from colourless to yellow/orange, itself indicative of $Fe^{3+}_{(aq)}$. Overall the results were the same with only two differences. The first difference was that the intensity of colour change in the first three tests was slightly diminished. Secondly the thiocyanate test for Fe^{3+} proved positive, indicating the formation of Fe^{3+} during the partial evaporation. After these tests the remaining solution was evaporated to dryness under an infrared lamp.

The material left after evaporation of the filtrate was examined by X-ray powder diffraction. This analysis showed the presence of $FeCl_2.2H_2O$ [23], which agreed with the observations above. The chemical analysis above shows partial atmospheric oxidation of iron (II) had occurred during the evaporation of the reduced solution under the infrared lamp. There was no X-ray powder diffraction evidence for the formation of $FeCl_3.6H_2O$.

It should be noted here however that since Fe^{2+} precipitates out of solution at a pH of 3, and the pH was not directly measured in this reaction it may be possible that some of the Fe^{2+} in the reaction to be present in the solid residue. Since X-ray powder diffraction didn't finds any evidence of this, any formation is small.

The solid material from the reaction was also analysed by X-ray powder diffraction, Figure 4-10. The analysis showed the powder contained both Ag_2S and AgCl. After careful analysis of the pattern and comparison with a standard pattern recorded from a known mixture of Ag_2S and AgCl, it was determined that the mixture was biphasic with a concentration of 50% for each component.

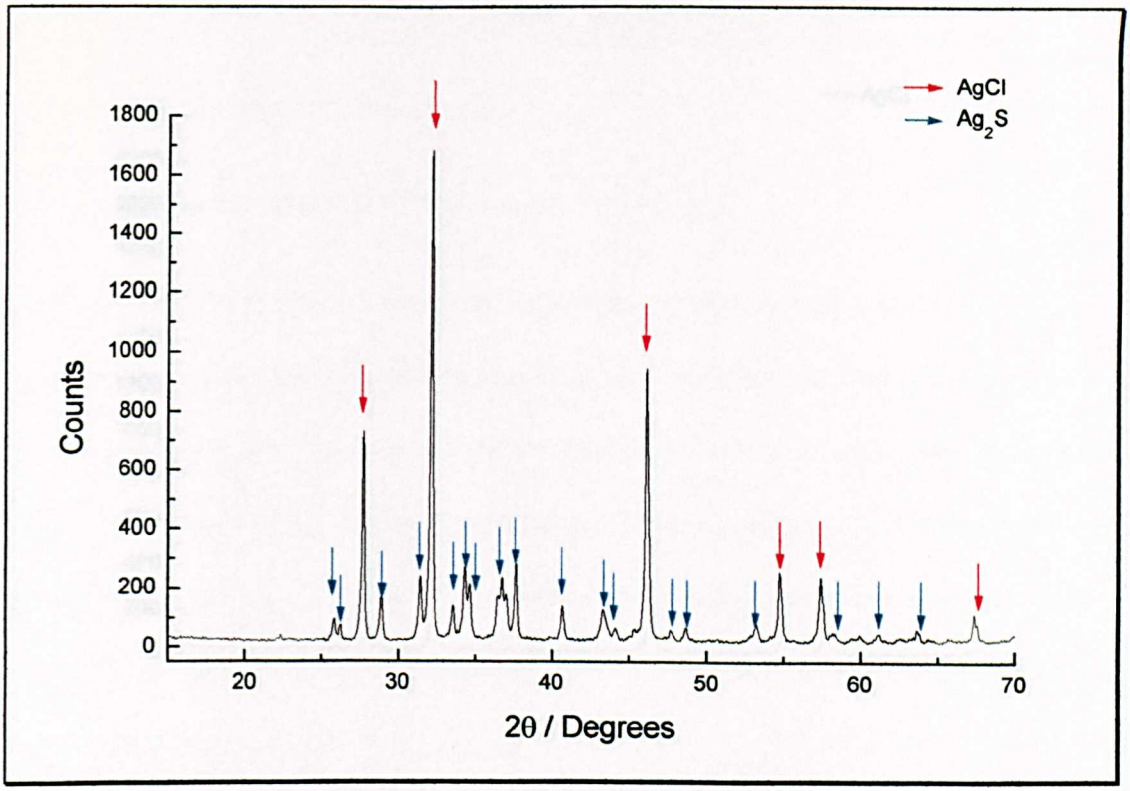

Figure 4-10 - X-ray powder diffraction pattern recorded from the solid residue when Fe is substituted for Cu in a Ag:Fe ratio of 1:1, Expt 4a.

In the original reaction mixture, the Fe : Ag molar ratio was 1 : 1. It seems that under these conditions, there is insufficient iron (III) to oxidise all of the Ag_2S. This means that all of the $Fe^{3+}_{(aq)}$ can be reduced to $Fe^{2+}_{(aq)}$. The re-oxidation back to $Fe^{3+}_{(aq)}$ by atmospheric oxygen at room temperature is slow, much slower, for example, than the corresponding oxidation of copper(I) to copper(II) in the more common copper-based process. Only when the solution is warmed and concentrated as in the evaporation experiments, does atmospheric oxidation become reasonably fast. In further experiments where the molar ratio Fe : Ag is 2 : 1 or greater, there was enough iron(III) to oxidise all of the silver sulphide, and the yield of AgCl was then found to approach 100%, shown in Figure 4-11.

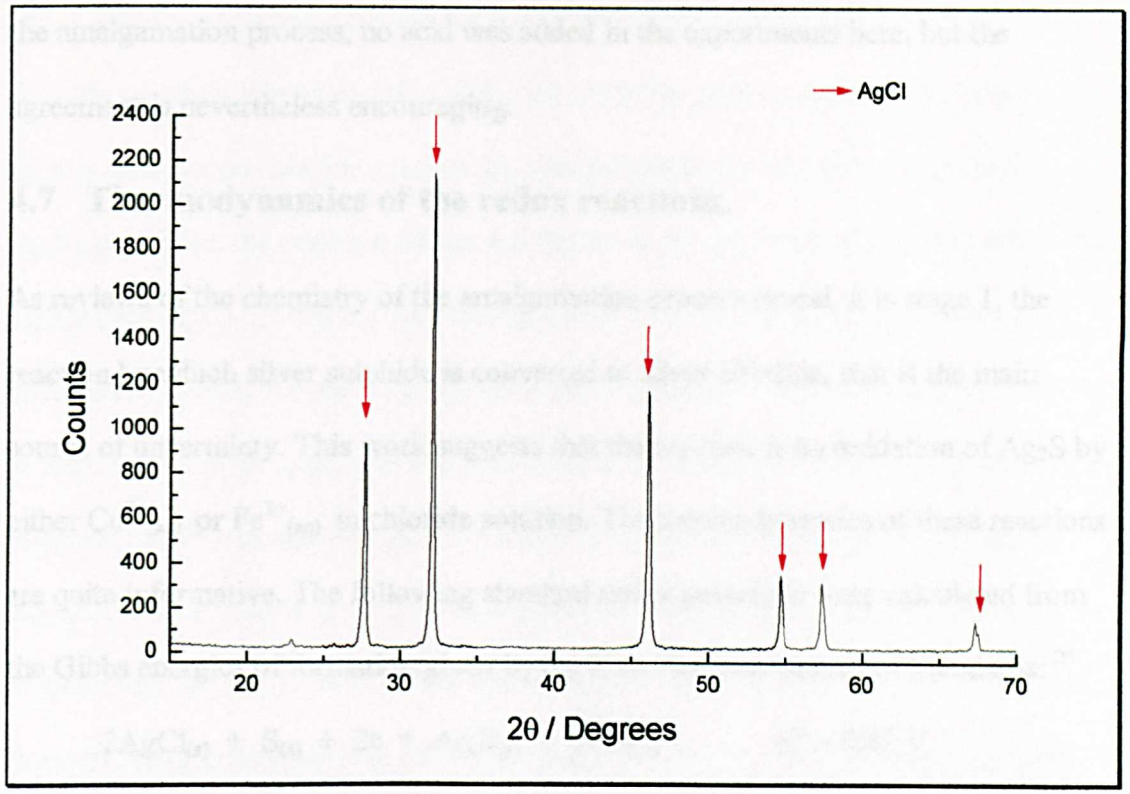

Figure 4-11 X-ray powder diffraction pattern recorded from the solid residue when Fe is substituted for Cu in a Ag:Fe ratio of 2:1.

The second experiment to be carried out using iron instead of copper was a simulation of the full amalgamation process. The analytical procedure was identical to that carried out for the copper system in Section 4.5. The yield from this analysis was again found to be ~90%. This result agrees with the earlier hypothesis that the second stage of the process only involves the reaction of mercury with the AgCl that is formed in the first stage. The first stage appears to be:

$$2Fe^{3+}_{(aq)} + Ag_2S_{(s)} + 2Cl^-_{(aq)} \rightarrow 2AgCl_{(s)} + 2Fe^{2+}_{(aq)} + S_{(s)} \qquad (4.6)$$

The analogy with the copper-based system is obvious. In both cases, the higher oxidation state of the transition metal is reduced to the lower in concentrated chloride solution. Moreover, support for the scheme of reaction 4.6 is provided by a recent study of the iron (III) chloride/ silver sulphide reaction in hydrochloric acid which came to essentially the same conclusions[24]. To be consistent with the conditions of

the amalgamation process, no acid was added in the experiments here, but the agreement is nevertheless encouraging.

4.7 Thermodynamics of the redox reactions.

As reviews of the chemistry of the amalgamation process reveal, it is stage 1, the reaction by which silver sulphide is converted to silver chloride, that is the main source of uncertainty. This work suggests that the reaction is an oxidation of Ag_2S by either $Cu^{2+}_{(aq)}$ or $Fe^{3+}_{(aq)}$ in chloride solution. The thermodynamics of these reactions are quite informative. The following standard redox potentials were calculated from the Gibbs energies of formation given by the U.S. National Bureau of Standards: [25]

$$2AgCl_{(s)} + S_{(s)} + 2e = Ag_2S_{(s)} + 2Cl^-_{(aq)} \qquad E^\circ = 0.43\ V$$

$$Cu^{2+}_{(aq)} + 3Cl^-_{(aq)} + e = [CuCl_3]^{2-}_{(aq)} \qquad E^\circ = 0.50\ V$$

$$Fe^{3+}_{(aq)} + e = Fe^{2+}_{(aq)} \qquad E^\circ = 0.77\ V$$

$$O_{2(g)} + 4H^+_{(aq)} + 4e = 2H_2O_{(l)} \qquad E^\circ = 1.23\ V$$

The values show that the oxidation of silver sulphide to silver chloride and sulphur by either $Cu^{2+}_{(aq)}$ or $Fe^{3+}_{(aq)}$ is indeed thermodynamically favourable under standard conditions (unit activities of reactants and products). They also suggest that, after reduction to copper (I) or iron (II), the regeneration of $Cu^{2+}_{(aq)}$ or $Fe^{3+}_{(aq)}$ by atmospheric oxidation is also thermodynamically favourable. Although the figure of 1.23 V for the oxygen electrode refers to unit activity of hydrogen ions, in the pH range of 3-4 which prevails in the solution, the value will only be lowered to about 1.0 V. Thus oxidation of copper (I) or iron (II) by atmospheric oxygen is still very favourable in a thermodynamic sense. In the case of copper, this oxidation is fast; in the case of iron, it is rather slow at room temperature.

Perhaps the most interesting feature of the redox potentials is the small difference between the values for the silver and copper systems. It is 0.07 V, and this suggests

only a small equilibrium constant for the reaction of copper (II) with Ag_2S in chloride solution. However, these standard potentials refer to a situation of unit activity in aqueous chloride ions. In the amalgamation process proper, and in the model used here, the concentrations, and therefore the activities of chloride are much higher than this. This tends to depress the redox potential of the silver system, and raise that of the copper one. Consequently the difference is increased, the reaction becomes more favourable, and a greater degree of oxidation of Ag_2S by copper (II) becomes possible at equilibrium. The high chloride concentration may also have valuable kinetic effects. It renders potentially insoluble products, the monochlorides of silver and copper, at least partially soluble in the form of chloride complexes, and prevents them from inhibiting further surface reactions. In summary then, the effects of the high chloride concentration may have beneficial results in both a kinetic and a thermodynamic sense. However, if the $[CuCl_3]^{2-}_{(aq)}$ product is being continuously removed by atmospheric oxidation, the thermodynamic effect will probably not be a crucial one.

4.8 The reaction between Ag_2S and $CuCl_2$ in dilute Cl^- solution.

Bargallo[26] and Rickard[8] have previously reported that one of the products of this reaction was the formation of a copper sulphide. The difference between the two reviews lies in the oxidation state of the copper. Bargallo[26] states that the oxidation state is +2, while Rickard[8] points out that both copper (I) and copper(II) sulphides have been suggested as possible products. So far in this investigation, as in the real amalgamation process, reactions have been performed in concentrated chloride solution. Under these circumstances, no direct evidence has been found for the existence of copper sulphide products; the main copper product is atacamite. However, when the atacamite was removed from the insoluble phase with acid

during the experiments of Section 4.4.1, the acid-insoluble phase still contained small quantities of copper, and a combination of classical and spectroscopic analysis showed that an upper limit could be assigned to them that might be as high as 10% of the total copper. As copper sulphides were precipitated in the presence of dilute hydrochloric acid during classical qualitative analysis[27], it is possible that this acid-insoluble copper might take the form of copper sulphides. High chloride concentrations tend to convert the copper to acid-soluble chloride-containing species such as $[CuCl_3]^{2-}_{(aq)}$ and atacamite. If copper sulphides are present in the acid insoluble residue, their abundance and detectability might be increased by lowering the background chloride concentration. In the hope that this was the case, the reaction between copper (II) and Ag_2S was carried out with a mixture of just Ag_2S and dissolved $CuCl_2.2H_2O$ in the absence of any additional background chloride (Table 4.1, experiment 5).

After the reaction had been allowed to proceed for 96 hours, the mixture was separated and both phases dried under an infrared lamp. After drying, X-ray powder diffraction characterisation was carried out.

The data recorded from the solid material formed, shown in Figure 4-13, showed the presence of AgCl with small peaks in the background. After comparison of these peaks with those stored in the JCPDS library it was found that these matched many different copper sulphide systems.

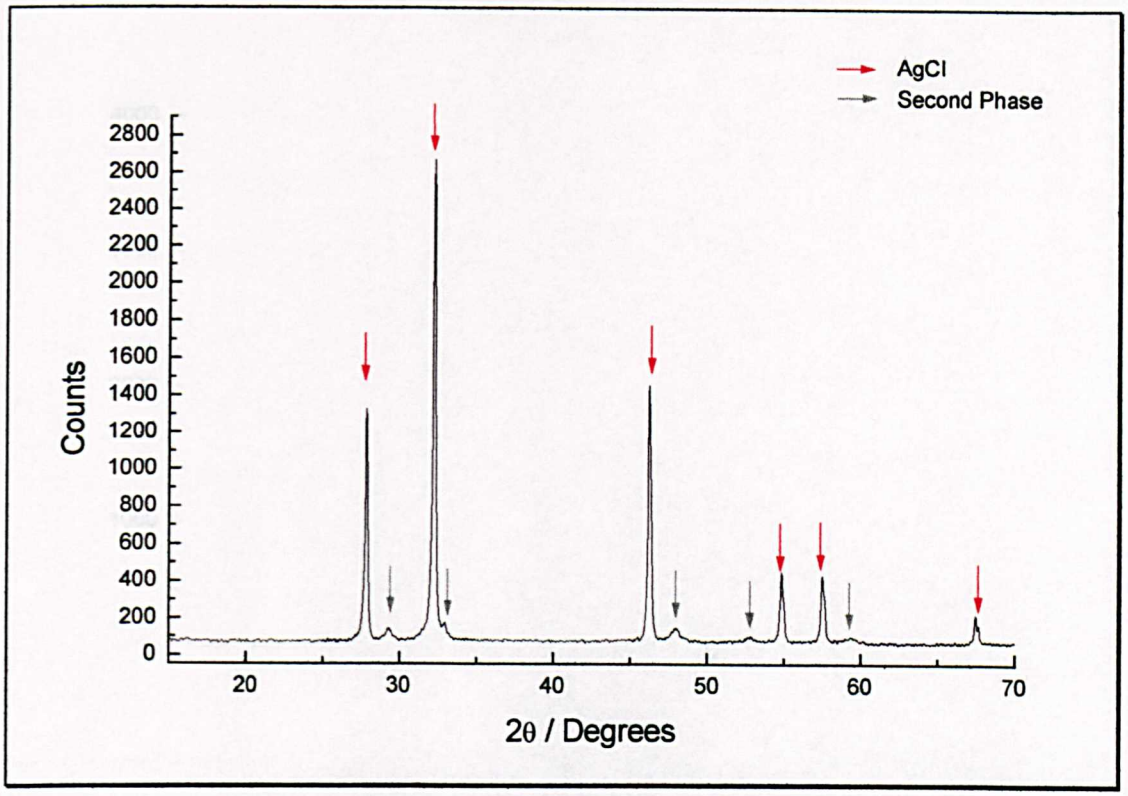

Figure 4-12 X-ray diffraction pattern recorded for residue from reaction between in Ag_2S and $CuCl_2$ in low Cl^- concentration, Expt 5.

To determine whether these copper systems were acid-soluble, and in the hope of reducing the number of possibilities, the solid material was washed in 2M HCl for 48 hours. After the material had been separated and dried, the X-ray powder diffraction pattern was again recorded (Figure 4-13). The pattern again showed the presence of another phase which had not diminished in intensity. The peaks are associated with acid-insoluble products. Such acid insolubility is a property of Cu_2S and CuS.

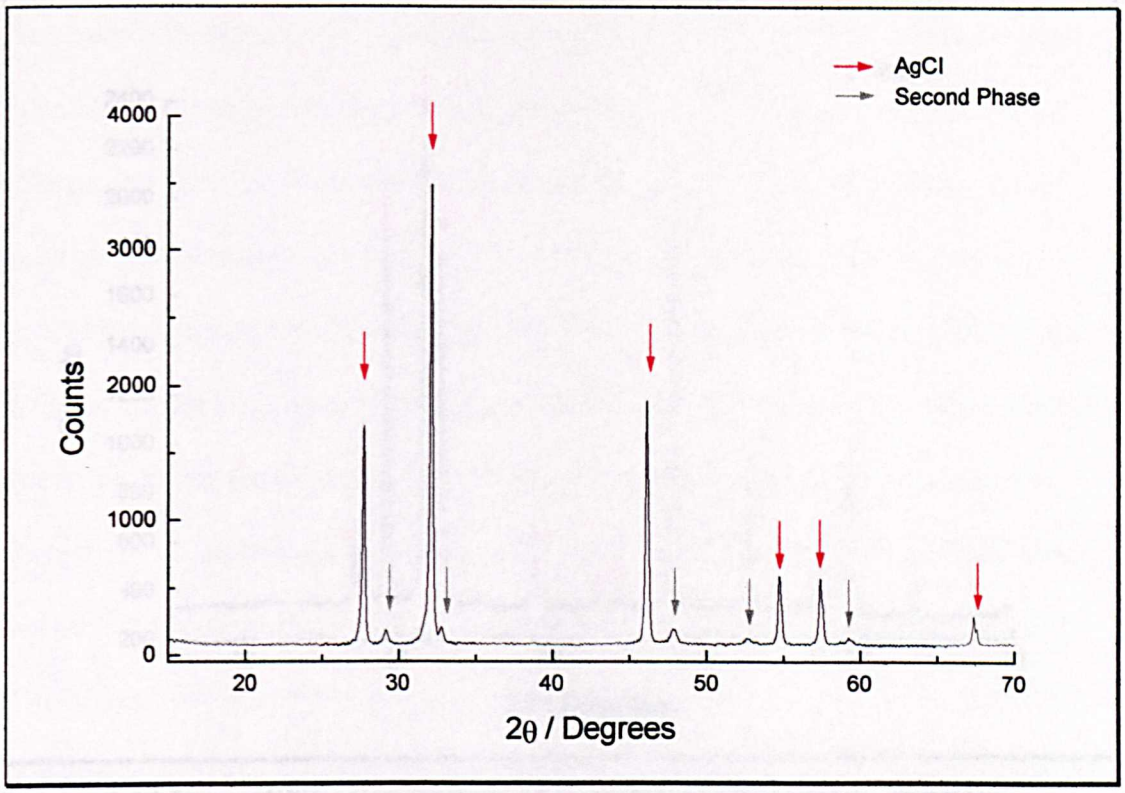

Figure 4-13 X-ray diffraction pattern recorded for residue from the washing of sample shown in Figure 4-12 with HCl, Expt5.

In order to determine whether the existence of copper sulphides affected the reaction in any manner, the following procedure was adopted. Cu_2S and CuS were mixed with $CuCl_2.2H_2O$ and stirred for 96 hours. After 96 hours the powders were filtered off, evaporated to dryness under an infrared lamp, and the X-ray powder diffraction pattern recorded, Figures 4-14 and 4-15.

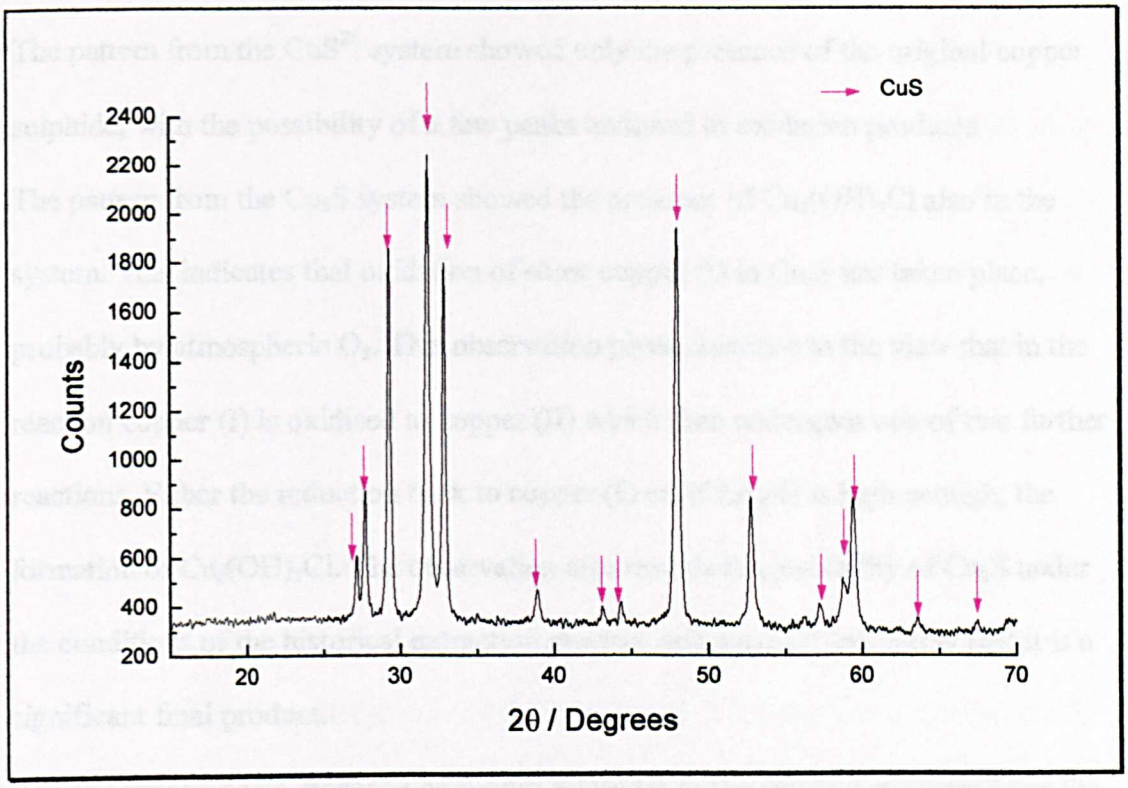

Figure 4-14 X-ray diffraction pattern recorded for residue from reaction between CuS and $CuCl_2$.

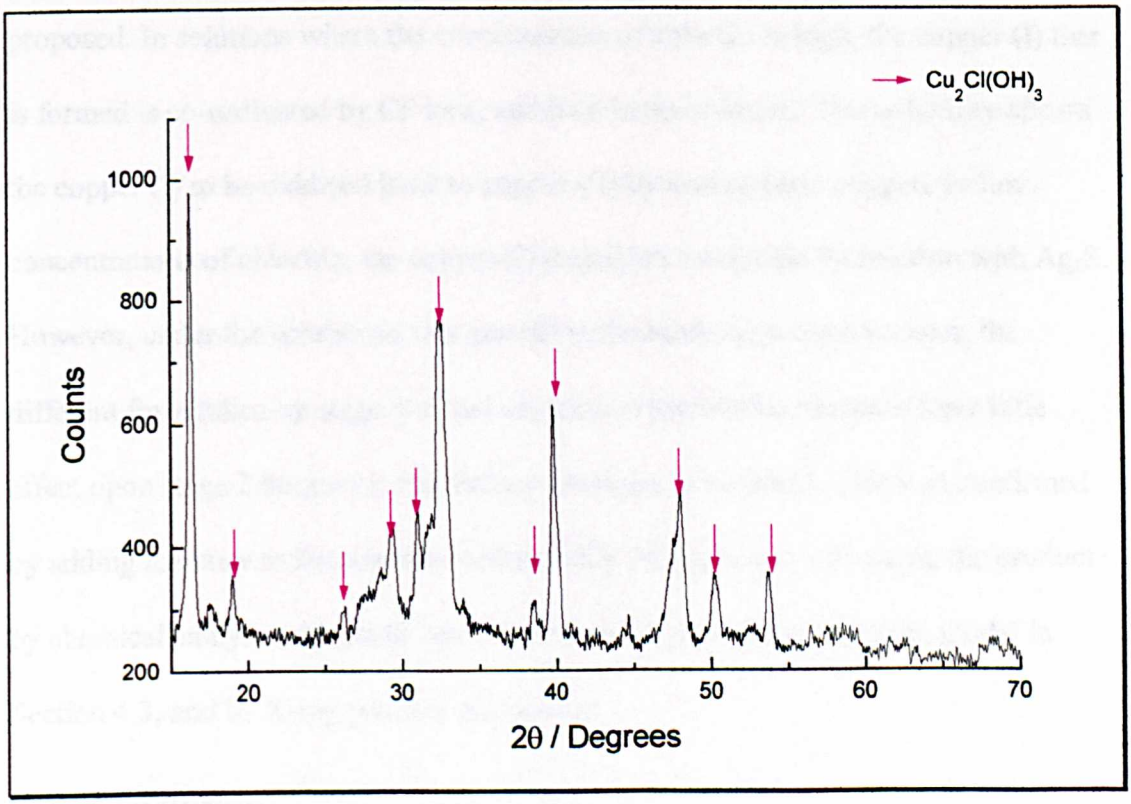

Figure 4-15 X-ray diffraction pattern recorded for residue from reaction between Cu_2S and $CuCl_2$.

The pattern from the CuS[28] system showed only the presence of the original copper sulphide, with the possibility of a few peaks assigned to oxidation products.

The pattern from the Cu_2S system showed the presence of $Cu_2(OH)_3Cl$ also in the system. This indicates that oxidation of some copper (I) in Cu_2S has taken place, probably by atmospheric O_2. This observation gives credence to the view that in the reaction copper (I) is oxidised to copper (II) which then undergoes one of two further reactions. Either the reduction back to copper (I) or, if the pH is high enough, the formation of $Cu_2(OH)_3Cl$. The observation also reveals the instability of Cu_2S under the conditions of the historical extraction process, and makes it less likely that it is a significant final product.

Because there was no evidence of copper sulphides in the patterns recorded from the experiments carried out in a high chloride concentration, the following explanation is proposed. In solutions where the concentration of chloride is high, the copper (I) that is formed is co-ordinated by Cl^- ions, and held in the solution. This solubility allows the copper (I) to be oxidised back to copper (II) by atmospheric oxygen. In low concentrations of chloride, the copper (I) may form a sulphide by reaction with Ag_2S. However, under the conditions that prevail in the model process used here, the different form taken by stage 1 at low chloride concentration seems to have little effect upon stage 2 because a satisfactory amalgam is obtained. This was confirmed by adding mercury to the reaction mixture after 24 hours and examining the product by chemical analyses, identical with those used for the validation of the model in Section 4.3, and by X-ray powder diffraction.

4.9 Conclusion.

Using the results presented above, it is now possible to present a reaction scheme for the chemistry of the amalgamation process. As stated earlier, the real historical

process was carried out at very high concentrations of chloride ions which were generated by the use of salt. The proposed reaction scheme under these conditions is as follows.

(i) Aqueous copper (II) oxidises Ag_2S to elemental sulphur, with the formation of AgCl, by undergoing reduction to copper (I) complexes, the principal product being $[CuCl_3]^{2-}_{(aq)}$:

$$2Cu^{2+}_{(aq)} + Ag_2S_{(s)} + 8Cl^-_{(aq)} \rightarrow 2AgCl_{(s)} + 2[CuCl_3]^{2-}_{(aq)} + S_{(s)} \quad (4.1)$$

(ii) The copper (I) complexes are then oxidised to copper (II) by the effect of the oxygen absorbed from the air. The nature of the copper (II) product depends upon the pH. Initially, the aerial oxidation will regenerate soluble copper (II) in the form of the aqueous ion, $Cu^{2+}_{(aq)}$, or its weak chloro-complexes that exist at high chloride ion concentrations:

$$2[CuCl_3]^{2-}_{(aq)} + 1/2O_2(g) + 2H^+_{(aq)} \rightarrow 2Cu^{2+}_{(aq)} + H_2O + 6Cl^-_{(aq)} \quad (4.3)$$

This soluble copper (II) is then freshly available for further oxidation of Ag_2S via equation 4.1. However, eventually, the pH increase brought about by equation 4.3 will cause the regenerated copper (II) to be precipitated as atacamite. This seems to occur when the pH reaches a value of about 4:

$$2CuCl_3^{2-}_{(aq)} + 1/2O_2(g) + 2H_2O \rightarrow Cu_2(OH)_3Cl_{(s)} + 5Cl^-_{(aq)} + H^+_{(aq)} \quad (4.2)$$

This removes the copper from any further participation in the reaction.

(iii) Once mercury has been added, the silver chloride that is formed in equation 4.1 can undergo reduction to silver amalgam, the other product being calomel:

$$(n+2)Hg_{(l)} + 2AgCl_{(s)} \rightarrow Ag_2Hg_{n(s)} + Hg_2Cl_{2(s)} \quad (4.7)$$

(iv) Mercury, however, also reacts with the sulphur generated in reaction 4.1 to form cinnabar, HgS:

$$Hg_{(l)} + S_{(s)} \rightarrow HgS_{(s)} \qquad (4.8)$$

This reaction provides one of the reasons why an amount of mercury greater than that needed just to reduce silver chloride to silver is consumed in the overall process. Another potential reason is that observed in Section 4.7: the reaction with dissolved copper (II) chloride to give, in the first place, mixed valence complexes of copper(I) and copper(II). If the copper (I) produced in this way then underwent atmospheric oxidation via equation 4.3, the soluble copper(II) that is produced would become available for the destruction of further mercury. Much mercury could thereby be wasted. This could explain why historical accounts of the process note that the addition of too much *magistral* to the reacting mass increases the consumption of mercury[1]. It also provides a reason why the addition of mercury to the reacting mass is delayed. The interval allows time for the salt, the copper (II) and the silver ore to become thoroughly mixed, and for a substantial amount of soluble copper to be converted into insoluble atacamite. In this form, the copper (II) does not react with mercury. Percy[1] noted that a green precipitate was often observed on the surface of the reacting mud. This is presumably the atacamite product.

When the high concentrations of chloride that existed during the real amalgamation process are made a part of the model used in this work, no direct evidence is found for the formation of copper sulphides. It is, however, possible that such sulphides account for the small amounts of copper that occur in the acid-insoluble residue left after the reaction is over. However, the major insoluble copper product is certainly atacamite, and this rules out the reaction schemes proposed by Bargallo [26] and Rickard [8]. Stronger evidence of copper sulphide formation is found when the chloride concentration is lowered, but is of very limited relevance for the real process in which the different elements were used in a ratio Ag : Cu : Hg : Cl of 2 : 3 : 6 :

120. Here, the high chloride concentration keeps the copper (I) and silver (I) chloride species in at least a partially soluble form and prevents them hindering surface reactions. It would also allow the copper (I) complex, and any soluble copper (II) into which it is converted by aerial oxidation, to percolate through the entire mass of treated ore. This would have a beneficial effect on the kinetics of the process, and favour the reaction scheme proposed here at the expense of one in which insoluble sulphides are formed.

The reaction scheme proposed above can now be used to understand the physical operations in stages (iii)-(v) of the process as outlined in the introduction to this thesis:

Stage (iii) – Salt was added to the wet mixture which was then thoroughly trodden. This would ensure that a concentrated aqueous chloride solution was thoroughly dispersed throughout the entire mass of treated ore.

Stage (iv) – The addition of *'magistral'*; this would react with the silver sulphide to form the copper (I) and AgCl species which, due to the concentrated chloride medium, would exist either wholly or partially in the form of soluble chloride complexes. The copper (I) could then be oxidised by atmospheric oxygen to form either soluble copper (II) or atacamite. Soluble iron (III) in the *magistral* would also oxidise silver sulphide in a similar fashion but, in this case, the atmospheric oxidation of the iron (II) product that is formed is slow.

Stage (v) – The addition of mercury reduces the silver chloride or its chloride complexes. Further mercury then forms an amalgam with the silver that is formed. Of the previous work carried out on this system the reaction scheme which agrees most closely with this work is that of Percy [29]. Percy only published the results of his studies of the reaction between copper compounds and Ag_2S in a chloride medium,

but he noted the formation of elemental sulphur and copper (I) which he assumed to exist as the monochloride. He also recognised that the copper (I) species was oxidised by air to a basic chloride of copper. He promised a completed study of the amalgamation process at a later date, but this work remained unpublished at his death.

4.10 References.

1. J Percy, *Metallurgy; Silver and Gold Part 1*, John Murray, London, 1880, pp. 576-608.

2. L.G Sillen and A.E Martell, *Stability of Metal-Ion Complexes*, Special Publication No. 17, Royal Society of Chemistry , London, 1964.

3. A Pinkus and A.M Timmermans, *Bull Soc Chim Belges*, 1937, **46**, 46.

4. JCPDS Card Number 31-1238

5. JCPDS Card Number 25-0269

6. JCPDS Card Number 5-0628

7. JCPDS Card Number 33-0451

8. T.A Rickard, *The Canadian Institute Of Mining and Metallurgy*, 1936, 23.

9. P.J Bakewell, *The Cambridge History of Latin America*, Cambridge University Press, Cambridge, 1984, pp. 105-151.

10. P.J Bakewell, *Silver Mining and Society in Colonial Mexico; Zacatecas 1546-1700*, Cambridge University Press, Cambridge, 1971, p. Chapter 6.

11. A.I Vogel, *A Textbook of Quantitative Inorganic Analysis*, Longmans, London, 1939.

12. A.G Sharpe , *Principles of Oxidation and Reduction*, Royal Institue of Chemistry, London, 1962, p. 20.

13. R Vestin, A Somersalo and B Mueller, *Acta Chem Scand*, 1953, **7**, 745.

14. B Liedholm, *Acta Chem Scand*, 1969, **23**, 3175.

15. J.B Sharkey and S.Z Lewin, *Am. Mineral.*, 1971, **56**, 179.

16. F.A Cotton and G Wilkinson, *Advanced Inorganic Chemistry*, Wiley, New York, 5th edn., 1989, pp. 773-773 and 1276.

17. M Mori, *Bull Chem Soc Jpn*, 1960, **33**, 985.

18. M.B Robin and P.Day, *Adv Chem Inorg Chem Radiochem*, 1967, **10**, 312.

19. JCPDS Card Number 11-0067

20. JCPDS Card Number 26-0312

21. JCPDS Card Number 6-0261

22. JCPDS Card Number 6-0565

23. JCPDS Card Number 16-0123

24. J.E Dutrizac, *Hydrometallurgy*, 1994, **35**, 275.

25. D.D Wagman, W.H Evans, V.B Parker, R.H Schumm, I Halow, S.M Bailey, K.L Churney and R.L Nuttall, *The NBS Tables of Chemical*

Thermodynamic Properties, American Institute of Physics, New york, 1982.

26. M Bargallo, *La Mineria y La Metalurgica En La America Espanola Durante La Epoca Colonial*, Mexico, 1955, p. 194.

27. A.I Vogel, *A Textbook of Macro and Semimicro Quantitative Analysis*, Longmans, London, 4th edn., 1954.

28. JCPDS Card Number 6-0464

29. J Percy, *Metallurgy; Silver and Gold Part 1*, John Murray, London, 1880, pp. 73-84.

CHAPTER 5 - RESULTS AND DISCUSSION

RARE EARTH DOPED HEXAFERRITES.

5.1 Hexaferrites prepared by the calcination of oxides.

5.1.1 X-ray powder diffraction.

The X-ray powder diffraction patterns recorded from samples made by the calcination of oxides are shown in Figure 5-1. The patterns show the presence of $SrFe_{12}O_{19}$ or a $SrFe_{12}O_{19}$-related phase. The peaks resulting from the silicon standard used to calibrate the positions are indicated.

5.1.1.1 Lattice Parameters.

The unit cell parameters were calculated using a standard least squares fitting routine supplied by Siemens and also by using the DICVOL91[1] program. Three different measurements were carried out on each sample. The calculated unit cell parameters were independent of the program used and are presented in Table 5-1.

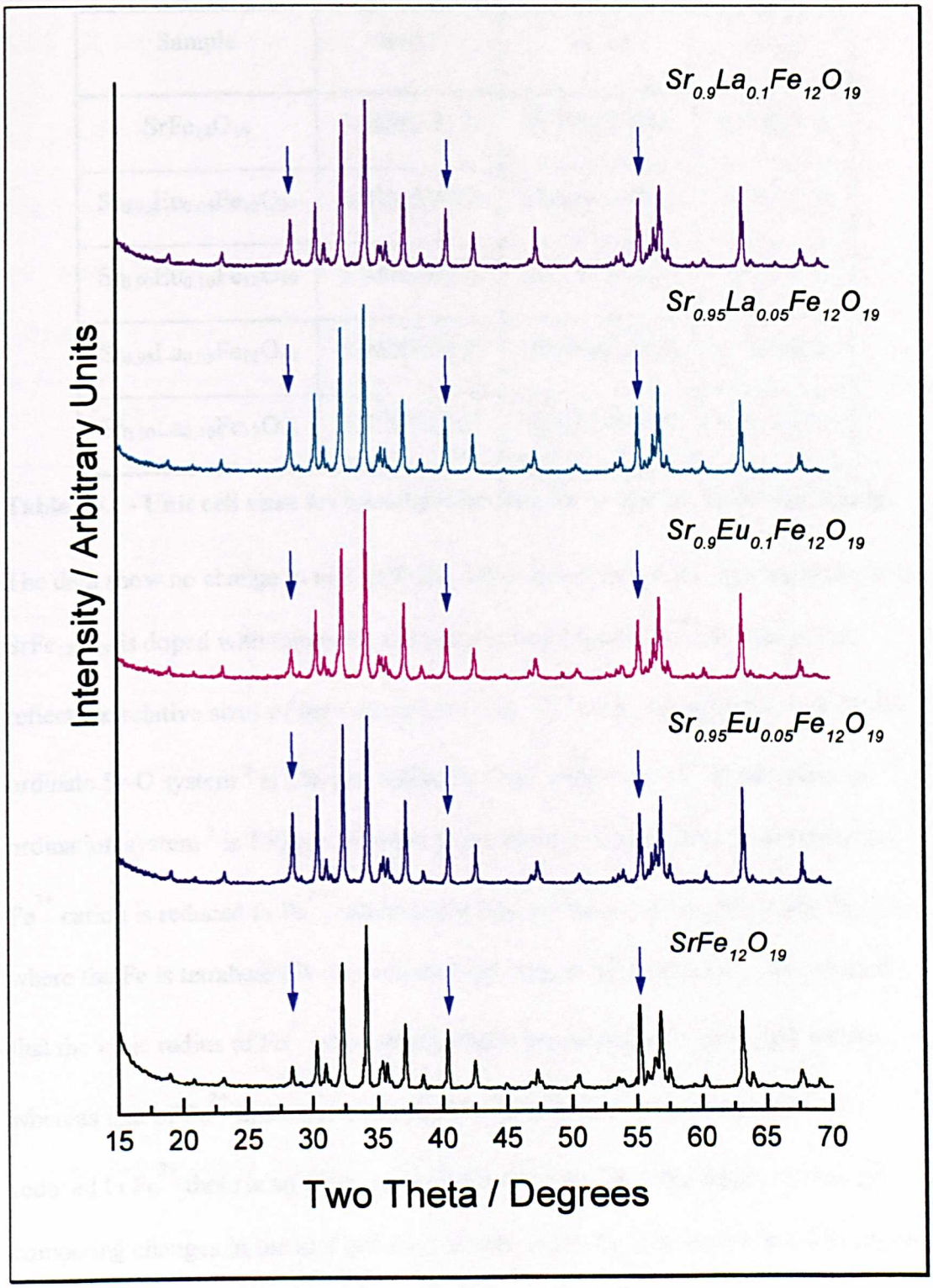

Figure 5-1 X-ray powder diffraction patterns recorded from hexaferrites made by calcination of oxides, arrows mark the Silicon peaks.

Sample	a (Å)	c (Å)	Vol ($Å^3$)
$SrFe_{12}O_{19}$	5.888(0.017)	23.040(0.086)	691.8(6.6)
$Sr_{0.95}Eu_{0.05}Fe_{12}O_{19}$	5.883(0.016)	23.041(0.081)	690.6(6.5)
$Sr_{0.90}Eu_{0.10}Fe_{12}O_{19}$	5.885(0.015)	23.051(0.085)	691.3(6.2)
$Sr_{0.95}La_{0.05}Fe_{12}O_{19}$	5.882(0.015)	23.042(0.084)	690.4(6.0)
$Sr_{0.90}La_{0.10}Fe_{12}O_{19}$	5.879(0.021)	23.026(0.081)	689.1(8.2)

Table 5 -1 - Unit cell sizes for hexaferrites formed by the calcination of oxides.

The data show no change in unit cell size within the errors of the measurement, when $SrFe_{12}O_{19}$ is doped with rare earth elements by solid state reactions. The results reflect the relative sizes of the cations involved. The ionic radius of Sr^{2+} in a 12 co-ordinate Sr-O system [2] is 158 pm, while the ionic radius for La^{3+} in the same co-ordination system [2] is 150 pm. In order to conserve charge balance in the system a Fe^{3+} cation is reduced to Fe^{2+}, which according to Sauer et al[3] occurs at the 2a site where the Fe is tetrahedrally co-ordinated by oxygen. Shannon et al[4] has reported that the ionic radius of Fe^{3+} when tetrahedrally co-ordinated by oxygen is 49 pm, whereas that of Fe^{2+} in similar co-ordination is 63 pm. Therefore when Fe^{3+} is reduced to Fe^{2+} there is an increase in radius of 14 pm. In these systems there are competing changes in the unit cell size, which results in no overall change in lattice parameters.

5.1.2 X-ray Absorption Fine Structure (XAFS).

5.1.2.1 Sr K-edge.

The Sr K-edge XAFS data for two samples are shown in Table 5-2. A typical spectrum is shown in Figure 5-2. The results agree well with the single crystal data published by Kimura et al[5], which are given in Table 5-3.

Sample	Shell	Element	CN	R (Å)	$2\sigma^2$ (Å^2)	R-value
$SrFe_{12}O_{19}$	1	O	6	2.73	0.026	32.8
	2	O	6	2.90	0.028	
	3	Fe	3	3.39	0.023	
	4	Fe	12	3.62	0.025	
$Sr_{0.90}Eu_{0.10}Fe_{12}O_{19}$	1	O	6	2.74	0.026	40.7
	2	O	6	2.91	0.026	
	3	Fe	3	3.37	0.022	
	4	Fe	12	3.62	0.025	

Table 5 -2 Best fit parameters for Sr K-edge XAFS data recorded from hexaferrites prepared by the calcination of oxides.

Shell	CN	Atom	Radius (Å)
1	6	O	2.820
2	6	O	2.946
3	3	Fe	3.399
4	12	Fe	3.650

Table 5 -3 Crystallographic environment of Sr in $SrFe_{12}O_{19}$ derived from single crystal X-ray diffraction data[5]

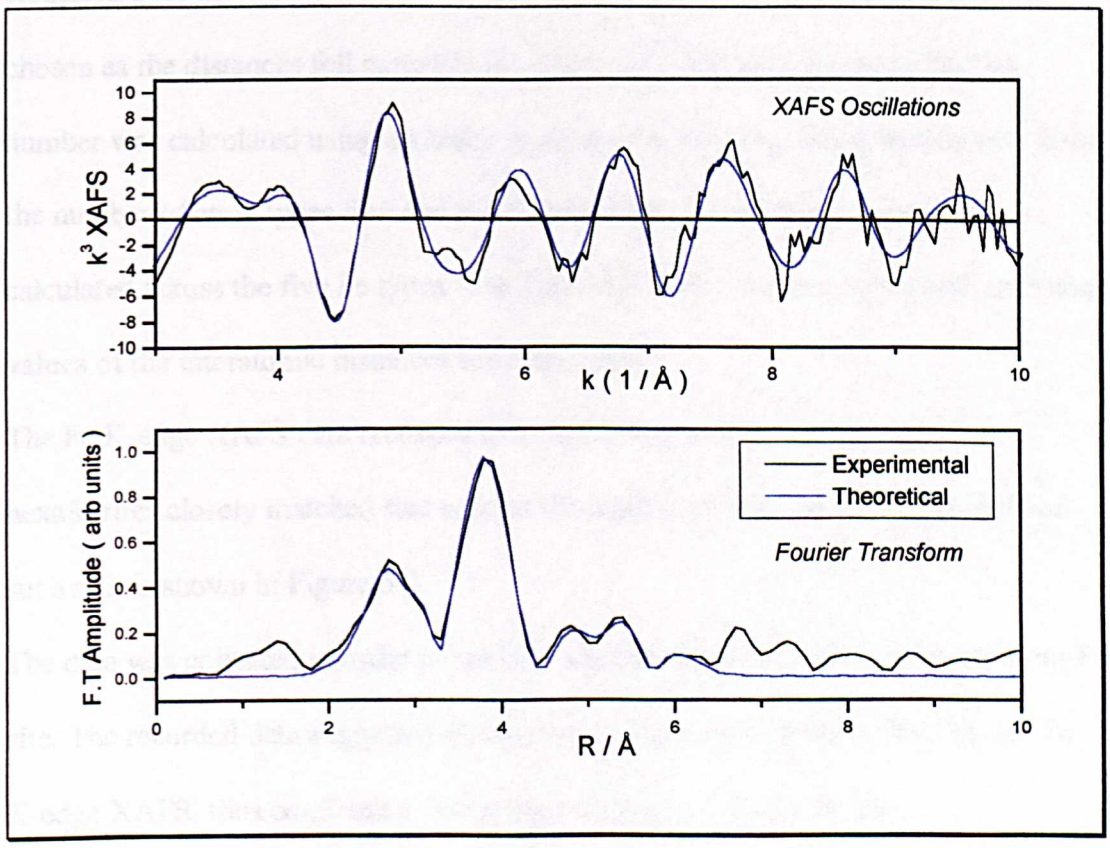

Figure 5-2 Sr K-edge XAFS recorded from $SrFe_{12}O_{19}$.

5.1.2.2 Fe K-edge

The Fe K-edge XAFS were measured in order to confirm that the rare-earth element was not doping onto a Fe site. The data once recorded were found to be complicated for the reason outlined below.

Due to the nature of the $SrFe_{12}O_{19}$ structure, there are 5 crystallographic Fe sites, Section 1.3.1, and so the Fe K-edge XAFS is complex. These sites each eject a photoelectron which contributes to the observed XAFS oscillations.

In order to analyse the recorded data it was necessary to construct a model structure using single crystal data, with the calculation for the average distances being weighted over the five iron sites. The average distances shown in Table 5-4 were chosen as the distances fell naturally into these sets. The average co-ordination number was calculated using a similar method with the value being determined from the number of atom types found at the distances set. All average values were calculated across the five Fe types. The Table indicating the maximum and minimum values of the interatomic distances for each range.

The Fe K-edge XAFS data recorded from $SrFe_{12}O_{19}$ and lanthanum doped hexaferrites closely matched that used in the model outlined above, an example of such a fit is shown in Figure 5-3.

The data was collected in order to confirm whether the dopant resided on the Sr or Fe site. The recorded data suggests that the dopant has no measurable effect on the Fe K-edge XAFS, thus confirming that doping takes place on the Sr site.

The XAFS data recorded from the Fe K-edge are shown in Appendix 1.

Shell	CN	Atom	Distance (Å)
1	3.9	O	1.9±0.1
2	1.6	O	2.1±0.1
3	3.0	Fe	2.95±0.1
4	1.3	Sr	3.45±0.2
5	5.4	O	3.45±0.2
6	6.5	Fe	3.45±0.2

Table 5 -4 Average Fe K-edge XAFS calculated for $SrFe_{12}O_{19}$ to a distance of 5Å.

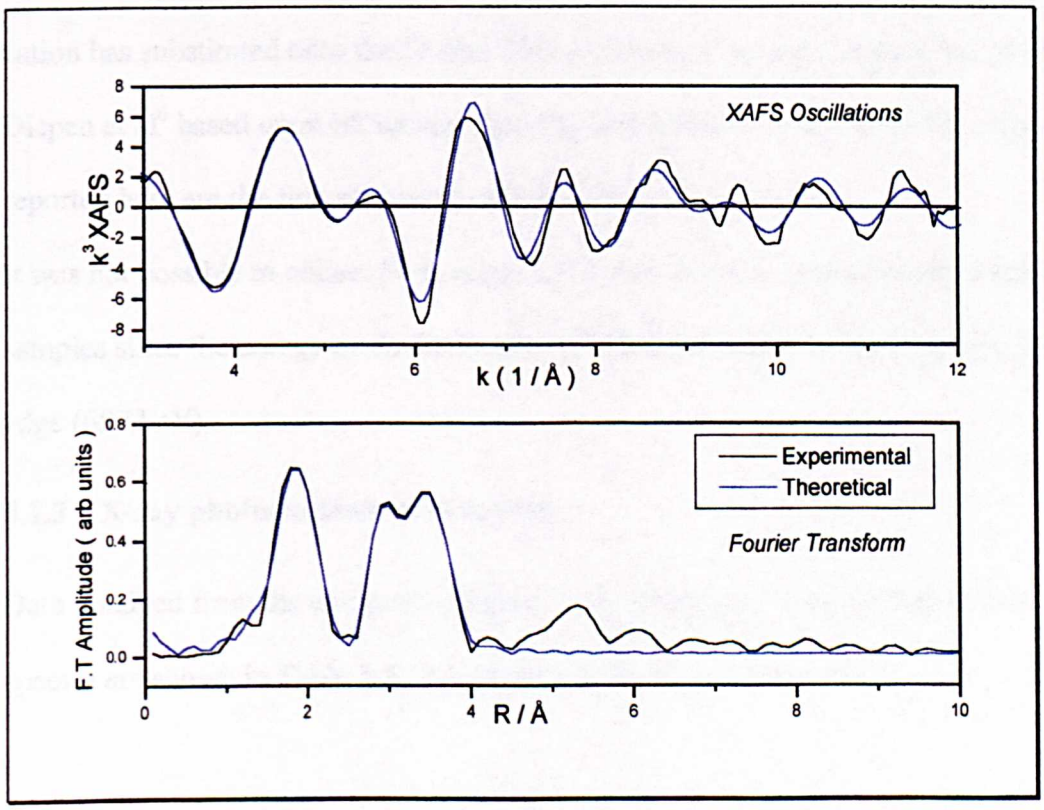

Figure 5-3 Fe K-edge XAFS data recorded from $SrFe_{12}O_{19}$ and fitted to the average model.

5.1.2.3 La L_{III}-Edge

Sample	Shell	Element	CN	R (Å)	$2\sigma^2$(Å^2)	R-value
$Sr_{0.90}La_{0.10}Fe_{12}O_{19}$	1	O	6	2.72	0.007	35.1
	2	O	6	3.01	0.011	
	3	Fe	3	3.47	0.019	

Table 5 -5 Best fit parameters to La L_{III} edge XAFS recorded from hexaferrite prepared by the calcination of oxides.

The La L_{III} edge data recorded from $Sr_{0.9}La_{0.1}Fe_{12}O_{19}$, shown in Table 5-5, matches that recorded from the Sr K-edge, shown in Table 5-2. This indicates that the La cation has substituted onto the Sr site. This is consistent with the suggestion of van Diepen et al[6] based upon Mössbauer spectral data recorded from $LaFe_{12}O_{19}$. The data reported here are the first structural evidence for such a process.

It was not possible to collect Fe K-edge XAFS data from the europium-containing samples since the energy of the Fe K-edge (7112 eV) is close to that of the Eu L_{III} edge (6972 eV).

5.1.3 X-ray photoelectron spectroscopy.

Data obtained from the computer analysis of the calibrated X-ray photoelectron spectra are shown in Table 5-6. A spectrum is shown in Figure 5-4.

Sample	Element	Electronic Level	Binding Energy ±0.1 (eV)
$SrFe_{12}O_{19}$	Fe	2p	710.3
	Sr	3d	133.3
$Sr_{0.95}Eu_{0.05}Fe_{12}O_{19}$	Fe	2p	710.5
	Sr	3d	133.2
	Eu	4f	1134.8
$Sr_{0.90}Eu_{0.10}Fe_{12}O_{19}$	Fe	2p	710.4
	Sr	3d	133.2
	Eu	4f	1134.6
$Sr_{0.95}La_{0.05}Fe_{12}O_{19}$	Fe	2p	710.4
	Sr	3d	133.3
	La	4f	834.4
$Sr_{0.90}La_{0.10}Fe_{12}O_{19}$	Fe	2p	710.2
	Sr	3d	133.1
	La	4f	835.3

Table 5 -6 Binding energies recorded by X-ray photoelectron spectroscopy.

When the data are compared with that recorded from standards (Table 5-7) and in the literature[7,8], it is found that the Sr and Fe are present as the Sr^{2+} and Fe^{3+} cations. The data collected from the rare earth elements broadly match those collected from Eu_2O_3 and La_2O_3 (Table 5-7). As such they indicate that these elements are in the tripositive state.

Compound	Cation	Electronic Shell	Binding Energy (eV)
Fe_2O_3	Fe^{3+}	2p	710.8[7], 711.0[8]
$SrCO_3$	Sr^{2+}	3d	133.6
Eu_2O_3	Eu^{3+}	4f	1132.2
La_2O_3	La^{3+}	4f	833.7

Table 5 -7 Binding energies of standards used for the interpretation of recorded XPS data.

Due to the low level of dopant the recorded X-ray photoelectron spectra from the rare earth elements show a broad peak of little intensity. As a result the assignment of peak centre, and subsequently binding energy, is difficult and contains a relatively large degree of error. Such an explanation can be used to explain the difference, ~ 1.5 eV, between the rare earth oxide standards and the recorded data.

The presence of Eu^{3+} and La^{3+} would be expected to produce a Fe^{2+} component. However, due to the low level of dopant used here any contribution arising from Fe^{2+} is masked by the large Fe^{3+} component. A shoulder on the Fe^{3+} spectrum and a satellite peak at 714 eV would normally indicate the presence of Fe^{2+}.

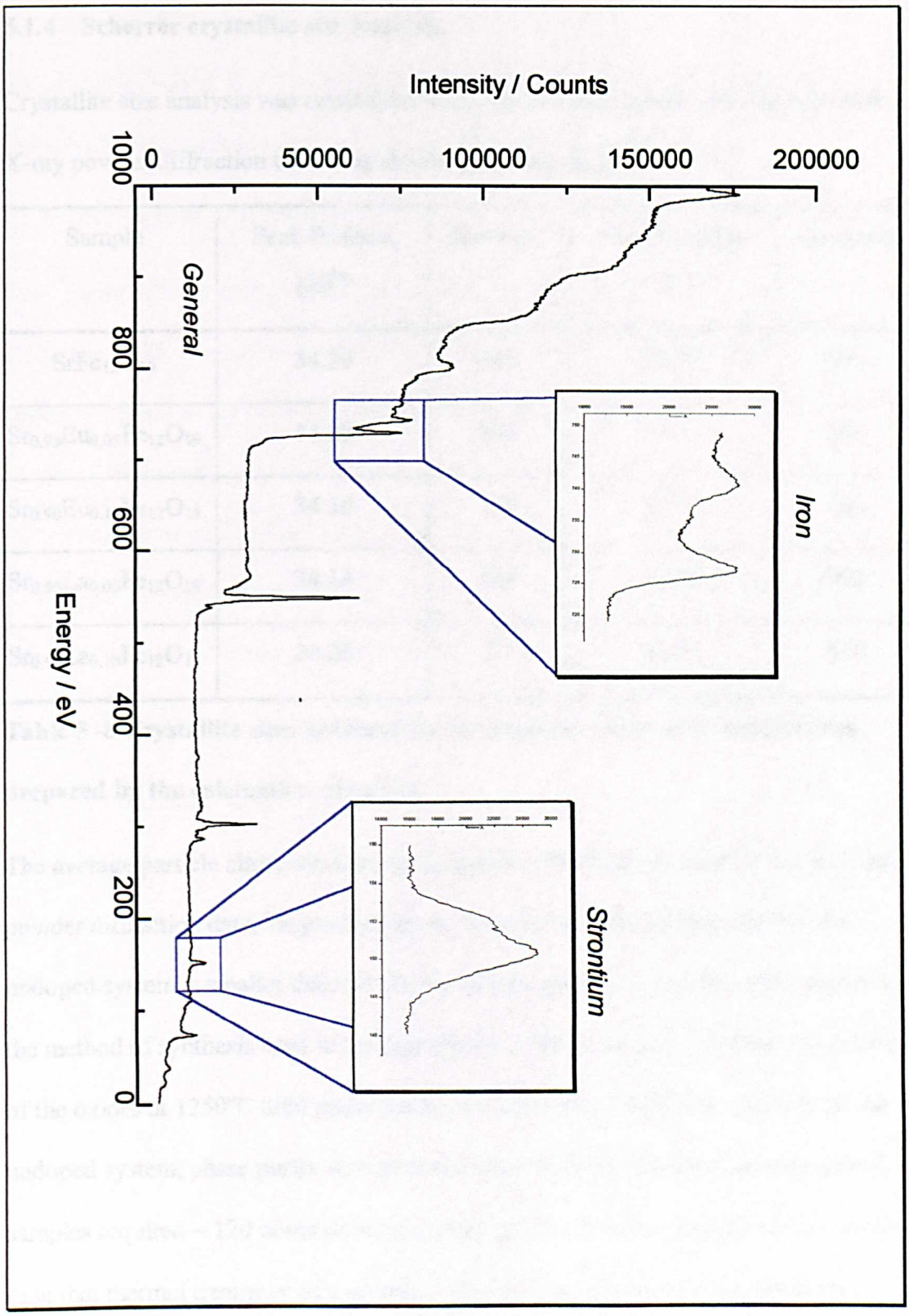

Figure 5-4 X-ray photoelectron spectrum recorded from $SrFe_{12}O_{19}$.

5.1.4 Scherrer crystallite size analysis.

Crystallite size analysis was carried out using the Scherrer equation on the recorded X-ray powder diffraction data. The results are shown in Table 5-8.

Sample	Peak Position (2θ°)	Size (nm)	Peak Position (2θ°)	Size (nm)
$SrFe_{12}O_{19}$	34.20	490	32.35	570
$Sr_{0.95}Eu_{0.05}Fe_{12}O_{19}$	34.26	800	32.41	880
$Sr_{0.90}Eu_{0.10}Fe_{12}O_{19}$	34.26	700	32.41	600
$Sr_{0.95}La_{0.05}Fe_{12}O_{19}$	34.14	740	32.29	890
$Sr_{0.90}La_{0.10}Fe_{12}O_{19}$	34.26	670	32.41	650

Table 5 -8 Crystallite sizes obtained by the Scherrer method for hexaferrites prepared by the calcination of oxides.

The average particle sizes, obtained from applying the Scherrer equation to the X-ray powder diffraction data, vary according to composition. The particle size for the undoped system is smaller than that for the doped systems. As outlined in Chapter 3, the method of synthesis used in the preparation of these samples involves calcination of the oxides at 1250°C until phase purity was achieved. During the synthesis of the undoped system, phase purity was achieved after 48 hours. Contrastingly the doped samples required ~ 120 hours to achieve phase purity. It has been accepted for some time that thermal treatment of a sample at elevated temperature causes the particle size to increase[9]. Thus the $SrFe_{12}O_{19}$ sample heated for 48 hours has a smaller particle size than doped samples heat treated for 120 hours

The difference between the particle sizes given by the two angles, can be put down to error in peak definition. Although it may have been ideal to use more peaks, it proved difficult to get reliable data from peaks at higher angles.

5.1.5 Mössbauer Spectroscopy.

The ^{57}Fe Mössbauer parameters from spectra recorded at 25K, 55K, 77K, 155K, 215K, and 298K are shown in Tables 5-9 to 5-13. The fitting process applied the same constraints to the fitting of all spectra. The constraints were:

(i) Standard Lorentzian lines.

(ii) Equal width of peaks in the sextet.

(iii) The area of the outer lines being three times the area of the inner lines.

The middle lines were allowed to fit freely.

5.1.5.1 ^{57}Fe Mössbauer spectra recorded from $SrFe_{12}O_{19}$.

The ^{57}Fe Mössbauer parameters obtained from computer fitting of the spectra are shown in Table 5-9. The spectra are shown in Figure 5-5. The assignment of the subspectra with specific Fe sites in the $SrFe_{12}O_{19}$ structure are based upon the interpretation of spectra of $SrFe_{12}O_{19}$ reported by Evans et al[10].

Temp (K)	Site	$\delta \pm 0.03$ (mm s^{-1})	$\Delta \pm 0.05$ (mm s^{-1})	H ± 0.5 (T)
298	2a	0.35	0.00	50.9
	$4f_1$	0.27	0.18	49.6
	$4f_2$	0.39	0.26	52.4
	2b	0.31	2.26	40.9
	12k	0.36	0.42	41.4
215	2a	0.23	0.06	48.3
	$4f_1$	0.31	0.14	50.3
	$4f_2$	0.40	0.22	52.2
	2b	0.39	2.34	41.7
	12k	0.39	0.40	43.9
155	2a, $4f_1$	0.43	0.34	53.0
	$4f_2$	0.34	0.14	50.8
	2b	0.38	2.32	42.2
	12k	0.44	0.40	47.2
77	2a, $4f_1$, $4f_2$	0.41	0.16	52.6
	2b	0.40	2.24	42.2
	12k	0.45	0.34	49.9
55	2a, $4f_1$, $4f_2$	0.42	0.20	52.8
	2b	0.42	2.26	42.3
	12k	0.45	0.34	50.2
25	2a, $4f_1$, $4f_2$	0.42	0.22	52.9
	2b	0.44	2.28	42.4
	12k	0.45	0.34	50.5

Table 5 -9 - ^{57}Fe Mössbauer parameters recorded from $SrFe_{12}O_{19}$ prepared by the calcination of oxides.

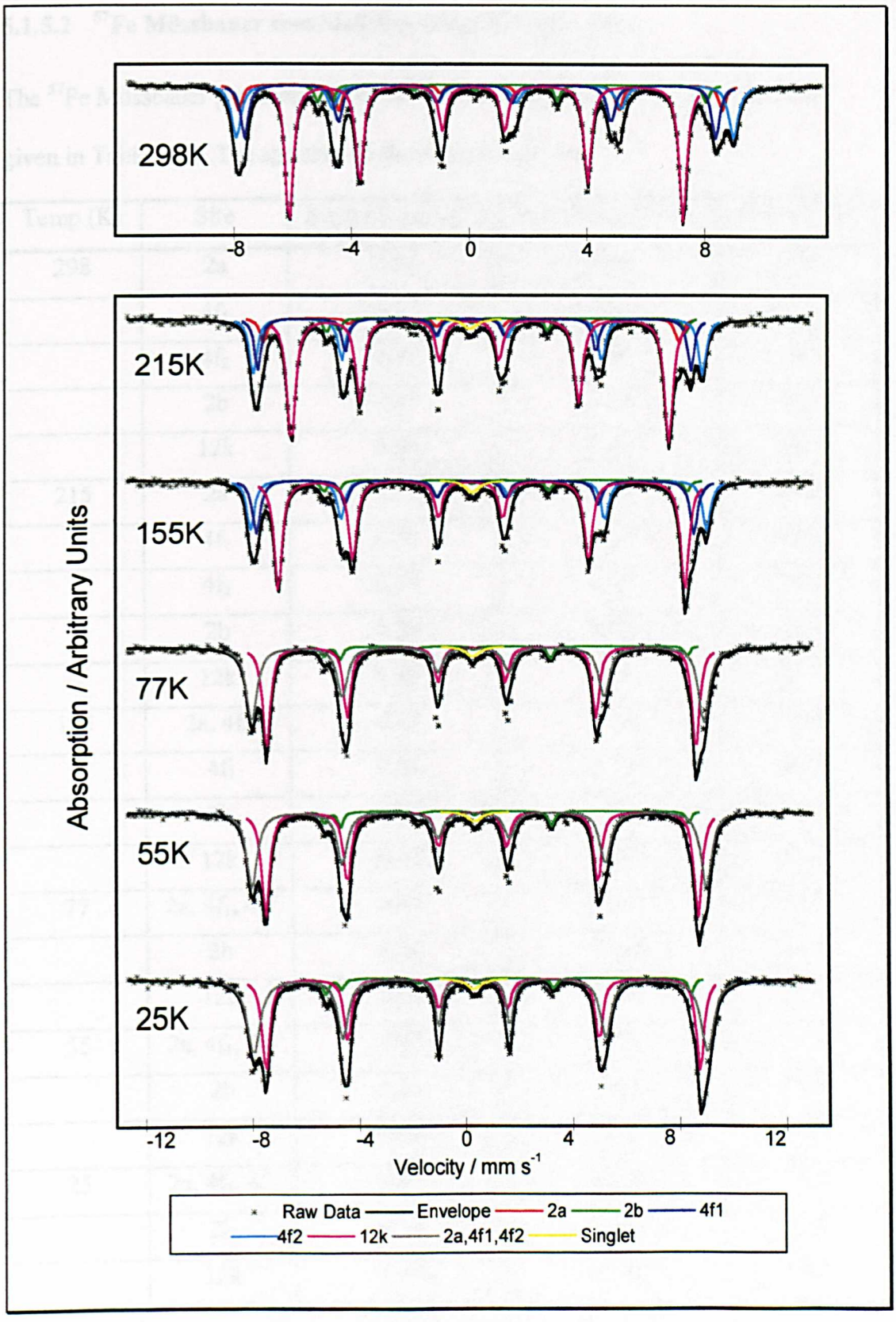

Figure 5-5 ^{57}Fe Mössbauer spectra collected from $SrFe_{12}O_{19}$ at various temperatures.

5.1.5.2 ^{57}Fe Mössbauer recorded from $Sr_{0.95}Eu_{0.05}Fe_{12}O_{19}$.

The ^{57}Fe Mössbauer parameters obtained from computer fitting of the spectra are given in Table 5-10. The spectra are shown in Figure 5-6.

Temp (K)	Site	$\delta \pm 0.03$ (mm s^{-1})	$\Delta \pm 0.05$ (mm s^{-1})	$H \pm 0.5$ (T)
298	2a	0.34	0.06	50.8
	$4f_1$	0.27	0.18	49.4
	$4f_2$	0.38	0.26	52.3
	2b	0.31	2.28	40.9
	12k	0.36	0.42	41.4
215	2a	0.19	0.00	47.8
	$4f_1$	0.31	0.14	50.2
	$4f_2$	0.39	0.18	52.2
	2b	0.34	2.32	41.4
	12k	0.38	0.38	43.7
155	2a, $4f_1$	0.42	0.18	52.8
	$4f_2$	0.34	0.14	50.7
	2b	0.38	2.34	42.4
	12k	0.43	0.38	47.2
77	2a, $4f_1$, $4f_2$	0.41	0.20	52.7
	2b	0.36	2.20	41.6
	12k	0.43	0.34	49.9
55	2a, $4f_1$, $4f_2$	0.43	0.20	52.8
	2b	0.31	2.34	42.1
	12k	0.44	0.34	50.1
25	2a, $4f_1$, $4f_2$	0.42	0.22	52.8
	2b	0.38	2.20	41.8
	12k	0.45	0.32	50.4

Table 5 -10 ^{57}Fe Mössbauer parameters recorded from $Sr_{0.95}Eu_{0.05}Fe_{12}O_{19}$ prepared by the calcination of oxides.

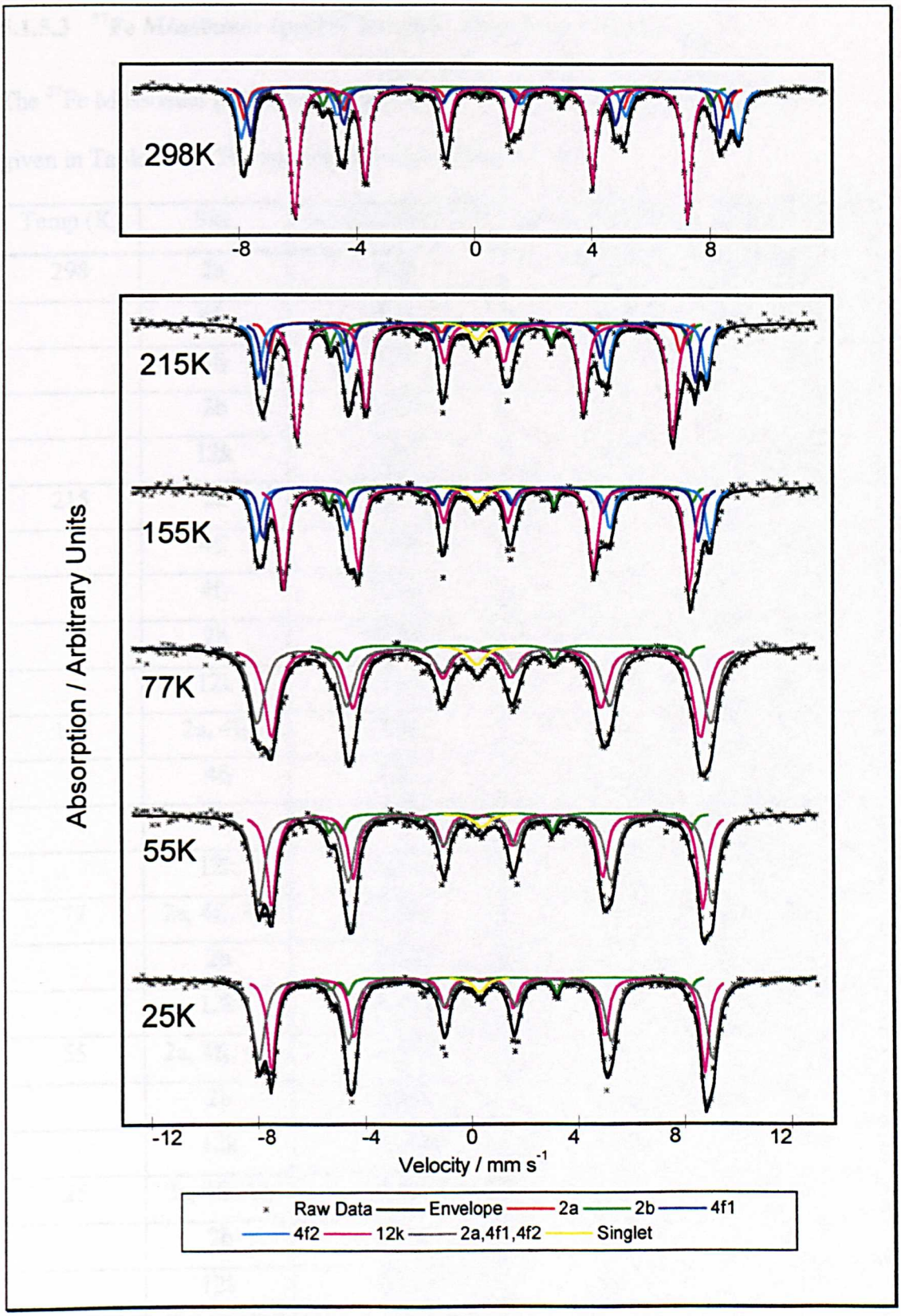

Figure 5-6 ^{57}Fe Mössbauer spectra recorded from $Sr_{0.95}Eu_{0.05}Fe_{12}O_{19}$ at various temperatures.

5.1.5.3 ^{57}Fe Mössbauer spectra recorded from $Sr_{0.90}Eu_{0.10}Fe_{12}O_{19}$.

The ^{57}Fe Mössbauer parameters obtained from computer fitting of the spectra are given in Table 5-11. The spectra are shown in Figure 5-7.

Temp (K)	Site	$\delta \pm 0.03$ (mm s^{-1})	$\Delta \pm 0.05$ (mm s^{-1})	H ± 0.5 (T)
298	2a	0.35	0.00	50.8
	$4f_1$	0.31	2.24	40.8
	$4f_2$	0.27	0.16	49.5
	2b	0.38	0.26	52.3
	12k	0.36	0.41	41.4
215	2a	0.21	0.00	48.2
	$4f_1$	0.32	0.12	50.3
	$4f_2$	0.40	0.20	52.2
	2b	0.37	2.30	41.8
	12k	0.40	0.38	44.2
155	2a, $4f_1$	0.44	0.20	52.7
	$4f_2$	0.33	0.14	50.6
	2b	0.39	2.36	42.2
	12k	0.43	0.38	47.1
77	2a, $4f_1$, $4f_2$	0.42	0.18	52.2
	2b	0.41	2.24	41.8
	12k	0.45	0.34	49.9
55	2a, $4f_1$, $4f_2$	0.43	0.22	52.5
	2b	0.40	2.26	42.0
	12k	0.45	0.34	50.0
25	2a, $4f_1$, $4f_2$	0.42	0.22	52.9
	2b	0.40	2.20	41.9
	12k	0.44	0.32	50.5

Table 5 -11 ^{57}Fe Mössbauer parameters recorded from $Sr_{0.90}La_{0.10}Fe_{12}O_{19}$ prepared by the calcination of oxides.

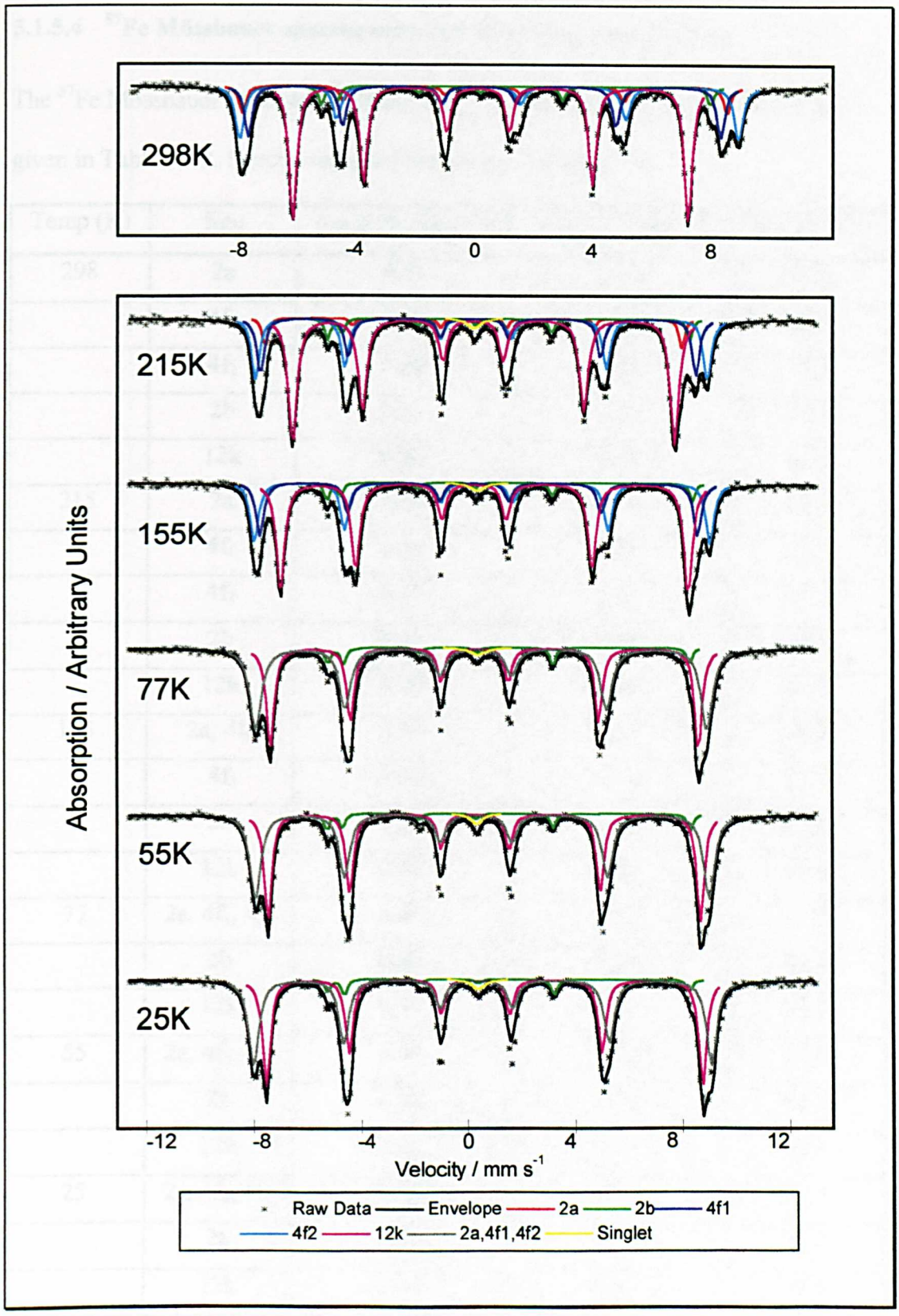

Figure 5-7 ^{57}Fe Mössbauer spectra recorded from $Sr_{0.90}Eu_{0.10}Fe_{12}O_{19}$ at various temperatures.

5.1.5.4 ^{57}Fe Mössbauer spectra recorded from $Sr_{0.95}La_{0.05}Fe_{12}O_{19}$.

The ^{57}Fe Mössbauer parameters obtained from computer fitting of the spectra are given in Table 5-12. Spectra recorded are shown in Figure 5-8 .

Temp (K)	Site	$\delta \pm 0.03$ (mm s^{-1})	$\Delta \pm 0.05$ (mm s^{-1})	H ± 0.5 (T)
298	2a	0.34	0.00	50.8
	$4f_1$	0.27	0.16	49.5
	$4f_2$	0.38	0.30	52.3
	2b	0.31	2.24	40.9
	12k	0.36	0.40	41.5
215	2a	0.19	0.00	48.9
	$4f_1$	0.30	0.14	51.2
	$4f_2$	0.41	0.22	53.4
	2b	0.35	2.36	42.5
	12k	0.40	0.40	44.6
155	2a, $4f_1$	0.44	0.30	54.3
	$4f_2$	0.36	0.18	52.1
	2b	0.38	2.10	42.3
	12k	0.47	0.42	48.4
77	2a, $4f_1$, $4f_2$	0.44	0.22	53.5
	2b	0.42	2.28	42.8
	12k	0.45	0.34	50.7
55	2a, $4f_1$, $4f_2$	0.45	0.22	53.6
	2b	0.43	2.36	43.1
	12k	0.45	0.34	50.8
25	2a, $4f_1$, $4f_2$	0.42	0.24	53.7
	2b	0.43	2.26	42.7
	12k	0.45	0.34	51.8

Table 5 -12 ^{57}Fe Mössbauer parameters recorded from $Sr_{0.95}La_{0.05}Fe_{12}O_{19}$ prepared by the calcination of oxides.

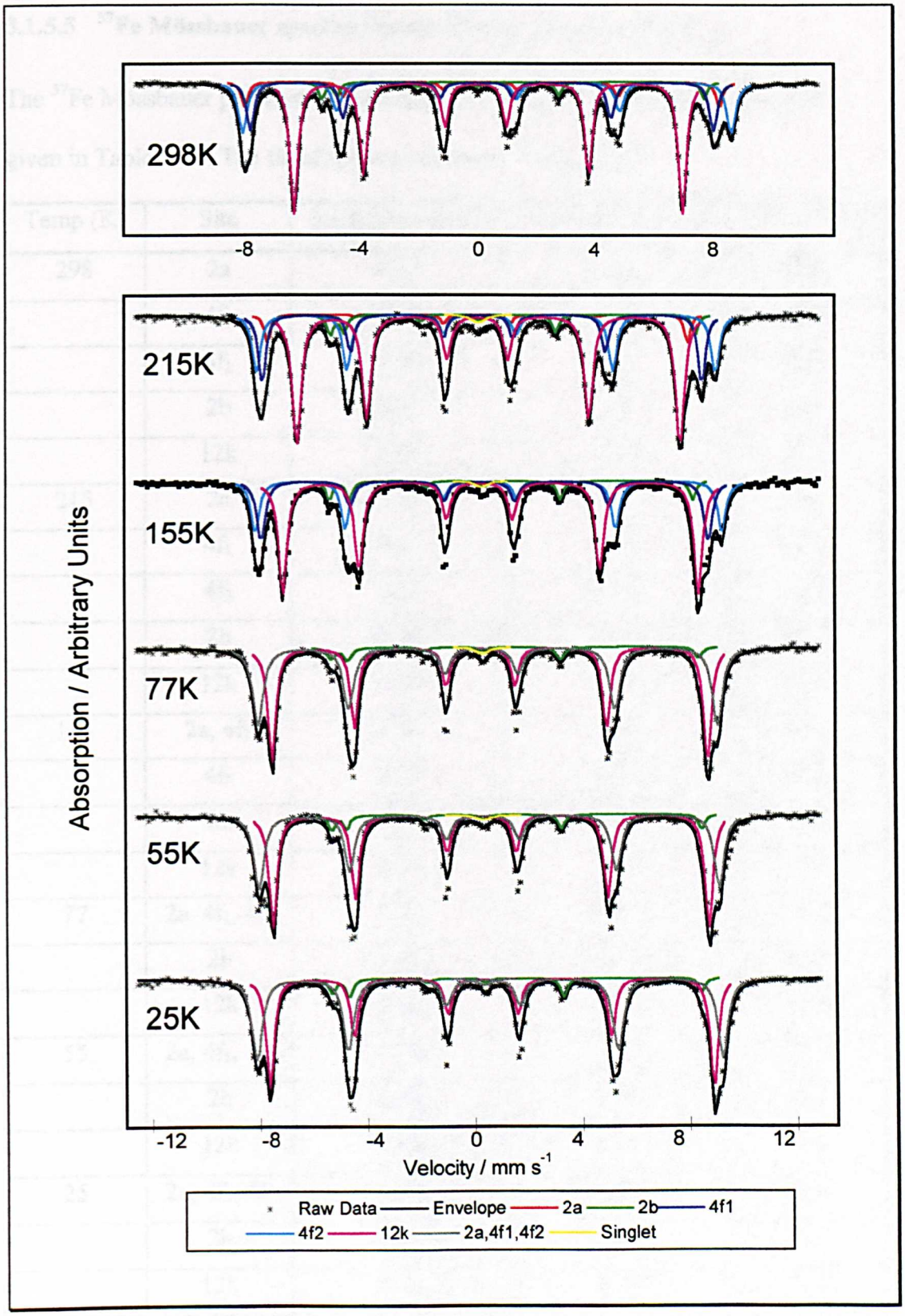

Figure 5-8 ^{57}Fe Mössbauer spectra recorded from $Sr_{0.95}La_{0.05}Fe_{12}O_{19}$ at various temperatures.

5.1.5.5 ^{57}Fe Mössbauer spectra recorded from $Sr_{0.90}La_{0.10}Fe_{12}O_{19}$.

The ^{57}Fe Mössbauer parameters obtained from computer fitting of the spectra are given in Table 5-13. The fitted spectra are shown in Figure 5-9.

Temp (K)	Site	$\delta \pm 0.03$ (mm s^{-1})	$\Delta \pm 0.05$ (mm s^{-1})	H ± 0.5 (T)
298	2a	0.35	0.00	50.6
	$4f_1$	0.27	0.16	49.4
	$4f_2$	0.39	0.30	52.3
	2b	0.31	2.24	41.0
	12k	0.36	0.40	41.7
215	2a	0.23	0.00	48.8
	$4f_1$	0.32	0.14	51.0
	$4f_2$	0.41	0.24	53.1
	2b	0.35	2.36	42.2
	12k	0.39	0.38	45.0
155	2a, $4f_1$	0.44	0.24	54.1
	$4f_2$	0.35	0.14	51.7
	2b	0.33	2.22	42.5
	12k	0.45	0.40	48.7
77	2a, $4f_1$, $4f_2$	0.41	0.18	52.5
	2b	0.41	2.26	42.3
	12k	0.45	0.36	49.4
55	2a, $4f_1$, $4f_2$	0.45	0.22	53.6
	2b	0.43	2.36	43.1
	12k	0.45	0.34	50.8
25	2a, $4f_1$, $4f_2$	0.43	0.24	53.4
	2b	0.41	2.22	42.6
	12k	0.45	0.32	51.0

Table 5 -13 ^{57}Fe Mössbauer parameters recorded from $Sr_{0.90}La_{0.10}Fe_{12}O_{19}$ prepared by the calcination of oxides.

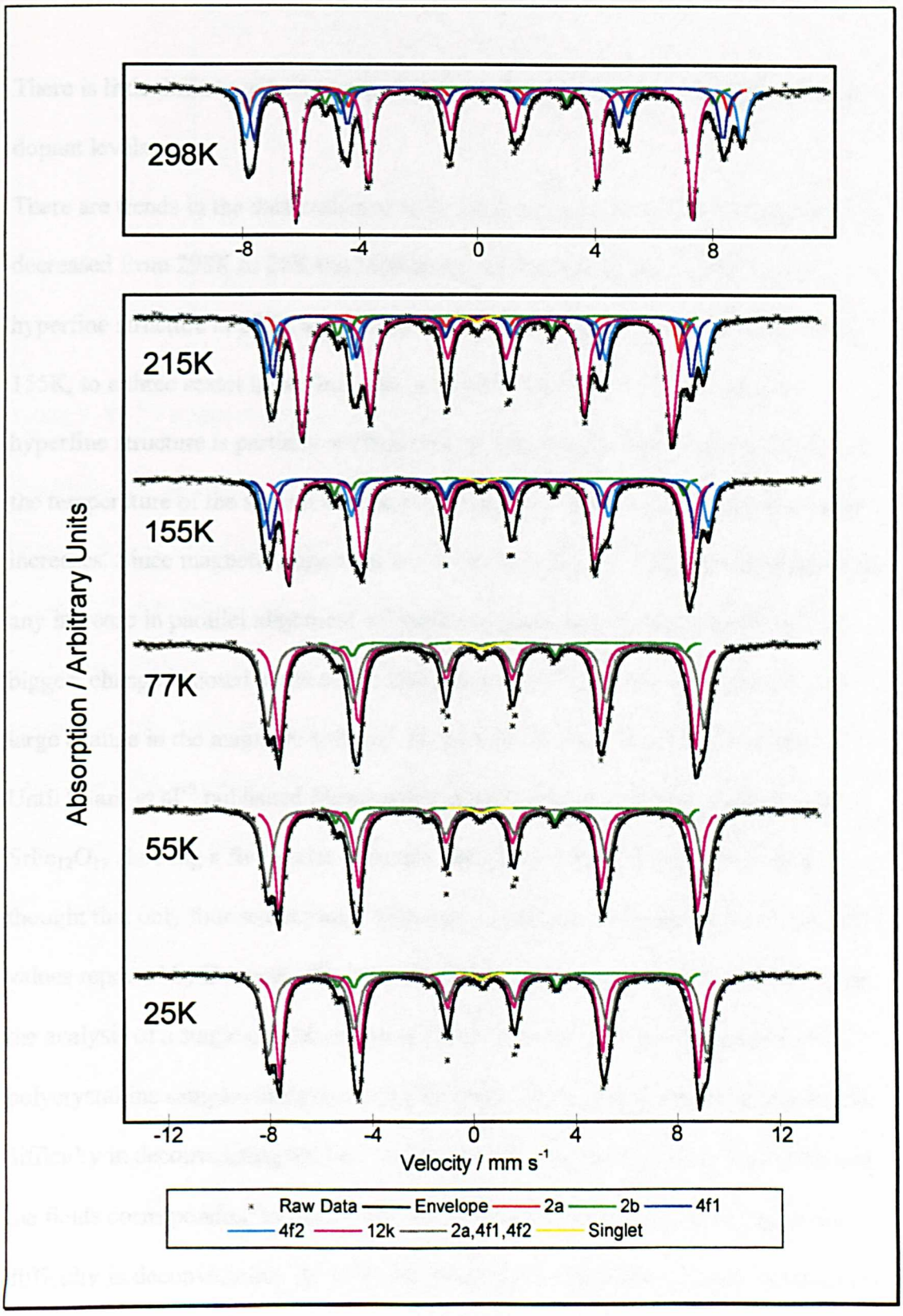

Figure 5-9 ^{57}Fe Mössbauer spectra recorded from $Sr_{0.90}La_{0.10}Fe_{12}O_{19}$ at various temperatures.

There is little difference between the spectra collected from systems with different dopant levels.

There are trends in the data collected at different temperatures. As the temperature is decreased from 298K to 25K the Mössbauer spectra change from a five sextet hyperfine structure at 298K and 215K, through a four sextet hyperfine structure at 155K, to a three sextet hyperfine structure at 77K and below. This change in hyperfine structure is partially attributed to the superposition of magnetic fields. As the temperature of the system is lowered the degree of parallel magnetic alignment increases. Since magnetic alignment is a vector quantity i.e. direction and magnitude, any increase in parallel alignment subsequently increases the magnetic field. The biggest change is noted in the sextet assigned to the 12k Fe site. This site shows a large change in the magnetic splitting, H, from 41.5T at 298K to 50.5T at 25K. Until Evans et al[10] published Mössbauer parameters for high purity single crystal $SrFe_{12}O_{19}$ showing a five sextet structure, and given here in Table 5-14, it was thought that only four sextets were necessary to analyse the spectrum recorded. The values reported by Evans et al[10] showed that the 2a and $4f_2$ sites were similar. Since the analysis of a single crystal can yield clearer data it can be envisaged that the polycrystalline samples analysed here give larger errors and therefore increasing the difficulty in deconvoluting the two sextets. As the sample is lowered in temperature the fields corresponding to the 2a, $4f_1$ and $4f_2$ begin to merge increasing again the difficulty in deconvolution. At 155K the fields have completely merged resulting in a single sextet

Site	δ (mm s^{-1})	Δ (mm s^{-1})	H (Tesla)
2a	0.34	0.18	50.7
2b	0.29	2.27	41.0
$4f_1$	0.26	0.29	49.2
$4f_2$	0.37	0.38	52.0
12k	0.35	0.62	41.6

Table 5 -14 ^{57}Fe Mössbauer parameters reported by Evans et al [10].

The 2b Fe site shows no overall change in observed fields with decreasing temperature. In Chapter 1 it was outlined that the 2b site rather than being one discreet site was two closely situated sites with the Fe atom oscillating between. Such an oscillation, within the lifetime of the Mössbauer effect, results in an average position which does not give a change in magnetic field with decreasing temperature. The observations outlined above are summarised in Figure 5-10 where ^{57}Fe Mössbauer parameters for each subspectra are plotted against temperature in the $SrFe_{12}O_{19}$ system.

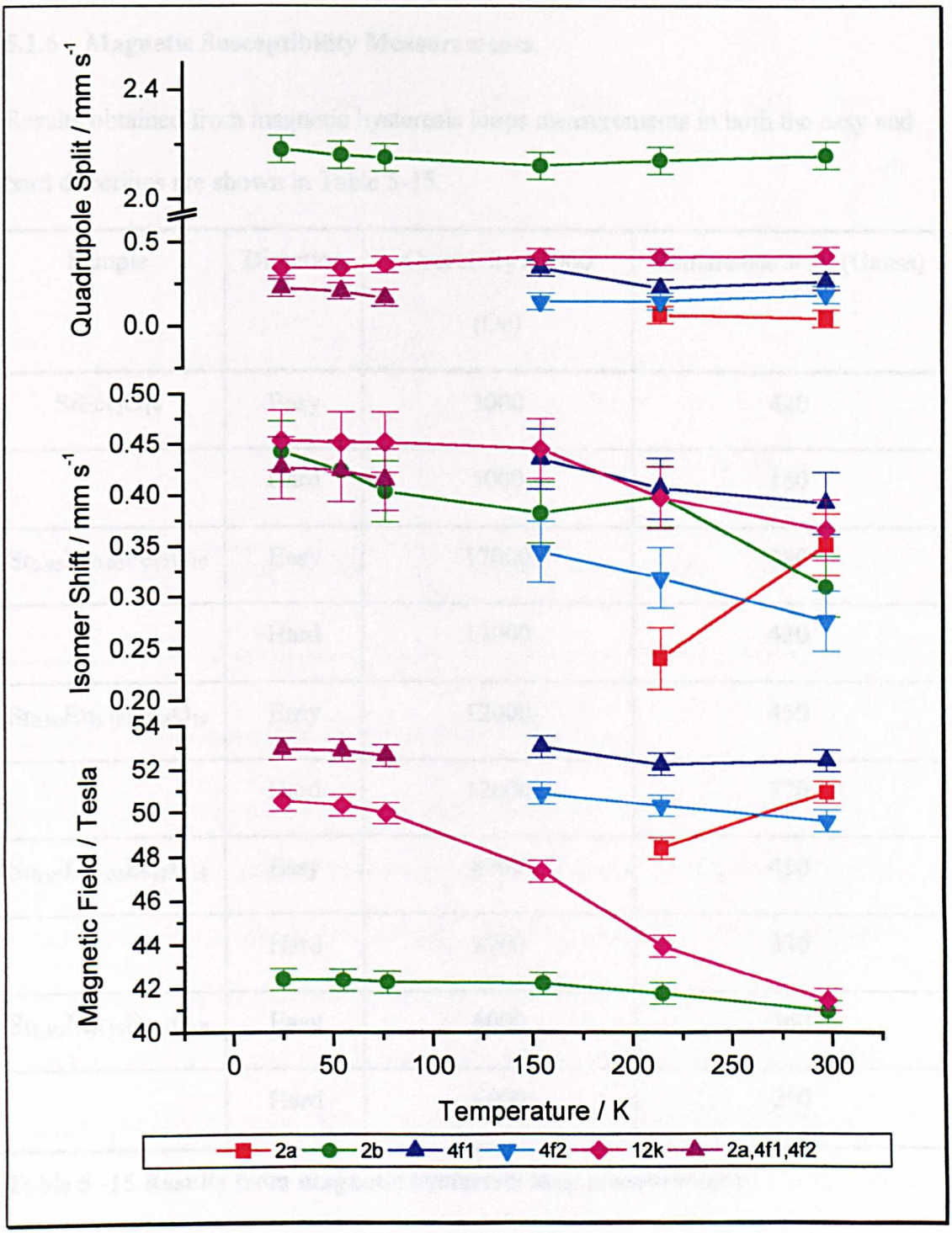

Figure 5-10 Changes in ^{57}Fe Mössbauer parameters with temperature for $SrFe_{12}O_{19}$.

5.1.6 Magnetic Susceptibility Measurements.

Results obtained from magnetic hysteresis loops measurements in both the easy and hard directions are shown in Table 5-15.

Sample	Direction	Coercivity ±1000 (Oe)	Remanence ± 50 (Gauss)
$SrFe_{12}O_{19}$	Easy	3000	420
	Hard	5000	160
$Sr_{0.95}Eu_{0.05}Fe_{12}O_{19}$	Easy	12000	380
	Hard	12000	430
$Sr_{0.90}Eu_{0.10}Fe_{12}O_{19}$	Easy	12000	450
	Hard	12000	370
$Sr_{0.95}La_{0.05}Fe_{12}O_{19}$	Easy	8700	410
	Hard	8700	330
$Sr_{0.90}La_{0.10}Fe_{12}O_{19}$	Easy	6000	360
	Hard	6000	250

Table 5 -15 Results from magnetic hysteresis loop measurements.

An example of a magnetic hysteresis loop measurement is shown in Figure 5-11.

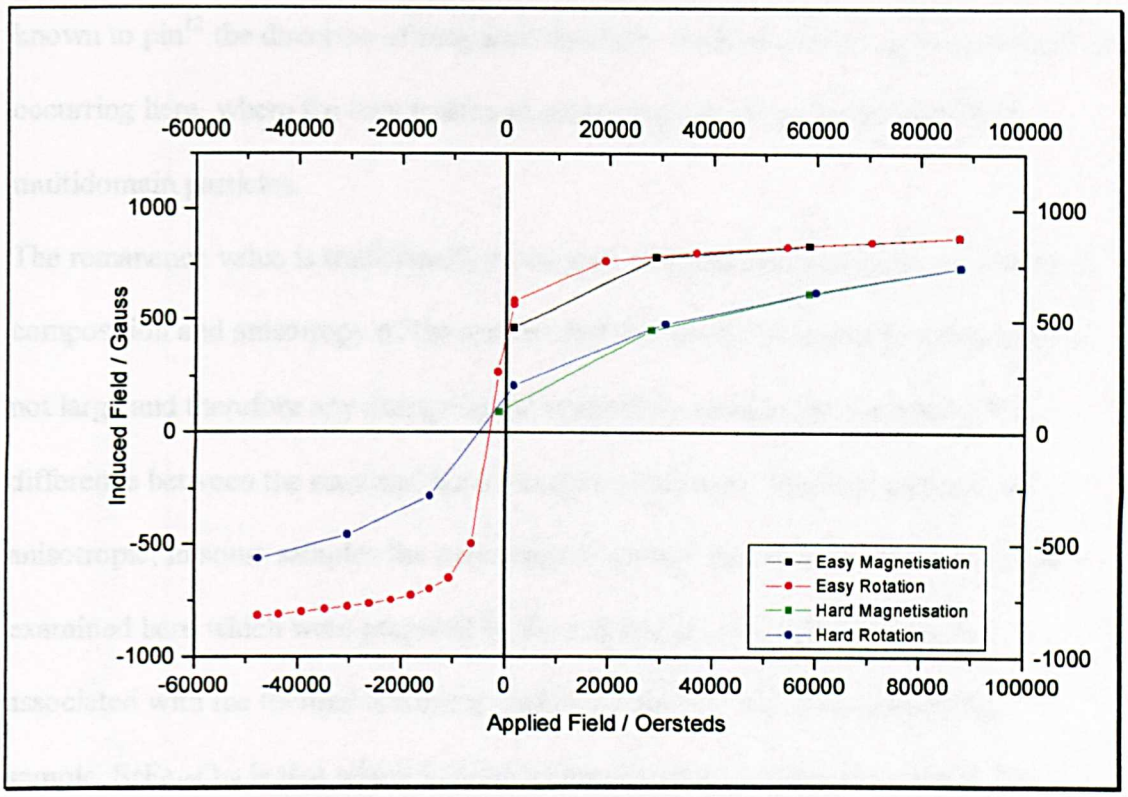

Figure 5-11 Hysteresis loop recorded from $SrFe_{12}O_{19}$.

The data recorded from the hysteresis loop measurements are low in magnitude, when compared with literature values for samples prepared by different methods[11], indicating that the sample is multidomain. This observation is consistent with the particle sizes obtained from the Scherrer method which, with the exception of $SrFe_{12}O_{19}$, showed the particles to exceed the 600 nm single domain particle size. The data recorded from $SrFe_{12}O_{19}$ show a lower coercivity than those recorded from other samples prepared by this method. The heat treatment during formation of these samples has an effect on the magnetic properties of these systems. The heat treatment affects the particle size (Section 5.1.4) and hence the magnetic properties. A second effect of heat treatment on the magnetic properties is through the formation of defects in the crystal structure. The increase in particle size arising from sintering is accompanied by the introduction of defects into the structure. Defects in a crystal are

known to pin[12] the direction of magnetic domains. Such an effect can be envisaged as occurring here, where the heat treatment process gives rise to the formation of multidomain particles.

The remanence value is traditionally envisaged as being determined by the chemical composition and anisotropy of the system. In these systems the amount of dopant is not large and therefore any change in the remanence value would be small. The difference between the *easy* and *hard* directions indicates that these samples are anisotropic, in some samples the anisotropy is greater than in others. In the samples examined here which were prepared by the calcination of oxides this can be associated with the thermal treatment during formation. The most anisotropic sample, $SrFe_{12}O_{19}$ is that which had the minimum amount of heat treatment. This observation agrees with the postulation that the particles formed by the calcination of oxides are in general multidomain[11], with the possible exception of the $SrFe_{12}O_{19}$ system.

5.2 Hexaferrites prepared by the co-precipitation of gels.

5.2.1 X-ray powder diffraction.

The X-ray powder diffraction patterns recorded from samples made by the co-precipitation of gels are shown in Figure 5-12. The patterns show the presence of $SrFe_{12}O_{19}$ or a $SrFe_{12}O_{19}$-related phase. The peaks resulting from the silicon standard used to calibrate the pattern are indicated with arrows.

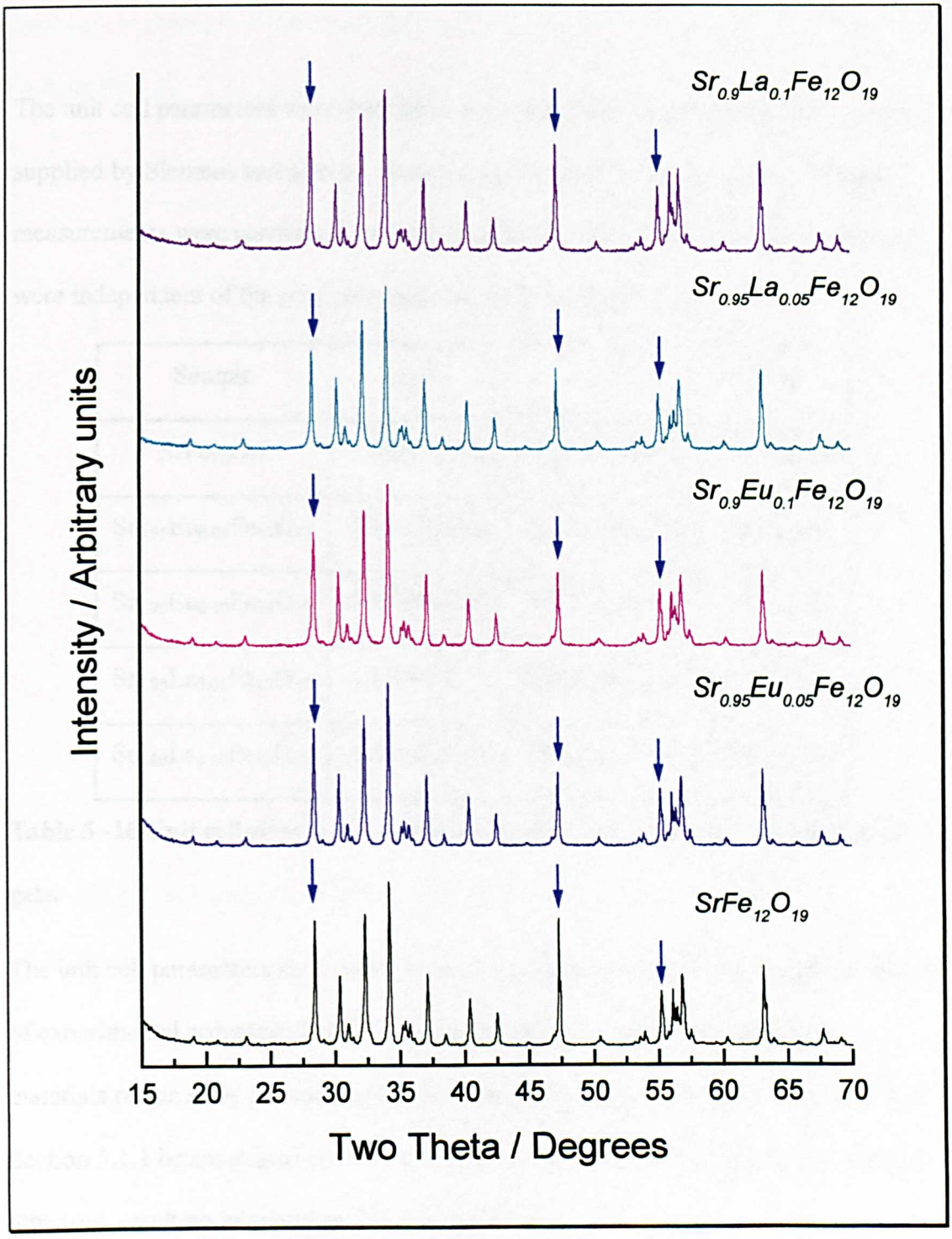

Figure 5-12 X-ray powder diffraction patterns recorded from hexaferrites made by the co-precipitation of gels, the silicon peaks are marked with arrows.

The unit cell parameters were calculated using a standard least squares fitting routine supplied by Siemens and also by using the DICVOL91[1] program. Three different measurements were carried out on each sample. The calculated unit cell parameters were independent of the program used and are presented in Table 5-16.

Sample	a (Å)	c (Å)	Vol (Å^3)
$SrFe_{12}O_{19}$	5.882(0.013)	23.058(0.076)	690.9(5.5)
$Sr_{0.95}Eu_{0.05}Fe_{12}O_{19}$	5.883(0.036)	23.050(0.073)	690.8(5.5)
$Sr_{0.90}Eu_{0.10}Fe_{12}O_{19}$	5.886(0.038)	23.051(0.069)	691.6(5.3)
$Sr_{0.95}La_{0.05}Fe_{12}O_{19}$	5.870(0.013)	23.047(0.200)	690.7(5.2)
$Sr_{0.90}La_{0.10}Fe_{12}O_{19}$	5.885(0.013)	23.053(0.075)	691.4(5.4)

Table 5 -16 Unit cell sizes for hexaferrites formed from the co-precipitation of gels.

The unit cell parameters show there is no overall change in cell size, within the limits of experimental accuracy. They are similar to those recorded from analogous materials prepared by the calcination of oxides (Table 5-1). This can, as explained in Section 5.1.1 be associated with the changes in ionic radii which tend to cancel each other out, resulting in no overall change in volume.

5.2.2 X-ray Absorption Fine Structure (XAFS).

Fe K-edge XAFS measurements were performed on the non-europium containing samples i.e. $SrFe_{12}O_{19}$, $Sr_{0.95}La_{0.05}Fe_{12}O_{19}$, and $Sr_{0.90}La_{0.10}Fe_{12}O_{19}$ an example of a

spectrum is shown in Figure 5-13, the results obtained from these samples are shown in Appendix II.

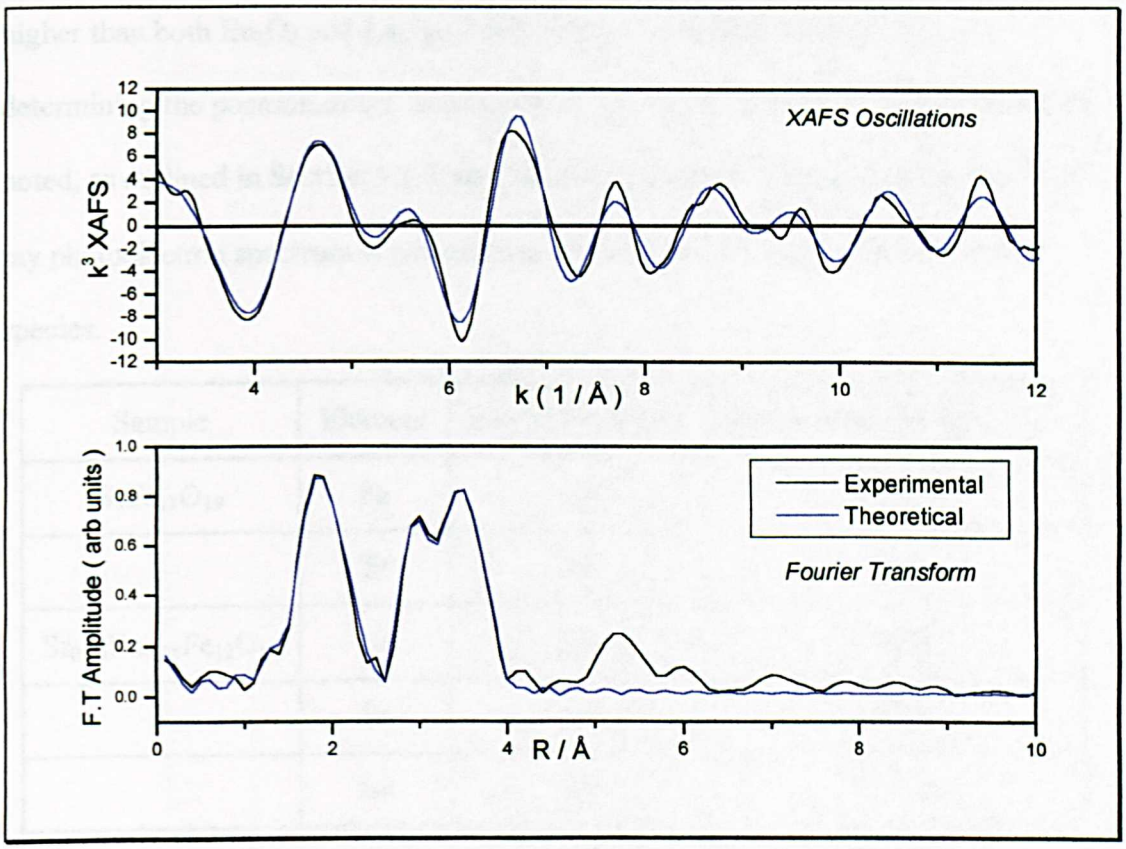

Figure 5-13 Fe K-edge XAFS data recorded from $SrFe_{12}O_{19}$ prepared by the co-precipitation of gels.

The data are very similar to those obtained from samples prepared by the calcination of oxides. This is not unexpected since XAFS is a technique that studies local structure around an atom and the materials prepared by the two methods were shown by X-ray powder diffraction to be structurally identical.

5.2.3 X-ray photoelectron spectroscopy.

Data obtained from computer analysis of the X-ray photoelectron spectra are shown in Table 5-17. The spectrum of $SrFe_{12}O_{19}$ prepared by the co-precipitation of a gel is shown in Figure 5-14.

The XPS spectra were similar to those recorded from samples prepared by the calcination of oxides. However, the binding energies of the rare earth elements are higher than both Eu_2O_2 and La_2O_3 (Table 5-7), as a result of the difficulty in determining the position of the broad peak as explained in Section 5.1.3. It should be noted, as outlined in Section 5.1.3, that the absence of a Fe^{2+} component in the Fe X-ray photoelectron spectrum is not necessarily indicative of the absence of such a species.

Sample	Element	Electronic Level	Binding Energy ±0.1 (eV)
$SrFe_{12}O_{19}$	Fe	2p	710.0
	Sr	3d	133.1
$Sr_{0.95}Eu_{0.05}Fe_{12}O_{19}$	Fe	2p	709.8
	Sr	3d	132.6
	Eu	4f	1133.4
$Sr_{0.90}Eu_{0.10}Fe_{12}O_{19}$	Fe	2p	710.0
	Sr	3d	132.8
	Eu	4f	1133.3
$Sr_{0.95}La_{0.05}Fe_{12}O_{19}$	Fe	2p	710.1
	Sr	3d	133.0
	La	4f	833.7
$Sr_{0.90}La_{0.10}Fe_{12}O_{19}$	Fe	2p	710.0
	Sr	3d	132.9
	La	4f	833.5

Table 5 -17 Binding energies recorded by X-ray photoelectron spectroscopy.

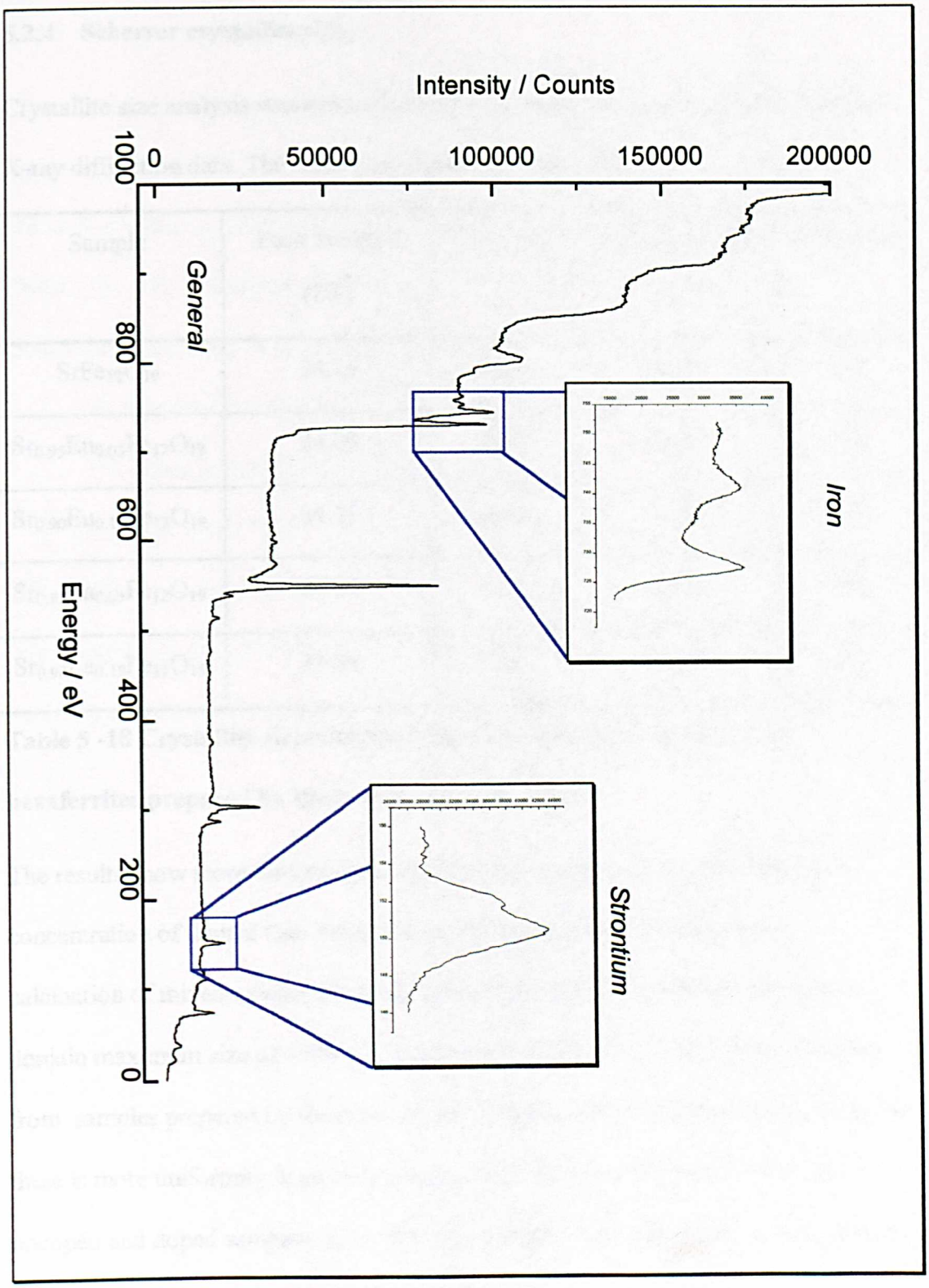

Figure 5-14 XPS spectrum recorded from $SrFe_{12}O_{19}$ prepared by the co-precipitation of a gel.

5.2.4 Scherrer crystallite size

Crystallite size analysis was carried out using the Scherrer equation on the recorded X-ray diffraction data. The results are shown in Table 5-18.

Sample	Peak Position ($2\theta^{\circ}$)	Size / nm	Peak Position ($2\theta^{\circ}$)	Size / nm
$SrFe_{12}O_{19}$	34.18	620	32.32	580
$Sr_{0.95}Eu_{0.05}Fe_{12}O_{19}$	34.20	690	32.34	640
$Sr_{0.90}Eu_{0.10}Fe_{12}O_{19}$	34.21	600	32.38	560
$Sr_{0.95}La_{0.05}Fe_{12}O_{19}$	34.24	510	32.40	480
$Sr_{0.90}La_{0.10}Fe_{12}O_{19}$	34.16	630	32.30	550

Table 5 -18 Crystallite sizes obtained from the Scherrer equation from hexaferrites prepared by the co-precipitation of gels.

The results show more uniformity in size and less dependence on the nature and concentration of dopant than those obtained from samples prepared by the calcination of mixed oxides. The particle sizes are close to the theoretical single domain maximum size of ~600 nm. Comparison of the results with those obtained from samples prepared by the calcination of oxides shows that across a dopant series there is more uniformity in particle size i.e. there is little difference between the undoped and doped samples. This reflects the similar heat treatments of each sample i.e. they were all heated at 925°C for 2 hours.

5.2.5 Mössbauer Spectroscopy.

The ^{57}Fe Mössbauer parameters for the samples $SrFe_{12}O_{19}$ and $Sr_{0.95}Eu_{0.05}Fe_{12}O_{19}$ collected at 25K, 55K, 77K, 155K, 181K, and 298K are shown in Table 5-19 and Table 5-20. Due to time limitations the three other samples were only measured at 298K. The ^{57}Fe Mössbauer parameters are shown in Tables 5-23 - 5-25. Identical constraints were used in the fitting of the spectra:

(i) Standard Lorentzian lines.

(ii) Equal width of peaks in the sextet.

(iii) The area of the outer lines being three times the area of the inner lines.

The middle lines were allowed to fit freely.

The assignment of sextet patterns to crystallographic sites in the structure was based upon the same procedure as that used in Section 5.1.5.

5.2.5.1 Spectra recorded from $SrFe_{12}O_{19}$.

The ^{57}Fe Mössbauer parameters obtained from computer fitting of the spectra are shown in Table 5-19. The spectra are shown in Figure 5-15.

Temp	Site	$\delta \pm 0.03$ (mm s^{-1})	$\Delta \pm 0.05$ (mm s^{-1})	$H \pm 0.5$ (T)
298	2a	0.30	0.00	51.2
	2b	0.30	2.26	41.0
	$4f_1$	0.27	0.16	49.2
	$4f_2$	0.40	0.30	52.0
	12k	0.36	0.42	41.5
185	2a $4f_1$	0.31	0.12	50.5
	$4f_2$	0.42	0.16	53.0
	2b	0.31	2.26	42.5
	12k	0.19	0.41	46.4
155	2a, $4f_1$	0.35	0.14	50.7
	$4f_2$	0.43	0.20	53.2
	2b	0.36	2.16	43.6
	12k	0.43	0.34	48.1
77	2a, $4f_1$, $4f_2$	0.42	0.20	53.4
	2b	0.36	2.16	42.6
	12k	0.44	0.32	50.6
55	2a, $4f_1$, $4f_2$	0.42	0.22	53.3
	2b	0.36	2.14	42.6
	12k	0.45	0.32	51.0
25	2a, $4f_1$, $4f_2$	0.43	0.22	53.4
	2b	0.38	2.20	42.8
	12k	0.45	0.30	51.1

Table 5 -19 - ^{57}Fe Mössbauer parameters collected from $SrFe_{12}O_{19}$ prepared by gel co-precipitation.

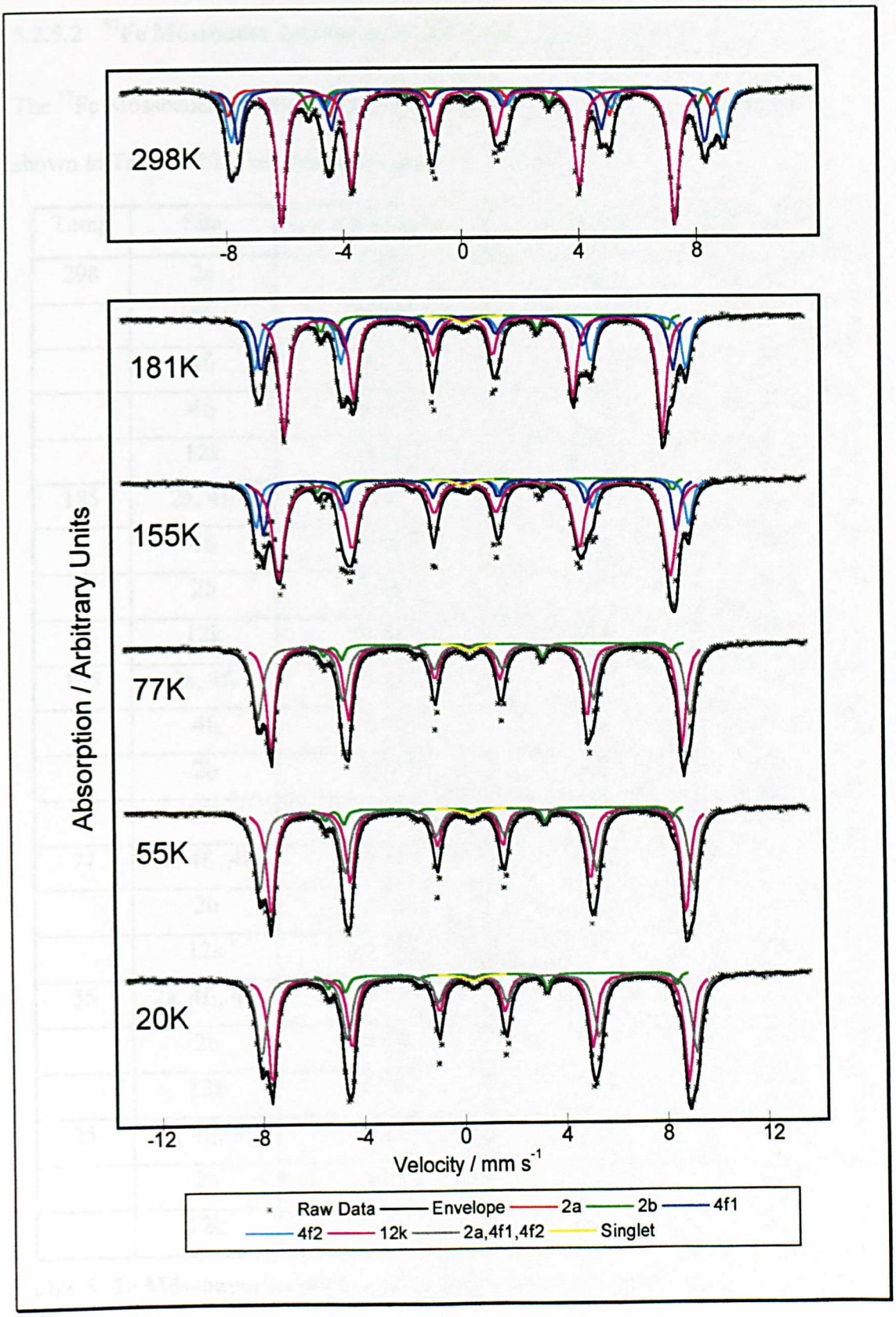

Figure 5-15 ^{57}Fe Mössbauer spectra recorded from $SrFe_{12}O_{19}$ prepared by the co-precipitation of a gel.

5.2.5.2 ^{57}Fe Mössbauer spectra recorded from $Sr_{0.95}Eu_{0.05}Fe_{12}O_{19}$.

The ^{57}Fe Mössbauer parameters obtained from computer fitting of the spectra are shown in Table 5-20. The spectra are shown in Figure 5-16.

Temp	Site	$\delta \pm 0.03$ (mm s^{-1})	$\Delta \pm 0.05$ (mm s^{-1})	H ± 0.5 (T)
298	2a	0.29	0.00	51.0
	2b	0.30	2.24	40.9
	$4f_1$	0.27	0.16	49.1
	$4f_2$	0.41	0.32	51.9
	12k	0.36	0.42	41.4
185	2a, $4f_1$	0.31	0.12	50.6
	$4f_2$	0.42	0.16	53.0
	2b	0.31	2.26	42.5
	12k	0.41	0.38	46.4
155	2a, $4f_1$	0.33	0.14	50.8
	$4f_2$	0.42	0.18	53.2
	2b	0.38	2.30	43.0
	12k	0.42	0.38	47.5
77	2a, $4f_1$, $4f_2$	0.42	0.20	53.0
	2b	0.36	2.16	42.6
	12k	0.44	0.32	50.5
55	2a, $4f_1$, $4f_2$	0.43	0.22	53.2
	2b	0.37	2.12	42.5
	12k	0.44	0.32	50.9
25	2a, $4f_1$, $4f_2$	0.43	0.24	53.3
	2b	0.38	2.18	42.7
	12k	0.44	0.32	51.0

Table 5 -20 Mössbauer hyperfine parameters obtained from $Sr_{0.95}Eu_{0.05}Fe_{12}O_{19}$ prepared by co-precipitation of a gel.

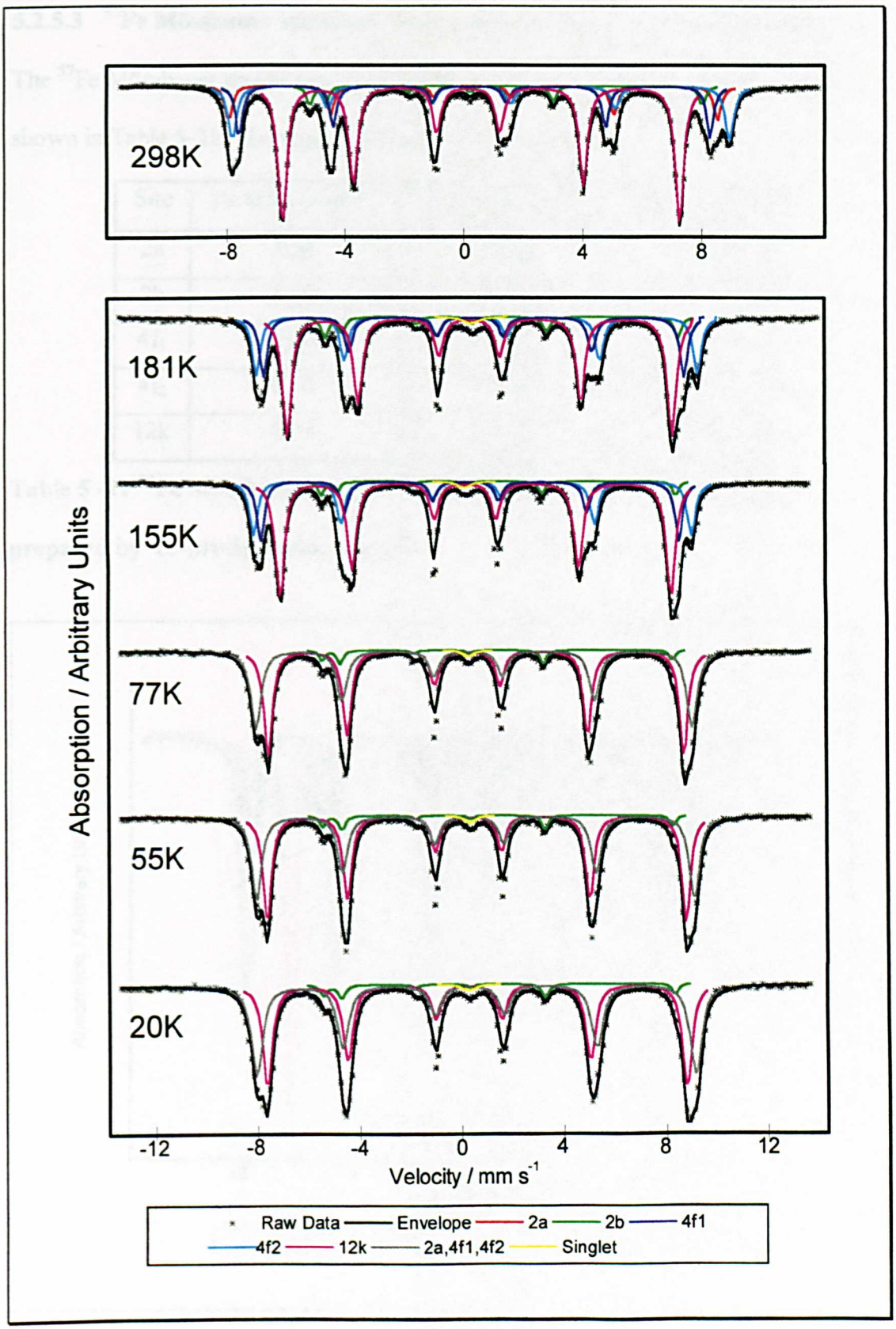

Figure 5-16 ^{57}Fe Mössbauer spectra recorded from $Sr_{0.95}Eu_{0.05}Fe_{12}O_{19}$ at various temperatures.

5.2.5.3 ^{57}Fe Mössbauer spectrum recorded from $Sr_{0.9}Eu_{0.1}Fe_{12}O_{19}$ at 298K.

The ^{57}Fe Mössbauer parameters obtained from computer fitting of the spectra are shown in Table 5-21. The spectrum is shown in Figure 5-17.

Site	$\delta \pm 0.03$ (mm s^{-1})	$\Delta \pm 0.05$ (mm s^{-1})	H ± 0.5 (T)
2a	0.31	0.00	51.3
2b	0.29	2.26	41.1
$4f_1$	0.28	0.18	49.2
$4f_2$	0.40	0.34	52.0
12k	0.36	0.40	41.6

Table 5 -21 ^{57}Fe Mössbauer parameters recorded from $Sr_{0.9}Eu_{0.1}Fe_{12}O_{19}$ prepared by co-precipitation of a gel.

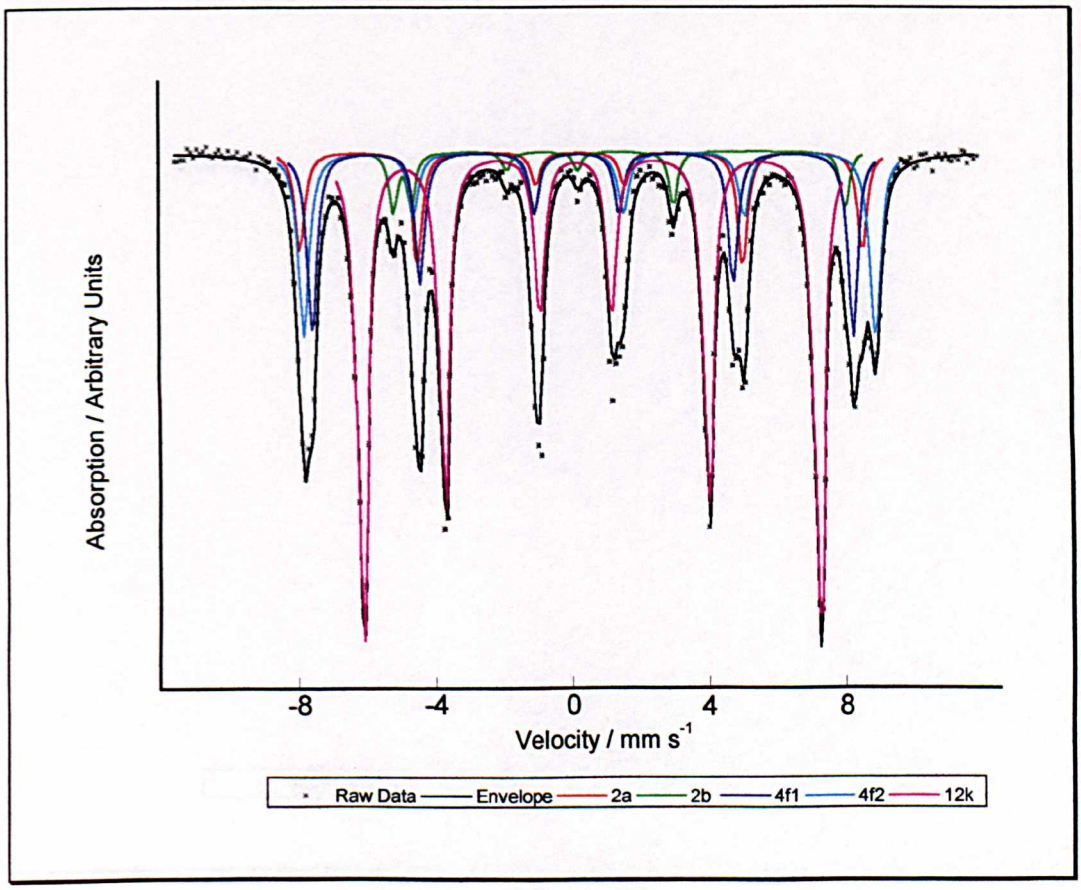

Figure 5-17 ^{57}Fe Mössbauer spectrum recorded from $Sr_{0.9}Eu_{0.1}Fe_{12}O_{19}$ at 298K.

5.2.5.4 ^{57}Fe Mössbauer spectrum recorded from $Sr_{0.95}La_{0.05}Fe_{12}O_{19}$.

The ^{57}Fe Mössbauer parameters obtained from computer fitting of the spectra are shown in Table 5-22. The spectrum is shown in Figure 5-18.

Site	$\delta \pm 0.03$ (mm s^{-1})	$\Delta \pm 0.05$ (mm s^{-1})	H ± 0.5 (T)
2a	0.31	0.06	51.3
2b	0.30	2.26	41.2
$4f_1$	0.28	0.18	49.3
$4f_2$	0.41	0.32	52.0
12k	0.36	0.40	41.6

Table 5 -22 ^{57}Fe Mössbauer parameters obtained from $Sr_{0.95}La_{0.05}Fe_{12}O_{19}$ prepared by co-precipitation of a gel.

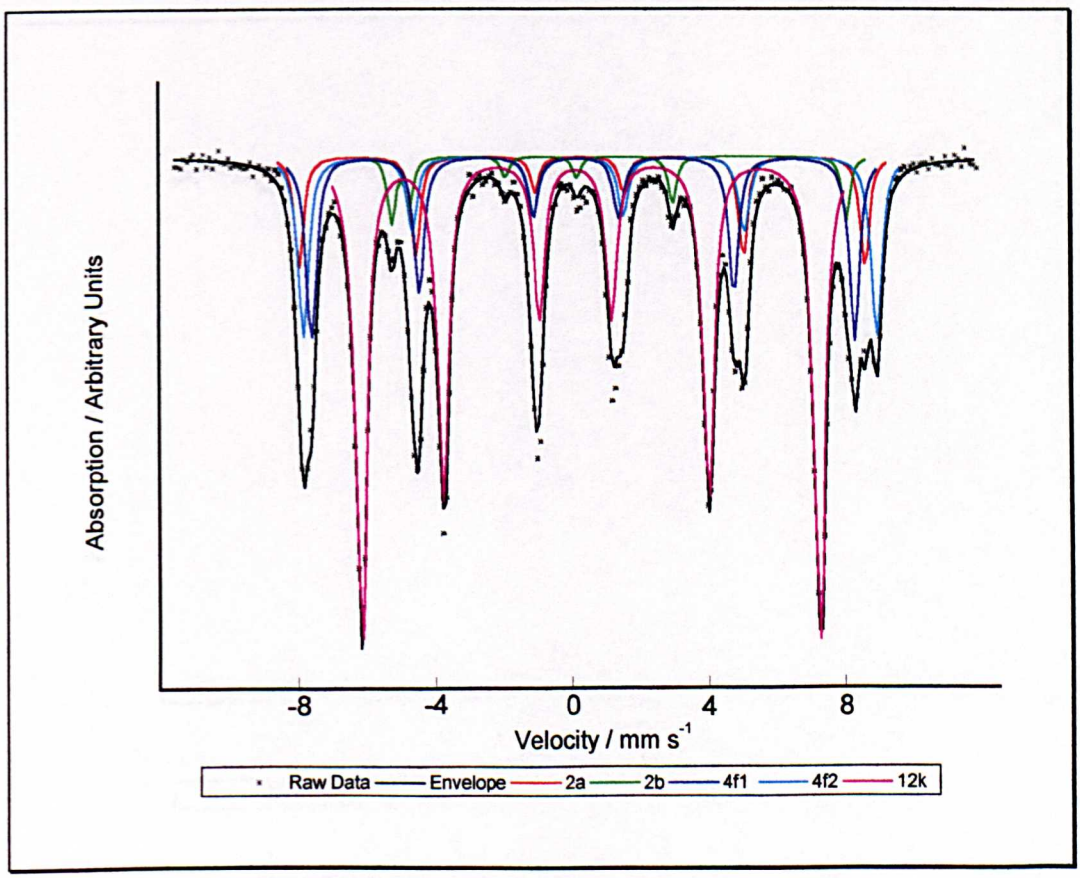

Figure 5-18 ^{57}Fe Mössbauer spectrum recorded from $Sr_{0.95}La_{0.05}Fe_{12}O_{19}$ at 298K.

5.2.5.5 ^{57}Fe Mössbauer spectrum recorded from $Sr_{0.90}La_{0.10}Fe_{12}O_{19}$.

The ^{57}Fe Mössbauer parameters obtained from computer fitting of the spectra are shown in Table 5-23. The spectrum is shown in Figure 5-19.

Site	$\delta \pm 0.03$ (mm s^{-1})	$\Delta \pm 0.05$ (mm s^{-1})	H ± 0.5 (T)
2a	0.32	0.00	51.3
2b	0.28	2.22	41.3
$4f_1$	0.27	0.18	49.4
$4f_2$	0.40	0.34	52.2
12k	0.36	0.40	41.7

Table 5 -23 ^{57}Fe Mössbauer parameters obtained from $Sr_{0.90}La_{0.10}Fe_{12}O_{19}$ prepared by co-precipitation of a gel.

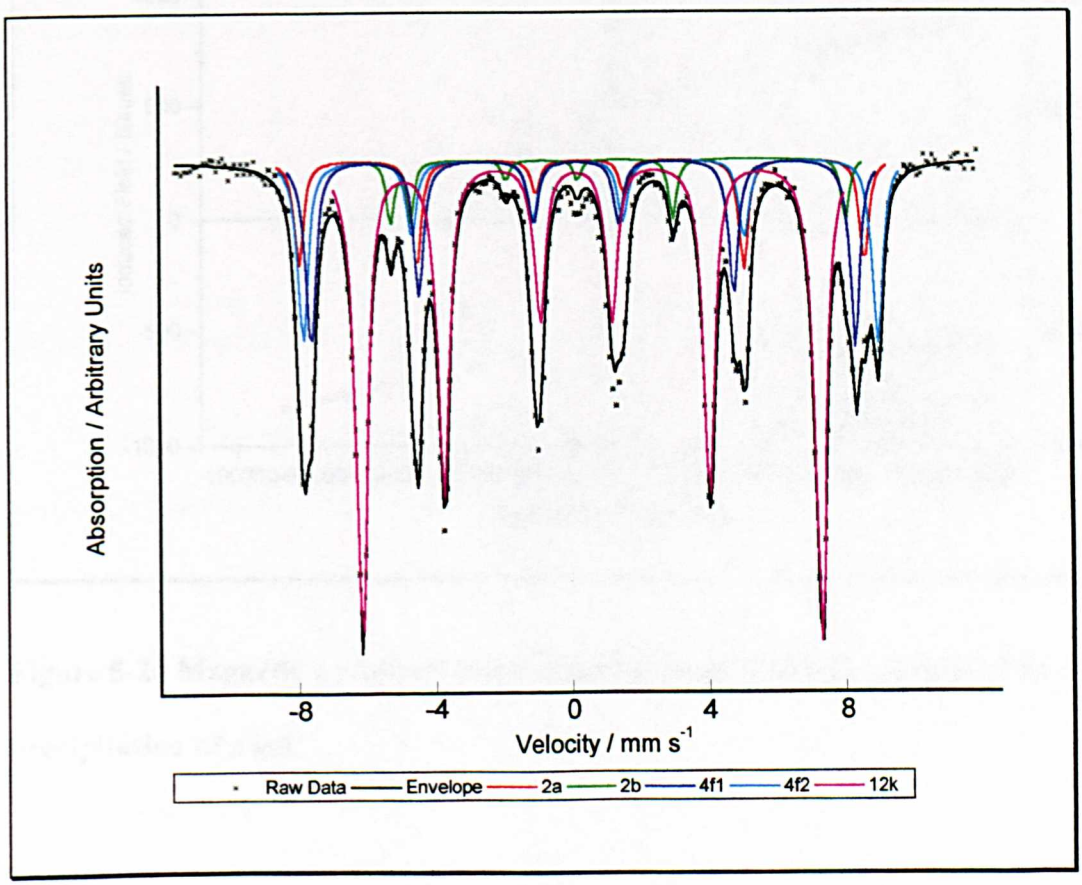

Figure 5-19 ^{57}Fe Mössbauer spectrum recorded from $Sr_{0.90}La_{0.10}Fe_{12}O_{19}$ at 298K.

The data collected from these samples are broadly in agreement with those collected from samples prepared by the calcination of oxides and can be interpreted in a similar fashion.

5.2.6 Magnetic Susceptibility Measurements.

The results obtained from the analysis of magnetic hysteresis loop measurements carried out in both the easy and hard directions are contained in Table 5-24. An example of a magnetic hysteresis loop is shown in Figure 5-20.

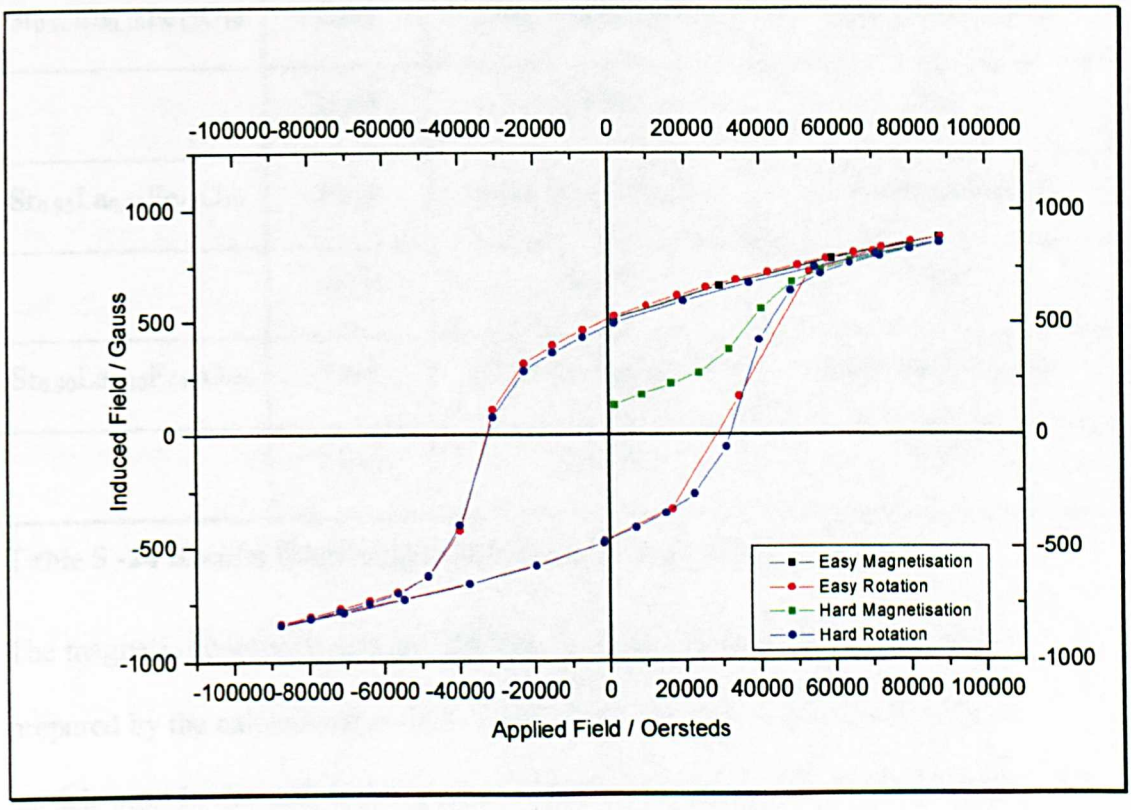

Figure 5-20 Magnetic hysteresis loops recorded from $SrFe_{12}O_{19}$ prepared by co-precipitation of a gel.

Sample	Direction	Coercivity ±1000 (Oe)	Remanence ± 50 (Gauss)
$SrFe_{12}O_{19}$	Easy	33000	510
	Hard	33000	470
$Sr_{0.95}Eu_{0.05}Fe_{12}O_{19}$	Easy	29000	495
	Hard	29000	450
$Sr_{0.90}Eu_{0.10}Fe_{12}O_{19}$	Easy	Data Inconclusive	Data Inconclusive
	Hard	30000	500
$Sr_{0.95}La_{0.05}Fe_{12}O_{19}$	Easy	Data Inconclusive	Data Inconclusive
	Hard	30000	460
$Sr_{0.90}La_{0.10}Fe_{12}O_{19}$	Easy	Data Inconclusive	Data Inconclusive
	Hard	28000	480

Table 5 -24 Results from magnetic hysteresis loop measurements.

The magnetic coercivity data are different from those recorded from samples prepared by the calcination of oxides (Section 5.1.6), this is due principally to particle size. In the samples prepared by the calcination of oxides, the particles exceeded that of a single magnetic domain. As outlined in Section 5.1.6 this resulted in the magnetic coercivity being relatively low. In materials prepared by the co-precipitation of a gel, Scherrer analysis of the X-ray powder diffraction data suggests that the particle sizes are around the single domain limit. The relatively large size of the magnetic domain requires a larger magnetic field to rotate and reduce the induced

magnetic field to zero. The explanation of this observation is outlined in Chapter 1, Section 1.2.4.

The values for magnetic remanence are similar to those recorded from samples prepared by the calcination of oxides of similar composition. The agreement stems from the remanence tending to be determined by chemical composition, as outlined in Section 5.1.6.

5.3 Hexaferrites prepared by hydrothermal processing of metal nitrates.

5.3.1 X-ray powder diffraction.

The X-ray powder diffraction patterns recorded from samples prepared by the hydrothermal processing of metal salts are shown in Figure 5-21. The patterns show the presence of $SrFe_{12}O_{19}$ or a $SrFe_{12}O_{19}$-related phase. The peaks resulting from the silicon standard used to calibrate the peak positions are indicated with arrows.

5.3.1.1 Lattice Parameters.

The unit cell parameters were calculated using a standard least squares fitting routine supplied by Siemens and also by using the DICVOL91[1] program. Three different measurements were carried out on each sample. The calculated unit cell parameters were independent of the program used and are presented in Table 5-25.

Sample	a (Å)	c (Å)	Vol (Å^3)
$SrFe_{12}O_{19}$	5.884(0.015)	23.092(0.085)	692.4(6.0)
$Sr_{0.95}Eu_{0.05}Fe_{12}O_{19}$	5.884(0.027)	23.075(0.188)	691.8(13.4)
$Sr_{0.90}Eu_{0.10}Fe_{12}O_{19}$	5.879(0.039)	23.086(0.249)	692.6(16.7)
$Sr_{0.95}La_{0.05}Fe_{12}O_{19}$	5.880(0.024)	23.076(0.124)	691.1(9.2)
$Sr_{0.90}La_{0.10}Fe_{12}O_{19}$	5.882(0.016)	23.082(0.106)	691.5(7.0)

Table 5 -25 - Unit cell sizes for hexaferrites formed from the hydrothermal processing of metal nitrates.

The data presented in Table 5-25 show no overall variation, within the limits of experimental accuracy, in the unit cell parameters obtained from the different samples. This observation agrees with the results obtained for identical samples prepared by the other two techniques.

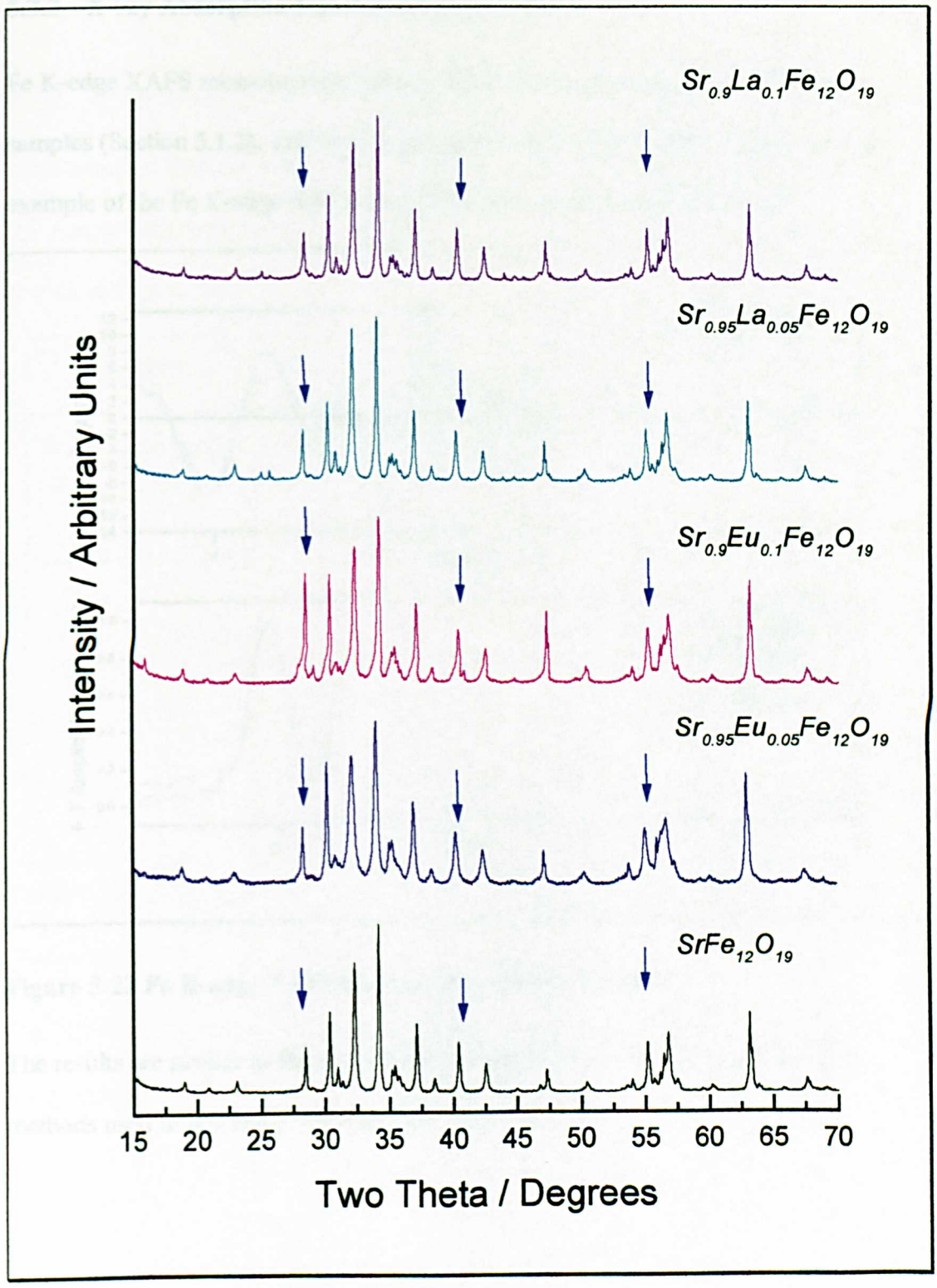

Figure 5-21 X-ray powder diffraction patterns recorded from hexaferrites made by the hydrothermal processing of metal nitrates, the silicon peaks are marked with arrows.

5.3.2 X-ray Absorption Fine Structure (XAFS).

Fe K-edge XAFS measurements were performed on non-europium containing samples (Section 5.1.2). The best-fit parameters are shown in Appendix III, and an example of the Fe K-edge XAFS from $SrFe_{12}O_{19}$ is shown in Figure 5-22.

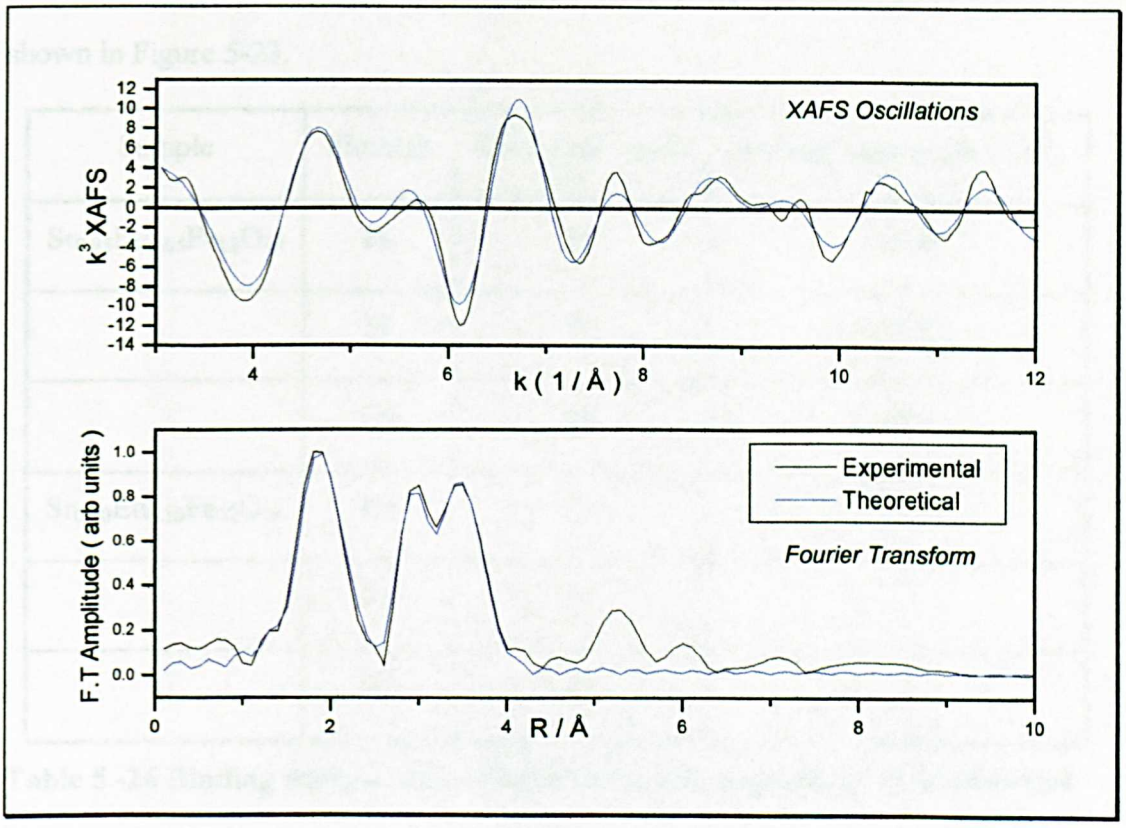

Figure 5-22 Fe K-edge XAFS data recorded from $SrFe_{12}O_{19}$.

The results are similar to those obtained from samples prepared by the other two methods used in this study and discussed in Section 5.2.2.

5.3.3 X-ray photoelectron spectroscopy.

Data obtained from the computer analysis of the X-ray spectra are shown in Table 5-26. A spectrum recorded from $Sr_{0.95}Eu_{0.05}Fe_{12}O_{19}$ prepared by this technique is shown in Figure 5-23.

Sample	Element	Electronic Level	Binding Energy ±0.1 (eV)
$Sr_{0.95}Eu_{0.05}Fe_{12}O_{19}$	Fe	2p	709.8
	Sr	3d	133.2
	Eu	4f	1132.5
$Sr_{0.90}Eu_{0.10}Fe_{12}O_{19}$	Fe	2p	711.9
	Sr	3d	
	Eu	4f	1133.5

Table 5 -26 Binding energies recorded for samples prepared by hydrothermal processing.

The XPS data recorded from these samples are similar to those recorded from samples prepared by the co-precipitation of a gel and the calcination of oxides.

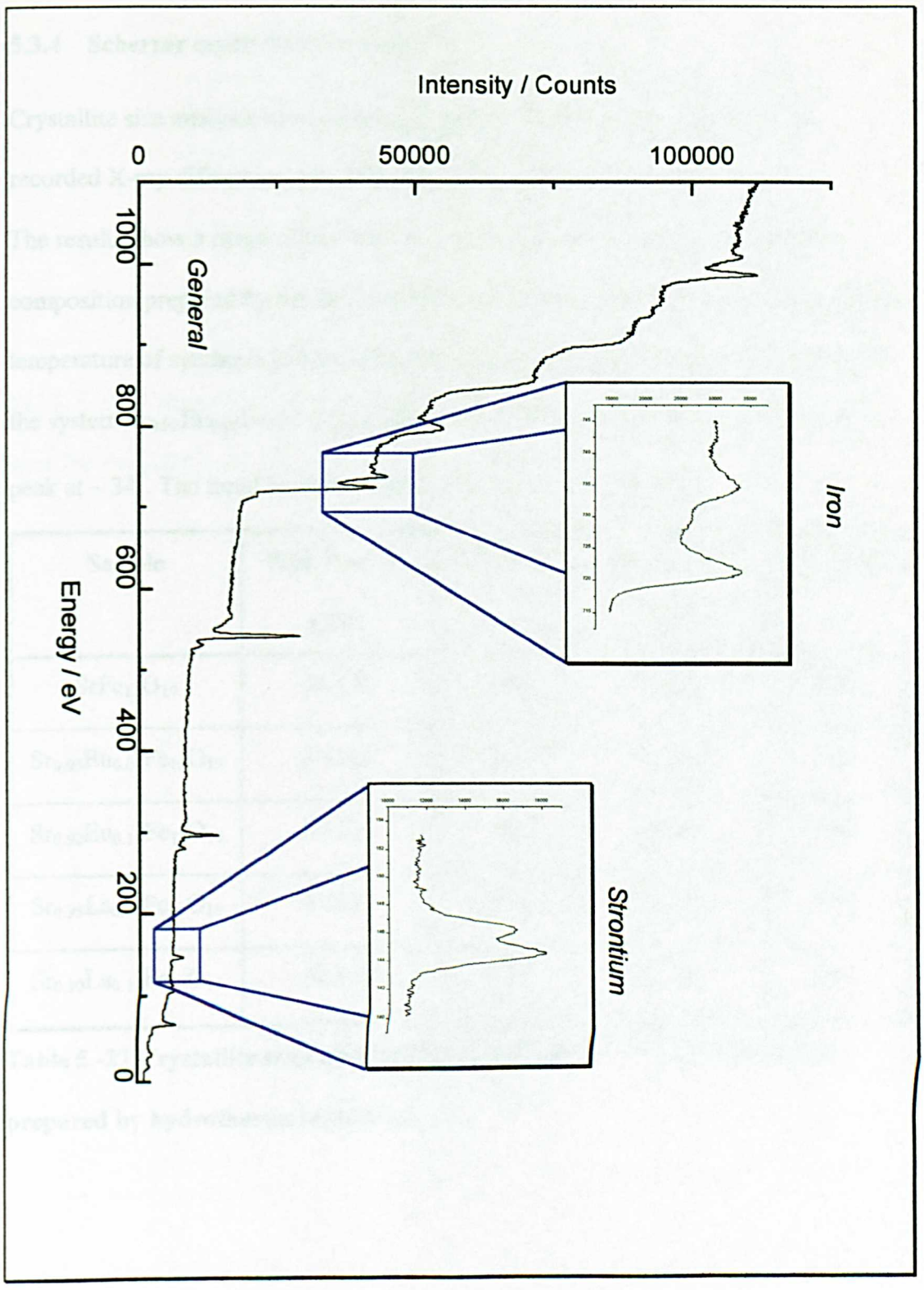

Figure 5-23 X-ray photoelectron spectrum recorded from $Sr_{0.95}Eu_{0.05}Fe_{12}O_{19}$ prepared by the hydrothermal processing of metal nitrates.

5.3.4 Scherrer crystallite size analysis.

Crystallite size analysis was carried out applying the Scherrer equation to the recorded X-ray diffraction data. The results are shown in Table 5-27.

The results show a range of particle sizes. When the particle sizes of a specific composition prepared by the three methods are compared, a trend can be seen. As the temperature of synthesis is decreased the particle size also decreases. An example is the system $Sr_{0.95}Eu_{0.05}Fe_{12}O_{19}$ for which the results are shown in Table 5-28 for the peak at ~ 34°. The trend in peak width is illustrated in Figure 5-24.

Sample	Peak Position (2θ°)	Size (nm)	Peak Position (2θ°)	Size (nm)
$SrFe_{12}O_{19}$	34.173	560	32.299	400
$Sr_{0.95}Eu_{0.05}Fe_{12}O_{19}$	34.136	280	32.246	200
$Sr_{0.90}Eu_{0.10}Fe_{12}O_{19}$	34.121	380	32.243	280
$Sr_{0.95}La_{0.05}Fe_{12}O_{19}$	34.154	470	32.277	350
$Sr_{0.90}La_{0.10}Fe_{12}O_{19}$	34.163	550	32.282	430

Table 5 -27 Crystallite sizes obtained by the Scherrer method for samples prepared by hydrothermal synthesis.

Method of Preparation	Particle Size (nm)
Calcination of oxides	~800
Co-precipitation of gel	~600
Hydrothermal Processing	~280

Table 5 -28 Comparison of results from Scherrer analysis of X-ray diffraction data for $Sr_{0.95}Eu_{0.05}Fe_{12}O_{19}$.

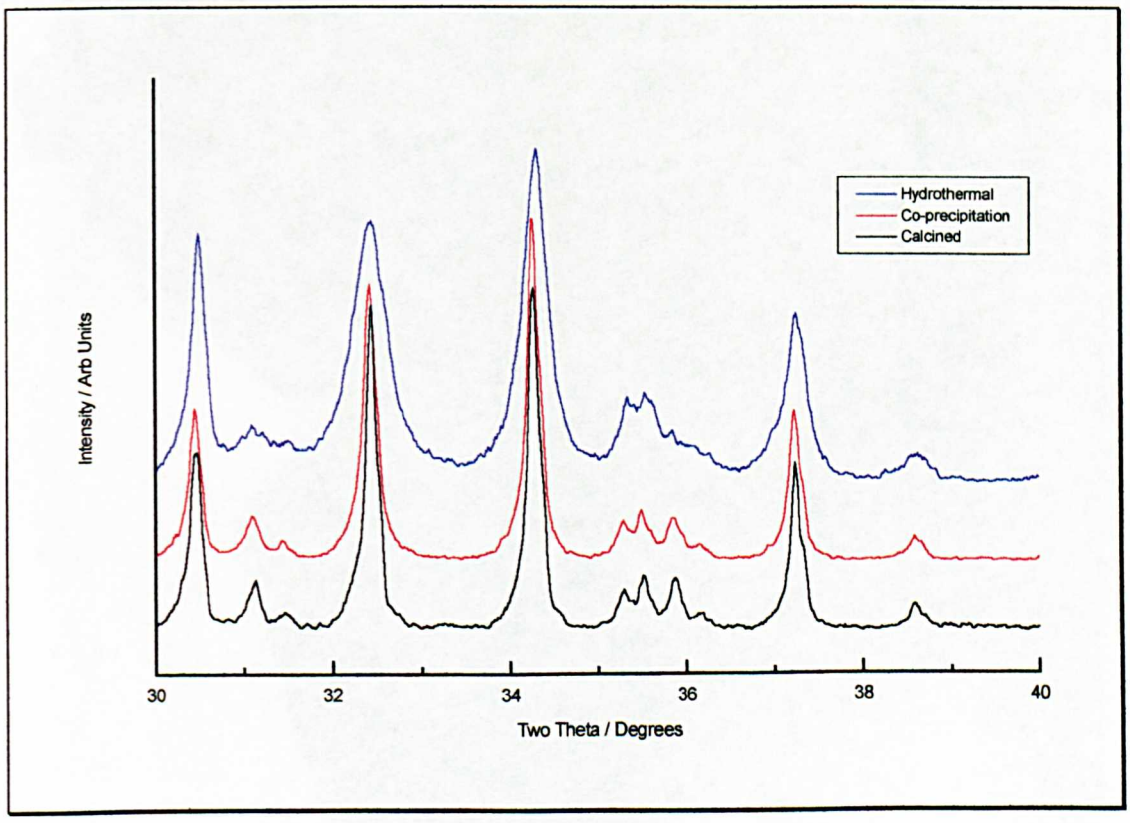

Figure 5-24 X-ray powder patterns from $SrFe_{12}O_{19}$ illustrating the changes in peak width with decreasing temperature of synthesis.

TEM measurements on samples made by this method indicated that the particles were flat hexagonal plates, as illustrated in Figure 5-25, which gave single crystal electron diffraction patterns as shown in Figure 5-26.

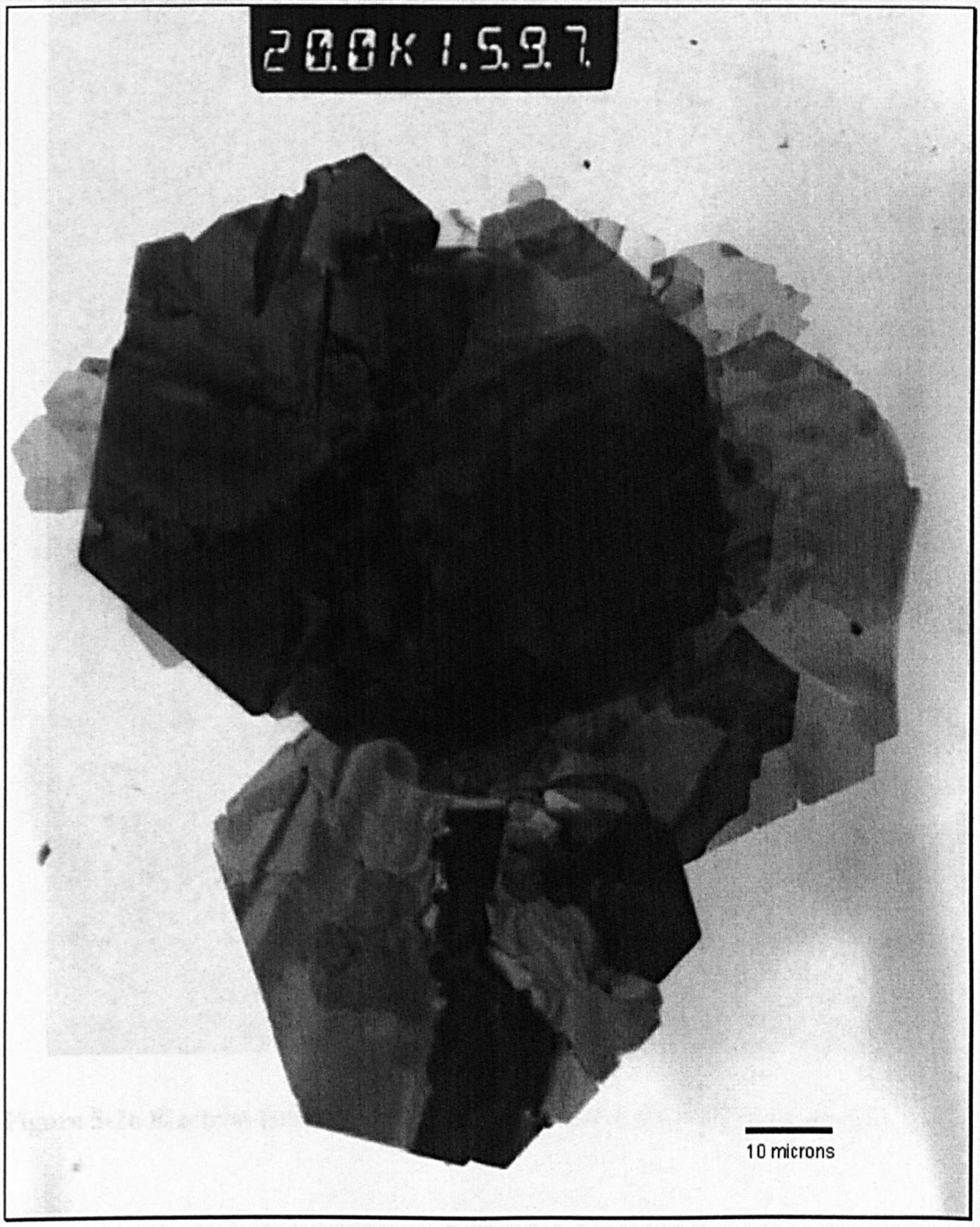

Figure 5-25 Transmission electron micrograph recorded from $Sr_{0.95}La_{0.05}Fe_{12}O_{19}$, at a magnification of 20,000.

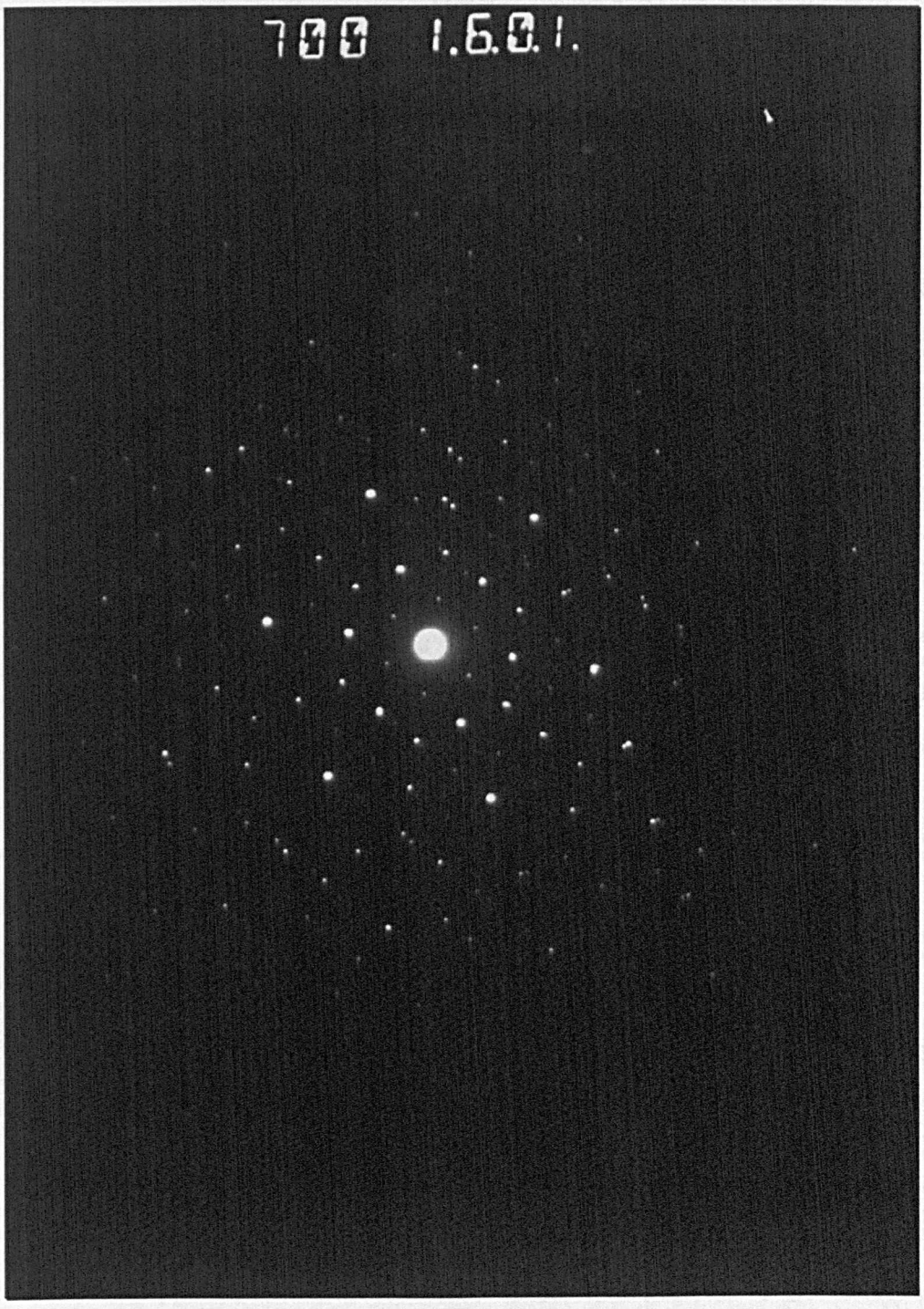

Figure 5-26 Electron Diffraction pattern recorded from $Sr_{0.95}La_{0.05}Fe_{12}O_{19}$.

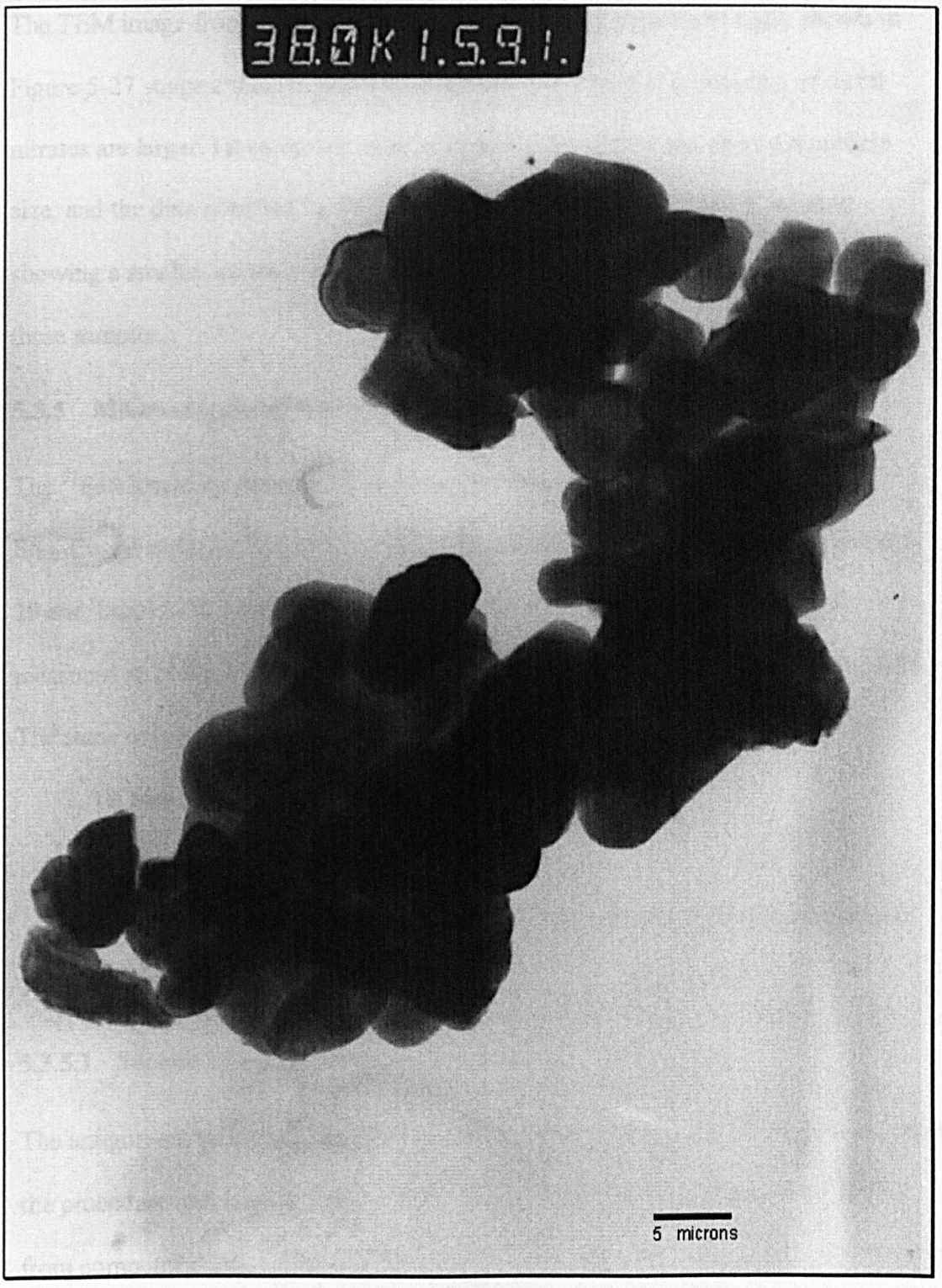

Figure 5-27 Transmission electron micrograph recorded from $SrFe_{12}O_{19}$ prepared by the co-precipitation of a gel, at a magnification of 38,000.

The TEM image from a sample prepared by the co-precipitation of a gel, shown in Figure 5-27 suggest that the particles made the hydrothermal processing of metal nitrates are larger. However the wide hexagonal plates skew the observed particle size, and the data obtained by the Scherrer analysis of the recorded X-ray data showing a smaller average volume, is a more reliable measurement of particle size in these samples.

5.3.5 Mössbauer Spectroscopy.

The ^{57}Fe Mössbauer parameters recorded from the samples $SrFe_{12}O_{19}$ and $Sr_{0.95}Eu_{0.05}Fe_{12}O_{19}$ at 25K, 55K, 77K, 155K, 181K, and 298K are shown in Table 5-29 and Table 5-30. Due to time limitations the three other samples were only measured at 298K. The ^{57}Fe Mössbauer parameters are shown in Tables 5-33 - 5-35. The same constraints were used in the fitting of the spectra:

(i) Standard Lorentzian lines.

(ii) Equal width of peaks in the sextet.

(iii) The area of the outer lines being three times the area of the inner lines.

The middle lines were allowed to fit freely.

5.3.5.1 Spectra recorded from $SrFe_{12}O_{19}$.

The assignment of subspectra with Fe sites in the $SrFe_{12}O_{19}$ structure was based upon the procedure specified in Section 5.1.5. The ^{57}Fe Mössbauer parameters obtained from computer fitting of the spectra are shown in Table 5-29. The spectra are shown in Figure 5-28.

Temp	Site	$\delta \pm 0.03$ (mm s^{-1})	$\Delta \pm 0.05$ (mm s^{-1})	H ± 0.5 (T)
298	2a	0.33	0.28	49.4
	2b	0.22	2.00	40.4
	$4f_1$	0.28	0.20	47.7
	$4f_2$	0.39	0.24	50.8
	12k	0.35	0.38	41.1
185	2a, $4f_1$	0.33	0.12	49.9
	$4f_2$	0.42	0.22	52.7
	2b	0.48	2.34	43.7
	12k	0.42	0.36	46.5
155	2a, $4f_1$	0.35	0.14	50.8
	$4f_2$	0.43	0.18	53.2
	2b	0.36	2.16	43.6
	12k	0.43	0.34	48.1
77	2a, $4f_1$, $4f_2$	0.43	0.22	53.0
	2b	0.33 0.39	2.02 1.80	42.9 44.4
	12k	0.45	0.28	50.7
55	2a, $4f_1$, $4f_2$	0.44	0.24	53.1
	2b	0.36 0.41	2.12 1.94	42.6 44.1
	12k	0.45	0.28	51.0
25	2a, $4f_1$, $4f_2$	0.45	0.24	53.3
	2b	0.41 0.45	2.16 1.88	43.1 44.5
	12k	0.45	0.26	51.3

Table 5 -29 - ^{57}Fe Mössbauer parameters collected from $SrFe_{12}O_{19}$ prepared by hydrothermal processing of metal nitrates.

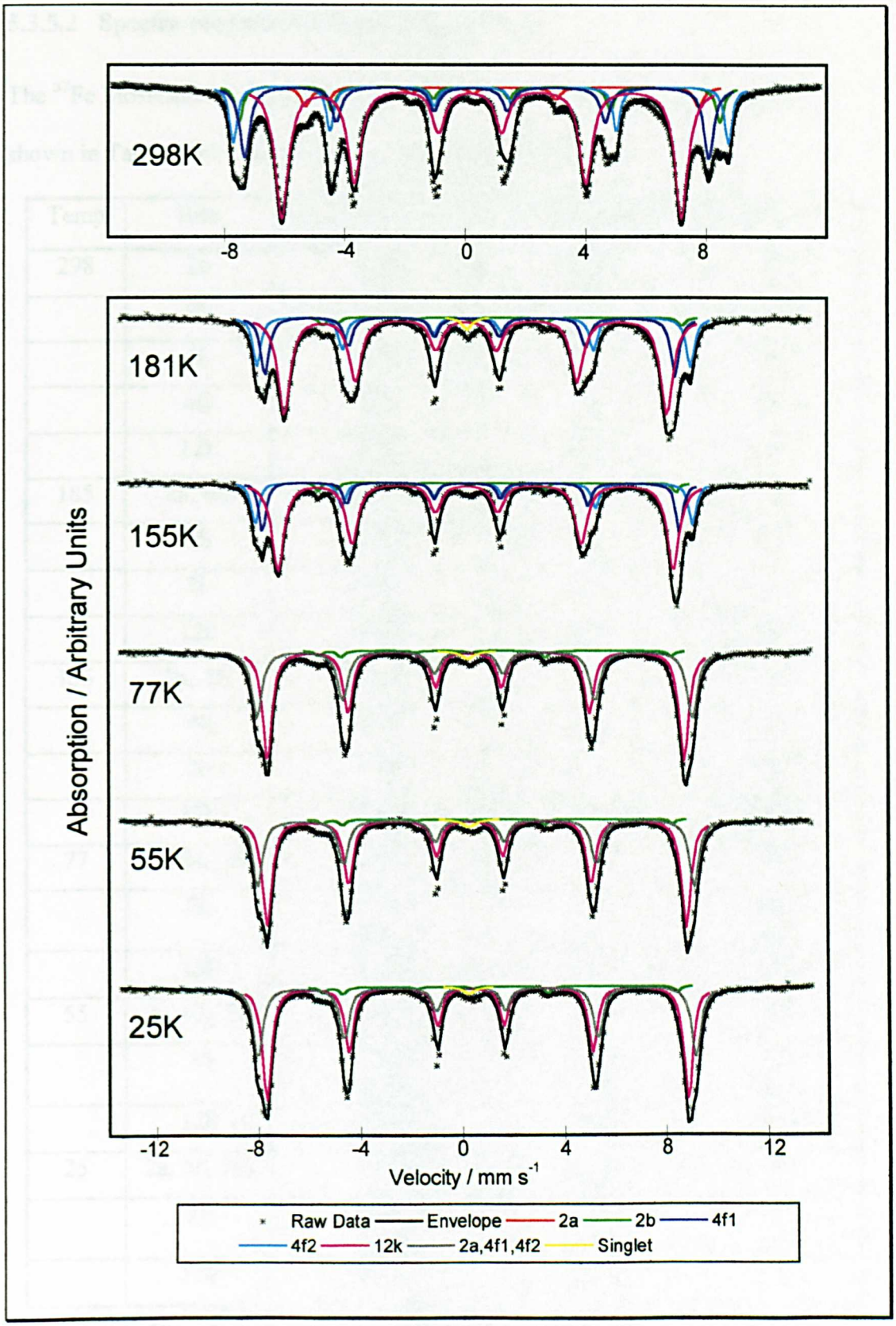

Figure 5-28 ^{57}Fe Mössbauer spectra collected from $SrFe_{12}O_{19}$ prepared by the hydrothermal processing of metal nitrates.

5.3.5.2 Spectra recorded from $Sr_{0.95}Eu_{0.05}Fe_{12}O_{19}$.

The ^{57}Fe Mössbauer parameters obtained from computer fitting of the spectra are shown in Table 5-30. The spectra are shown in Figure 5-29.

Temp	Site	$\delta \pm 0.03$ (mm s^{-1})	$\Delta \pm 0.05$ (mm s^{-1})	$H \pm 0.5$ (T)
298	2a	0.32	0.28	49.1
	2b	0.21	1.94	40.2
	$4f_1$	0.28	0.20	47.3
	$4f_2$	0.38	0.24	50.6
	12k	0.35	0.38	41.1
185	2a, $4f_1$	0.34	0.16	49.7
	$4f_2$	0.42	0.20	52.3
	2b	0.35	2.32	42.9
	12k	0.42	0.36	46.6
155	2a, $4f_1$	0.35	0.18	50.2
	$4f_2$	0.42	0.16	52.6
	2b	0.38	2.18	43.2
	12k	0.42	0.34	47.6
77	2a, $4f_1$, $4f_2$	0.44	0.24	52.8
	2b	0.34 0.31	1.96 1.76	43.0 44.3
	12k	0.45	0.28	50.8
55	2a, $4f_1$, $4f_2$	0.45	0.26	53.0
	2b	0.40 0.39	2.14 1.85	43.0 44.3
	12k	0.45	0.26	51.0
25	2a, $4f_1$, $4f_2$	0.45	0.26	53.2
	2b	0.44 0.40	2.04 1.98	43.5 44.3
	12k	0.45	0.26	51.3

Table 5 -30 - ^{57}Fe Mössbauer parameters collected from $Sr_{0.95}Eu_{0.05}Fe_{12}O_{19}$ prepared by hydrothermal processing of metal nitrates.

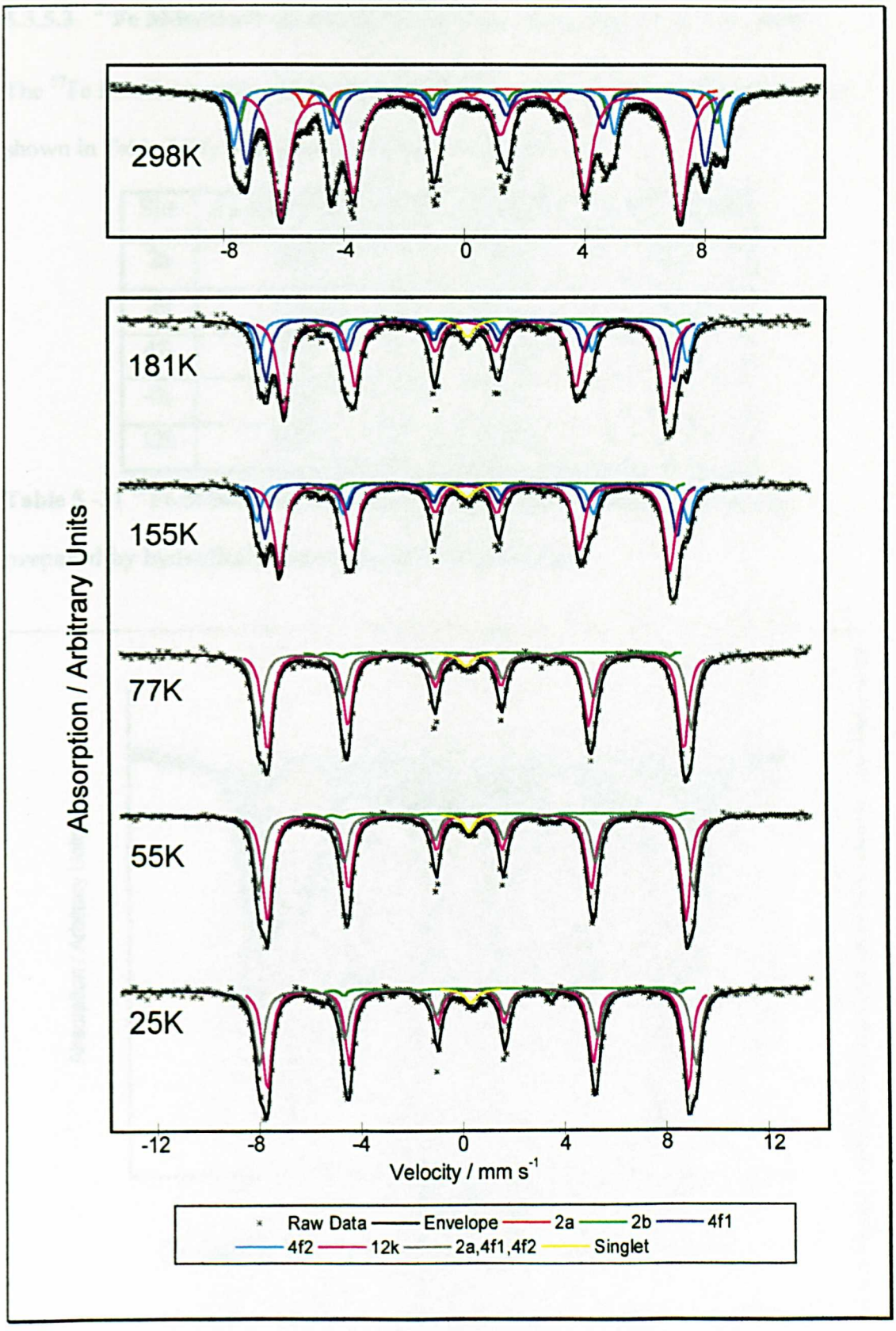

Figure 5-29 ^{57}Fe Mössbauer spectra collected from $Sr_{0.95}Eu_{0.05}Fe_{12}O_{19}$ prepared by the hydrothermal processing of metal nitrates.

5.3.5.3 ^{57}Fe Mössbauer spectrum recorded from $Sr_{0.9}Eu_{0.1}Fe_{12}O_{19}$ at 298K.

The ^{57}Fe Mössbauer parameters obtained from computer fitting of the spectrum are shown in Table 5-31. The spectrum is shown in Figure 5-30.

Site	$\delta \pm 0.03$ (mm s^{-1})	$\Delta \pm 0.05$ (mm s^{-1})	H ± 0.5 (T)
2a	0.33	0.28	49.3
2b	0.21	1.96	40.4
$4f_1$	0.29	0.20	47.4
$4f_2$	0.38	0.24	50.8
12k	0.35	0.38	41.2

Table 5 -31 ^{57}Fe Mössbauer parameters collected from $Sr_{0.90}Eu_{0.10}Fe_{12}O_{19}$ prepared by hydrothermal processing of metal nitrates.

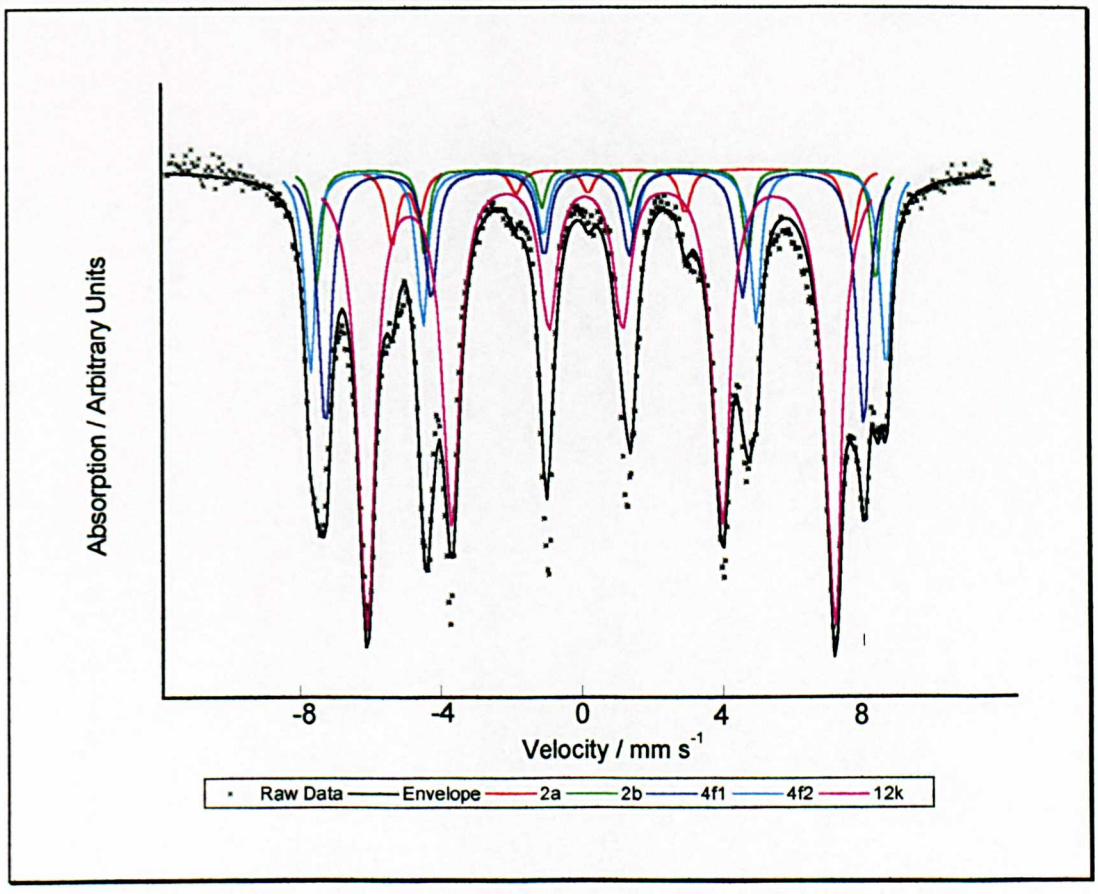

Figure 5-30 ^{57}Fe Mössbauer spectrum collected at 298K from $Sr_{0.9}Eu_{0.1}Fe_{12}O_{19}$ prepared by the hydrothermal processing of metal nitrates.

5.3.5.4 ^{57}Fe Mössbauer spectrum recorded from $Sr_{0.95}La_{0.05}Fe_{12}O_{19}$ at 298K.

The ^{57}Fe Mössbauer parameters obtained from computer fitting of the spectrum is shown in Table 5-32. The spectrum is shown in Figure 5-31.

Site	$\delta \pm 0.03$ (mm s^{-1})	$\Delta \pm 0.05$ (mm s^{-1})	H ± 0.5 (T)
2a	0.33	0.30	49.3
2b	0.25	1.92	40.3
$4f_1$	0.29	0.18	47.5
$4f_2$	0.39	0.26	50.8
12k	0.35	0.36	41.1

Table 5 -32 ^{57}Fe Mössbauer parameters collected from $Sr_{0.95}La_{0.05}Fe_{12}O_{19}$ prepared by hydrothermal processing of metal nitrates.

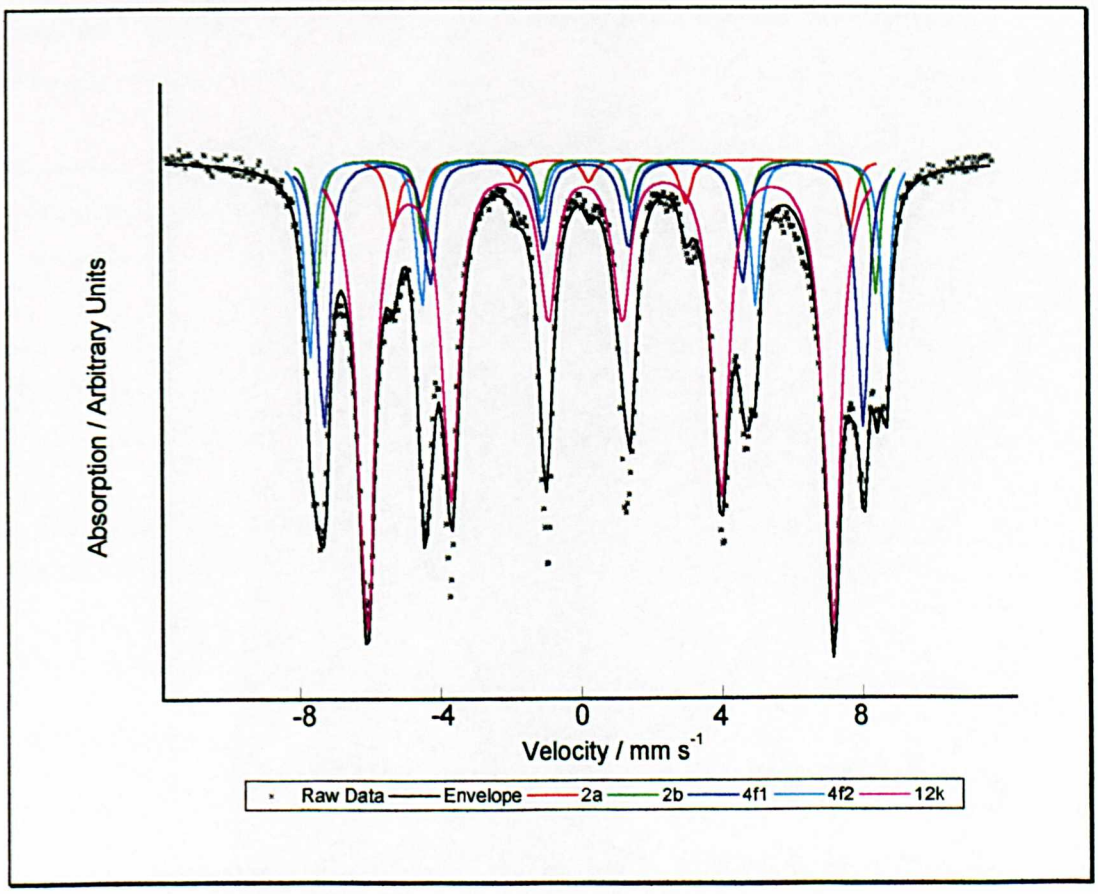

Figure 5-31 ^{57}Fe Mössbauer spectrum collected at 298K from $Sr_{0.95}La_{0.05}Fe_{12}O_{19}$ prepared by the hydrothermal processing of metal nitrates.

5.3.5.5 ^{57}Fe Mössbauer spectrum recorded from $Sr_{0.9}La_{0.10}Fe_{12}O_{19}$ at 298K

The ^{57}Fe Mössbauer parameters obtained from computer fitting of the spectrum is shown in Table 5-33. The spectrum is shown in Figure 5-32.

Site	$\delta \pm 0.03$ (mm s^{-1})	$\Delta \pm 0.05$ (mm s^{-1})	H ± 0.5 (T)
2a	0.34	0.28	49.1
2b	0.24	2.00	40.3
$4f_1$	0.30	0.20	47.2
$4f_2$	0.38	0.28	50.7
12k	0.35	0.36	40.9

Table 5 -33 ^{57}Fe Mössbauer parameters collected from $Sr_{0.90}La_{0.10}Fe_{12}O_{19}$ prepared by hydrothermal processing of metal nitrates.

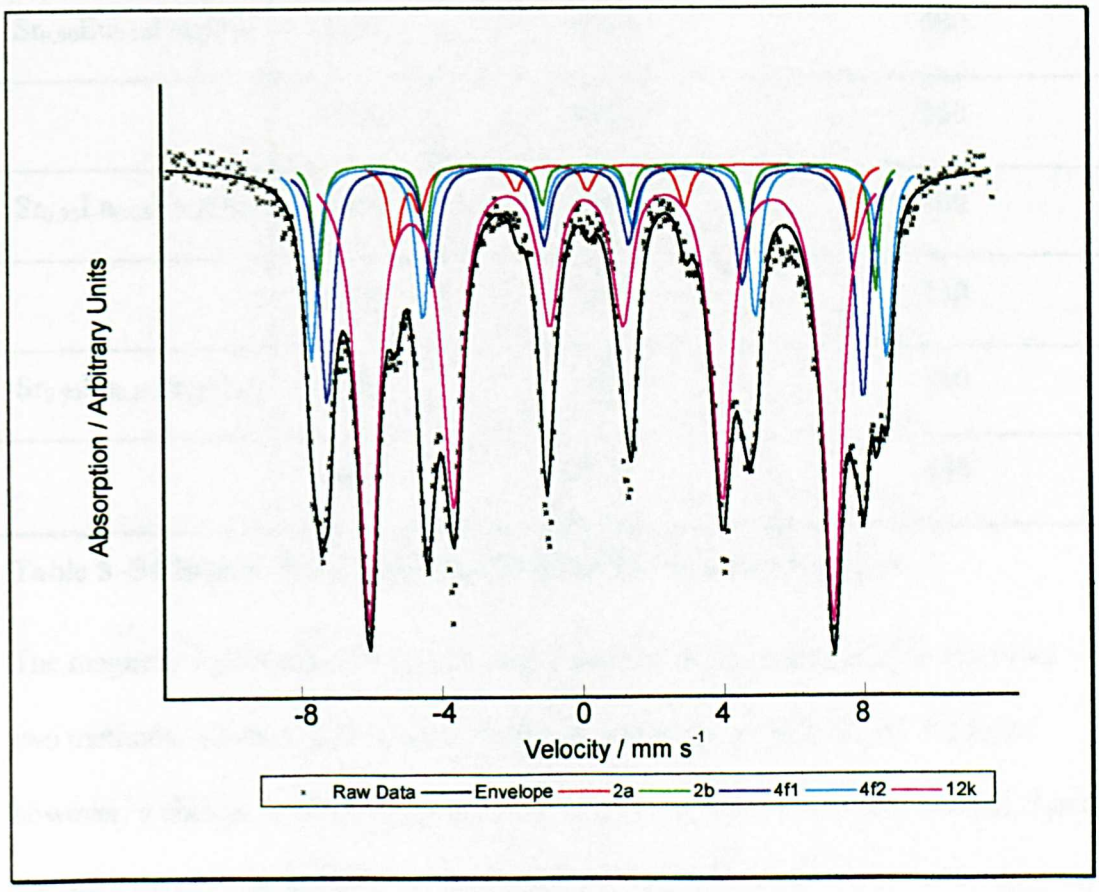

Figure 5-32 ^{57}Fe Mössbauer spectrum collected at 298K from $Sr_{0.90}La_{0.10}Fe_{12}O_{19}$ prepared by the hydrothermal processing of metal nitrates.

5.3.6 Magnetic Susceptibility Measurements.

The results obtained from analysis of the magnetic hysteresis loop measurements carried out in both the easy and hard directions are shown in Table 5-34. An example of a magnetic hysteresis loop is shown in Figure 5-33.

Sample	Direction	Coercivity ±1000 (Oe)	Remanence ± 50 (Gauss)
$SrFe_{12}O_{19}$	Easy	5000	170
	Hard	6000	410
$Sr_{0.95}Eu_{0.05}Fe_{12}O_{19}$	Easy	10000	350
	Hard	10000	300
$Sr_{0.90}Eu_{0.10}Fe_{12}O_{19}$	Easy	8300	480
	Hard	8300	250
$Sr_{0.95}La_{0.05}Fe_{12}O_{19}$	Easy	5600	460
	Hard	7500	130
$Sr_{0.90}La_{0.10}Fe_{12}O_{19}$	Easy	5500	340
	Hard	5500	140

Table 5 -34 Results from magnetic hysteresis loop measurements.

The magnetic hysteresis data are similar to that for samples prepared by the other two methods. There is little change in values across the dopant series. There is however, a change in the average values for samples prepared by this method. Since the particles of these systems are flat hexagonal plates, (Section 5.3.4 and 5.3.5), the intrinsic magnetic field of each particle is smaller for a given diameter. This reduction in volume directly lowers the magnetic field required to remove the

induced field to zero, by reducing the required field, thus lowering the magnetic coercivity, this is illustrated in Section 1.2.4.

The shape anisotropy of these particles has the effect of reducing the magnetic remanence of these systems. In some cases the remanence drops considerably.

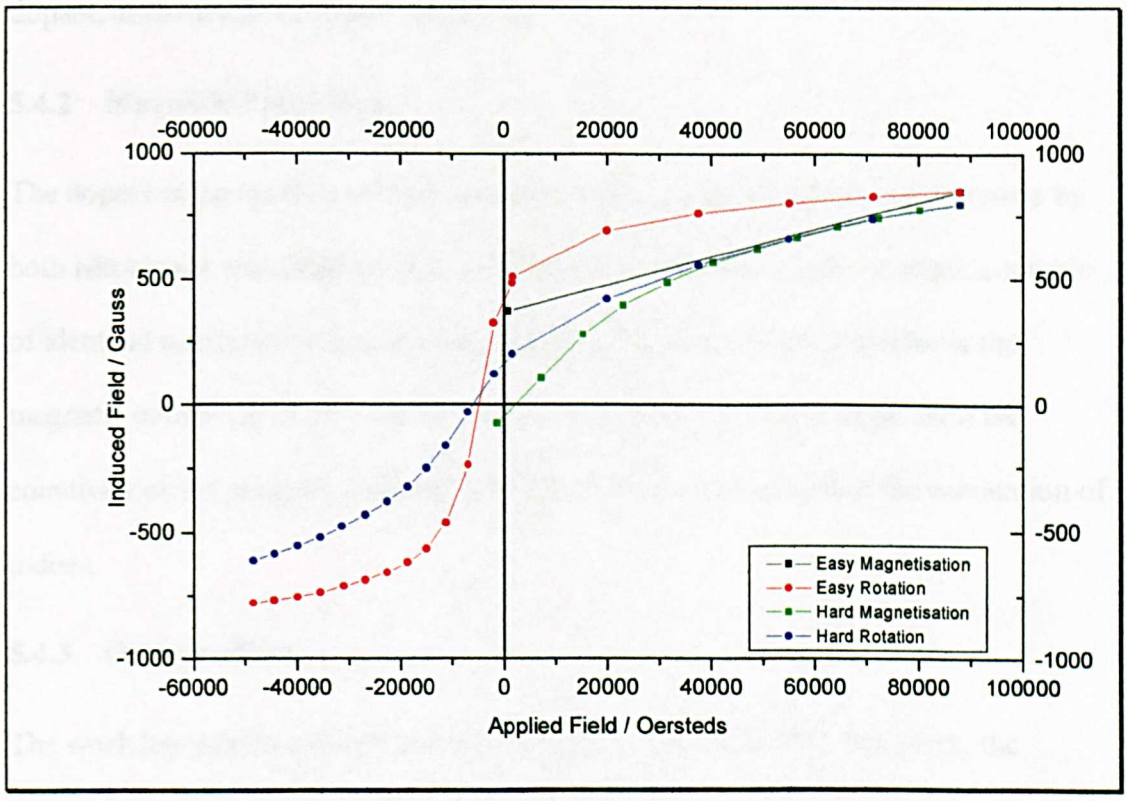

Figure 5-33 Magnetic Hysteresis loops recorded from $SrFe_{12}O_{19}$.

5.4 Conclusion.

5.4.1 Structural properties.

The results show that the addition of a dopant, at these levels, has had no measurable change on structural properties.

The method of synthesis did affect the particle size. When samples of identical composition prepared by different methods are compared, it is found that the particle size varies with the temperature of calcination. It is found that the higher the

temperature of synthesis, the larger the particle volume. The particle morphology also changes with synthetic procedure, with samples prepared by hydrothermal processing of metal nitrates being flat hexagonal plates, while those prepared by the other two methods are spherical. This effect has also been found to be independent of dopant, at the levels of dopant used here.

5.4.2 Magnetic Properties.

The dopant at the levels used had negligible effect on the properties as measured by both Mössbauer spectroscopy, and magnetic susceptibility. However when a sample of identical composition is compared across the three methods of synthesis the magnetic coercivity of the co-precipitated samples is ~six times larger than the coercivity of the samples prepared by hydrothermal processing and the calcination of oxides.

5.4.3 Overall effects.

The work reported has shown that, at the level of dopant used in this work, the method of synthesis has a larger effect on the magnetic properties than the effect of the dopant. Given that a lot of current work in the area of magnetic materials is directed into finding materials with a wide range of properties, the results suggest that the method of synthesis can have a larger effect on the magnetic properties than the dopants used.

5.5 References.

1. A Boultif and D Louer, *J. Appl. Crystallogr.*, 1991, **24**, 987.

2. R.D Shannon, *Acta Cryst*, 1976, **A32**.

3. Ch Sauer, U Kobler, W Zinn and H Stablein, *J. Phys. Chem. Solids*, 1978, **39**, 1197.

4. R.D Shannon and C.T Prewitt, *Acta Cryst*, 1969, **B25**, 925.

5. K Kimura, M Ohgaki, K Tanaka, H Morikawa and F Marumo, *J. Solid State Chem.*, 1990, **87**, 186.

6. A.M. van Diepen and F.K.Lotgering, *J. Phys. Chem. Solids*, 1974, **35**, 1641.

7. T Choudhury, S.O Saied, J.L Sullivan and A.M Abbot, *J. Phys. D: Appl. Phys.*, 1989, **22**, 1185.

8. N.S Mcintyre and D.G Zetaruk, *Anal. Chem.*, 1977, **49**, 1521.

9. A.R West, *Solid Chemistry and Its Applications*, John Wiley & Sons, Chichester, 1992.

10. B.J Evans, F Grandjean, A.P Lilot, R.H. Vogel and A.Gérard, *J. Magn. Magn. Mater.*, 1987, **67**, 123.

11. K Haneda, C Miyakawa and K Goto, *IEEE Trans. Magn.*, 1987, **MAG-23**, 3134.

12. C Kittel, *Introduction to Solid State Physics*, John Wiley & Sons, New York, 7th edn 1996.

APPENDICES.

6.1 Appendix I – Best fit parameters to Fe K-edge XAFS recorded from lanthanum doped hexaferrites prepared by the calcination of oxides.

Sample	Shell	Element	CN	R (Å)	$2\sigma^2$(Å^2)	R-value
$SrFe_{12}O_{19}$	1	O	3.9	1.93±0.1	0.023	24.3
	2	O	1.6	2.15±0.1	0.055	
	3	Fe	3.0	2.95±0.1	0.028	
	4	Sr	1.3	3.38±0.2	0.010	
	5	O	6.5	3.41±0.2	0.028	
	6	Fe	5.4	3.60±0.2	0.020	
$Sr_{0.95}La_{0.05}Fe_{12}O_{19}$	1	O	3.9	1.93±0.1	0.023	25.1
	2	O	1.6	2.26±0.1	0.040	
	3	Fe	3.0	2.97±0.1	0.031	
	4	Sr	1.3	3.37±0.2	0.011	
	5	O	6.5	3.34±0.2	0.036	
	6	Fe	5.4	3.52±0.2	0.043	
$Sr_{0.90}La_{0.10}Fe_{12}O_{19}$	1	O	3.9	1.92±0.2	0.037	25.0
	2	O	1.6	2.24±0.2	0.030	
	3	Fe	3.0	2.96±0.2	0.028	
	4	Sr	1.3	3.35±0.2	0.010	
	5	O	6.5	3.30±0.2	0.042	
	6	Fe	5.4	3.47±0.2	0.042	

6.2 Appendix II - Best fit parameters to Fe K-edge XAFS recorded from hexaferrites prepared by the co-precipitation of gels

Sample	Shell	Element	CN	R (Å)	$2\sigma^2$(Å^2)	R-value
$SrFe_{12}O_{19}$	1	O	3.9	1.91±0.1	0.014	23.7
	2	O	1.6	2.06±0.1	0.010	
	3	Fe	3.0	2.95±0.1	0.022	
	4	Sr	1.3	3.39±0.2	0.005	
	5	O	6.5	3.42±0.2	0.017	
	6	Fe	5.4	3.56±0.2	0.006	
$Sr_{0.95}La_{0.05}Fe_{12}O_{19}$	1	O	3.9	1.92±0.1	0.011	25.3
	2	O	1.6	2.07±0.1	0.010	
	3	Fe	3.0	2.95±0.1	0.022	
	4	Sr	1.3	3.41±0.2	0.007	
	5	O	6.5	3.43±0.2	0.017	
	6	Fe	5.4	3.57±0.2	0.012	
$Sr_{0.90}La_{0.10}Fe_{12}O_{19}$	1	O	3.9	1.92±0.1	0.012	24.0
	2	O	1.6	2.08±0.1	0.010	
	3	Fe	3.0	2.95±0.1	0.022	
	4	Sr	1.3	3.40±0.2	0.006	
	5	O	6.5	3.43±0.2	0.017	
	6	Fe	5.4	3.58±0.2	0.008	

6.3 Appendix III - Best fit parameters to Fe K-edge XAFS recorded from hexaferrites prepared by the hydrothermal processing of metal nitrates.

Sample	Shell	Element	CN	R (Å)	$2\sigma^2$ (Å^2)	R-value
$SrFe_{12}O_{19}$	1	O	3.9	1.92±0.1	0.011	27.5
	2	O	1.6	2.06±0.1	0.008	
	3	Fe	3.0	2.93±0.1	0.017	
	4	Sr	1.3	3.45±0.2	0.018	
	5	O	6.5	3.45±0.2	0.016	
	6	Fe	5.4	3.59±0.2	0.016	
$Sr_{0.95}La_{0.05}Fe_{12}O_{19}$	1	O	3.9	1.91±0.1	0.010	24.8
	2	O	1.6	2.06±0.1	0.004	
	3	Fe	3.0	2.93±0.1	0.018	
	4	Sr	1.3	3.44±0.2	0.003	
	5	O	6.5	3.43±0.2	0.011	
	6	Fe	5.4	3.59±0.2	0.005	
$Sr_{0.90}La_{0.10}Fe_{12}O_{19}$	1	O	3.9	1.90±0.1	0.008	24.2
	2	O	1.6	2.06±0.1	0.001	
	3	Fe	3.0	2.92±0.1	0.016	
	4	Sr	1.3	3.44±0.2	0.004	
	5	O	6.5	3.43±0.2	0.011	
	6	Fe	5.4	3.57±0.2	0.005	